International Journal of Aerospace Engineering

Optimal Control Techniques in Aircraft Guidance and Control

Lead Guest Editor: Ernesto Staffetti
Guest Editors: Alessandro Gardi, Xiang Li, Yoshinori Matsuno, and Manuel Soler

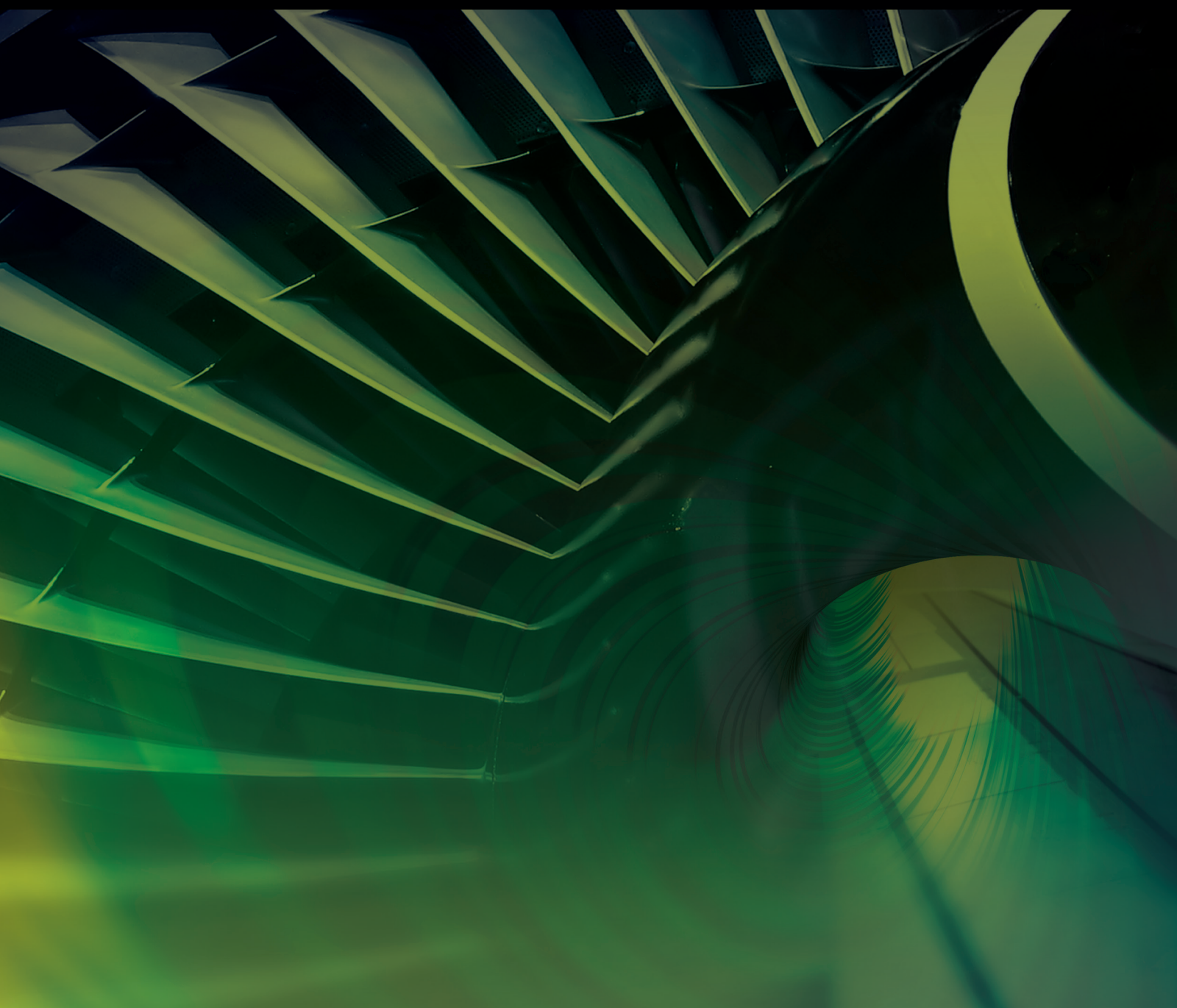

Optimal Control Techniques in Aircraft Guidance and Control

International Journal of Aerospace Engineering

Optimal Control Techniques in Aircraft Guidance and Control

Lead Guest Editor: Ernesto Staffetti
Guest Editors: Xiang Li, Yoshinori Matsuno, and Manuel Soler

Editorial Board

Contents

Hindawi
International Journal of Aerospace Engineering
Volume 2019, Article ID 3026083, 2 pages
https://doi.org/10.1155/2019/3026083

Editorial

Optimal Control Techniques in Aircraft Guidance and Control

Ernesto Staffetti,[1] **Xiang Li**,[2] **Yoshinori Matsuno**,[3] **and Manuel Soler**[4]

[1]*University Rey Juan Carlos, Madrid, Spain*
[2]*Beijing Institute of Technology, Beijing, China*
[3]*Japan Aerospace Exploration Agency, Tokyo, Japan*
[4]*University Carlos III of Madrid, Madrid, Spain*

Correspondence should be addressed to Ernesto Staffetti; ernesto.staffetti@urjc.es

Received 23 May 2019; Accepted 27 June 2019; Published 5 August 2019

Optimal control is a branch of mathematics that deals with analytical and numerical methods to design control strategies for dynamical systems in which some measures of performance are optimised.

Applications of optimal control in aeronautical engineering include aircraft guidance and control. Aircraft guidance refers to the determination of the trajectory to steer the aircraft between two different states. Techniques for aircraft guidance are in general open loop. Aircraft control refers to the determination of the control inputs to follow the planned trajectories while maintaining aircraft stability and smooth manoeuvring. In this case, closed-loop control techniques must be employed.

Although optimal control has been applied in aeronautical engineering for several decades, the continuous technological development in this field is resulting in leading to optimal control models of increasing size and complexity. As a consequence, and despite the progress in the development of numerical solution methods, the increasing size and complexity of the problems generates a constant demand for faster and more efficient methods to solve optimal control problem.

Among the most demanding problems from the computational point of view are the stochastic optimal control problems, in which uncertainties are taken into account and the obtained solution must fulfil probabilistic constraints.

The purpose of this special issue is to bring recognition to the contribution of optimal control techniques to aircraft guidance and control and to provide a forum to disseminate the latest research work with the aim of further stimulating interest in this area of great potential.

The special issue includes several high-quality papers written by leading and emerging specialists in the field.

14 submissions have been received. After a rigorous refereeing process, 5 papers have been accepted for publication in this special issue.

A short description of the addressed topics is presented.

In "Efficient Convex Optimization of Reentry Trajectory via the Chebyshev Pseudospectral Method" by C.-M. Yu et al., optimal control techniques based on the Chebyshev pseudospectral method and on a novel sequential convex optimisation scheme have been applied to solve the hypersonic reentry trajectory optimisation problem.

In "Analyzing the Departure Runway Capacity Effects of Integrating Optimized Continuous Climb Operations" by M. V. Díaz et al., optimal control techniques based on the Chebyshev pseudospectral method have been applied to study the effects of the introduction of continuous climb operations on runway capacity.

In "Characterization and Enhancement of Flight Planning Predictability under Wind Uncertainty" by J. García-Heras et al., potential enhancements in flight planning predictability due to the effects of wind uncertainty are analyzed using a robust optimal control methodology. In this work, wind uncertainty is retrieved out of ensemble probabilistic forecasts.

In "Evasion-Pursuit Strategy against Defended Aircraft Based on Differential Game Theory" by Q. Sun et al., an

optimal guidance law based on differential game theory is derived for the attacker in an active defence scenario, in which the attacker evades from the defender and pursues the target.

In "Cooperative Guidance of Seeker-Less Missiles for Precise Hit" by J. Zhao and F. Xiong, linear-quadratic optimal control and biased proportional navigation guidance are employed to develop a two-stage cooperative guidance law for fire-and-forget attacks for seeker-less missiles.

Conflicts of Interest

We declare that none of the authors of the editorial have a conflict of interest.

Ernesto Staffetti
Xiang Li
Yoshinori Matsuno
Manuel Soler

Hindawi
International Journal of Aerospace Engineering
Volume 2019, Article ID 6141452, 29 pages
https://doi.org/10.1155/2019/6141452

Research Article

Characterization and Enhancement of Flight Planning Predictability under Wind Uncertainty

Javier García-Heras, Manuel Soler, and Daniel González-Arribas

Bioengineering and Aerospace Engineering, Universidad Carlos III, Leganés, Madrid, Spain

Correspondence should be addressed to Javier García-Heras; javier.garcia-heras@uc3m.es

Received 16 November 2018; Revised 22 March 2019; Accepted 11 April 2019; Published 17 June 2019

Academic Editor: Kenneth M. Sobel

A novel study is presented aiming at characterizing and illustrating potential enhancements in flight planning predictability due to the effects of wind uncertainty. A robust optimal control methodology is employed to calculate robust flight plans. Wind uncertainty is retrieved out of Ensemble Probabilistic Forecasts. Different wind approximation functions are compared, typifying errors, and illustrating its importance for accurate solving of the robust optimal control problem. A set of key performance indicators is defined for the quantification of uncertainty in terms of flight time and fuel consumption. Two different case studies are presented and discussed. The first one is based on a representative sample of the whole 2016 year for a single origin-destination and a forecast time step of 6 hours. As for the second, we select the most uncertain day together with a multiorigin-destination set of flights with forecast time steps up to 2 days.

1. Introduction

The Air Traffic Management (ATM) System is undergoing a paradigm shift aiming at enhancing its environmental impact, capacity, safety, and efficiency. Different worldwide programmes are fostering this transformation, mainly the Single Sky ATM Research (SESAR) in Europe and Next Generation Air Transportation System (NextGen) in USA, yet also in the Asia/Pacific region, the Collaborative Actions for Renovation of Air Traffic Systems (CARATS) in Japan and the New Generation ATM System (CNAS) in China. Improvement in the ATM system predictability has been identified as paramount to achieve the above-mentioned high-level goals (see, e.g., SESAR-JU. European ATM Master Plan Edition 2015). All ATM system actors, including pilots, air traffic controllers, airlines, dispatchers, air navigation service providers, meteorological offices, and the network manager, are daily facing the effects of uncertainty. Should the capacity of the system be increased while maintaining high safety standards and improving the overall performance, uncertainty levels in ATM must be reduced and, when possible, find new strategies to deal with and eventually reduce it. For instance, it is well-known that the sector's capacity is under-declared due to uncertain entry/occupancy counts, thus limiting the capacity of the system. Also, adding unnecessary fuel leads to a nonneglectable loss of efficiency, e.g., Hao et al. in [1] conclude that 1 min in reducing flight time dispersion could save between $120 and $452 million per year only considering US domestic airlines.

Uncertainty in ATM is nevertheless a heavily involved, multilayered, and interrelated phenomena. The analysis of uncertainty in ATM should take into the different scales, yet also the different sources that introduce uncertainty into the system. For deeper insight on this taxonomy, refer to [2] (Chapter 4). From a scale perspective, ATM uncertainty can be grouped into macroscale (the air transport network), mesoscale (traffic scale), and microscale (single flight). Previous work analyzing uncertainty effects at both macro- and mesoscales include, e.g., Goyens et al. [3], who studied delay propagation across the European network; Valenzuela et al.

in [4], who studied probabilistic sector loading considering wind uncertainties; and Cook et al. [5], who applied complex network theory to the ATM system. Needless to say, the focus of the present paper is on flight uncertainty (microlevel).

Regarding flight uncertainty, [2] (Chapter 4) distinguishes four time frames, namely, strategic (flow management planning level, from months up to two/three hours before the off-block time), predeparture (flight dispatching planning level, from two/three hours up to off-block time), gate-to-gate (execution both airborne and taxi times), and postarrival (from on-block time). Source-wise, ATM uncertainty falls into the following five categories: data uncertainty, operational uncertainty, equipment uncertainty, and meteorological uncertainty. Indeed, meteorological uncertainty has been recognized as one of the most (if not the most) important sources introducing uncertainty into the ATM system (see also [2]). All five uncertainty sources obviously affect flight predictability at its different time frames, which is mainly due to [6] not perfect knowledge of the initial conditions (e.g., off-block time, departure time, and initial mass), inaccurate aircraft performance model (e.g., weight, aerodynamics, Earth models, and atmospheric variables), uncertain meteorological conditions (e.g., convection and wind), navigation and equipment errors (e.g., flight management system, avionics, and flight technical errors), and ATM-related operational uncertainty (regulations, ATC advisories). Some previous work on initial condition error estimation include, e.g., Sun et al. [7], who estimate aircraft initial mass using ADS-B data. Also, Vazquez and Rivas [8] studied the propagation of initial mass uncertainty. In [6], the authors use Polynomial Chaos Expansion (PCE) to propagate uncertainties along a given flight intent considering disturbances due to initial conditions, the aircraft performance model, the Earth and atmospheric model, the aircraft intent, and wind.

We are herein interested in both the strategic and predeparture time frames, the ones compatible with flight planning. Yet, analyzing meteorological uncertainty and its effects on flight planning, to the best of the authors' knowledge, has received not enough attention so far. Indeed, wind uncertainty modelling in [6] considers uniform wind field distributions based on a deterministic forecast. More advanced features are demanded, such as the use of Ensemble Prediction System (EPS) forecasts, which provide probabilistic forecasts.

One of the first (if not the first) works on EPS-based wind uncertainty modelling and flight trajectories is due to Cheung et al. [9]. They used EPS information to study the impact of wind uncertainty in flight duration on a given, fixed route over the North Atlantic. A great impact in flight duration was observed, with no seasonal variation, and an important decrease when the time frame gets closer to the used forecast. Moreover, Vazquez et al. [10] analyzed the influence of along-track wind uncertainty (also based on EPS) in fuel mass distribution based on a probabilistic transformation method. Both studies can be casted as trajectory prediction problems since the flight path is known a priori, and thus, they are only capable of characterizing uncertainty. The ambition in this paper is not only to characterize but also to reduce uncertainty. For that purpose, flight planning algorithms that take into consideration predictability should be derived. Research to this end is rather recent and still needs more insight.

For flight planning purposes, a rather straightforward approach is to extend some of the probabilistic trajectory prediction approaches (e.g., [9, 10]) to consider a higher algorithmic level in which the flight path is found using the discrete optimization method. This was followed by Cheung et al. in [11], where they used a Dijkstra-based trajectory predictor and also evaluated the quality of different EPSs, and by Franco et al. [12], who addressed the optimization of a North Atlantic crossing also using a Dijkstra algorithm together with their probabilistic trajectory predictor based on the probabilistic transformation method. A different approach is due to Legrand et al. [13], who presented a robust wind (obtained from EPS) optimal trajectory design algorithm based on dynamic programming and minimum-energy trajectory clustering. It should be noted that all these three approaches for flight planning under wind uncertainty are somehow based on discrete optimization. In [14], Gonzalez-Arribas et al. presented a robust optimal control approach to flight planning under wind uncertainty (obtained from EPS) in which the flight plan can be optimized considering efficiency and predictability. The present paper is based on the latter methodology, with the aim at generalizing it to different scenarios and modelling features, and thus advance in the understanding of the effects of meteorological uncertainty.

All in all, the contribution of this paper is threefold. First, we extend the methodology in [14] to consider spline wind approximations. It is shown that the errors committed in wind approximation (using, e.g., polynomial approximation such in [14]) have a tremendous impact, leading to ill-conditioned solutions. Second, instead on analyzing a single flight (as in previous work), we generalize for different days (and thus meteorological conditions) and for different origin-destinations. We also analyze the effects of wind uncertainty at different flight planning horizons, i.e., predeparture (3 hours before departure), which could be useful for flight dispatchers, and strategic (1 day before departure), which could be useful for the network manager for probabilistic capacity-demand balancing. Third, we characterize the quality of the flight plan prediction (and its uncertainty) against a hypothetical realization of winds based on reanalysis information. We note (as will be exposed) that further insights in the latter are demanded in future research and this third contribution remains as a preliminary step.

The methodology has been sketched in Figure 1. Firstly, wind data is collected from the EPS forecast. Secondly, wind forecasts are approximated by Lipschitz-continuous functions in order to model wind is a form compatible with the robust optimal planning methodology in [14]. Thirdly, the so-termed Robust Optimal Control Problem (ROCP) is solved, obtaining a Pareto frontier with different trade-offs between fuel consumption and predictability. Then, the flight path (obtained as a solution to the ROCP and defined by a sequence of waypoints) is introduced into a standard trajectory predictor (TP) ([15], Chapter 3), which *flies* the precalculated route using wind information retrieved from the original source (raw, tabular), either EPS or reanalysis. Finally, flight times, fuel burns, and its associated dispersions

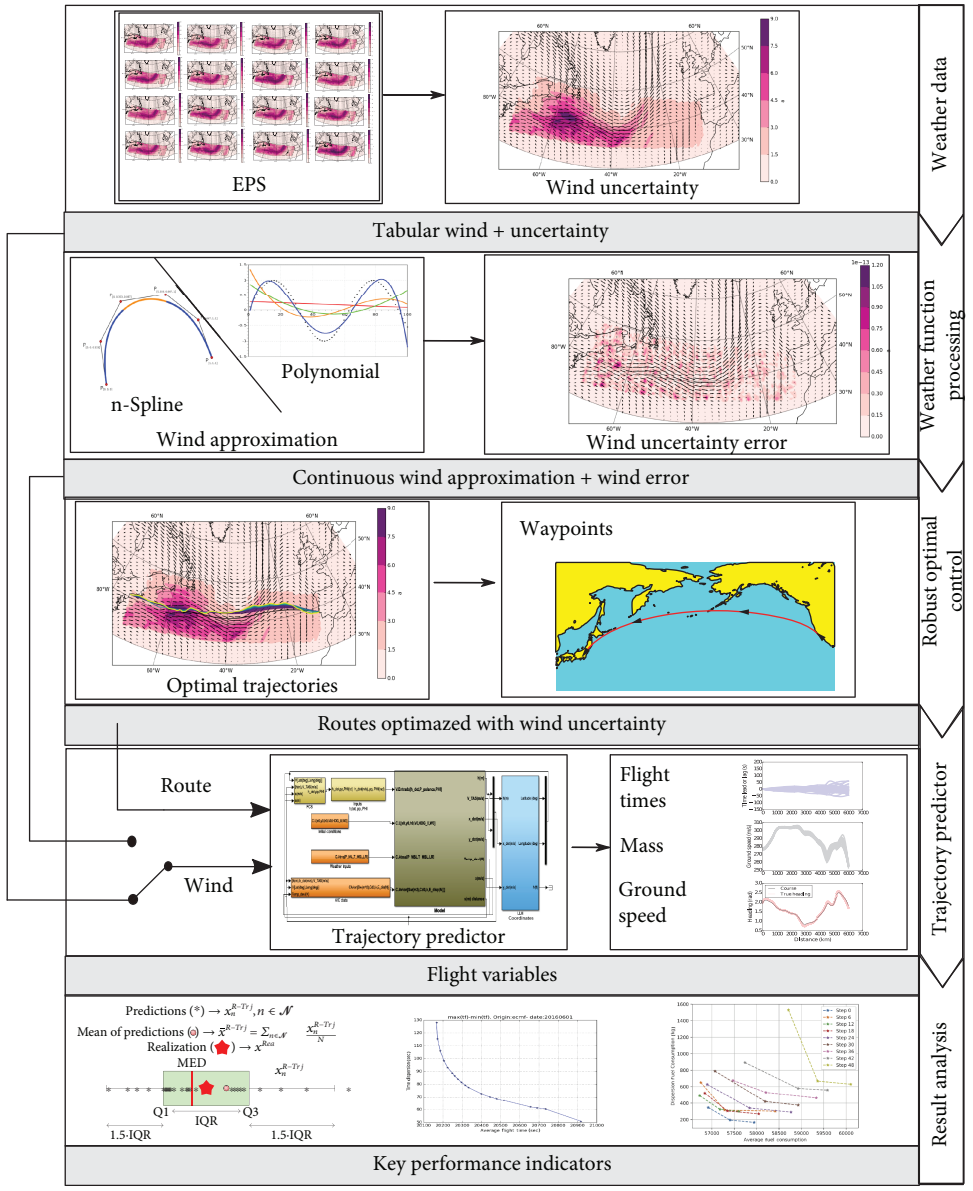

Figure 1: Methodological diagram.

are analyzed. Different Key Performance Indicators (KPIs) are defined to that end.

Two different case studies are presented. The first focuses on a single prediction horizon (referred to as step), choosing a single origin-destination flight (over the North Atlantic), and a systematic date analysis along year 2016 (choosing the 1st, 5th, 10th, 15th, 20th, and 25th of each month as representative days). The second focuses on a single day (5th October 2016, the one that resulted to be the most unpredictable one in the former analysis), multiple origin-destination flights (based on the schedule of an important airline), and with forecasting steps ranging from 0 to 48 hours (by 6 hours). The first study aims at characterizing the seasonal influence at the predeparture time horizon, i.e., compatible with flight dispatching time frames; the second aims at the geographical influence, yet on a more strategic vision, i.e., compatible with the network manager's time frames.

2. Robust Flight Planning

2.1. Robust Optimal Control Methodology. Our approach is based on the robust optimal control methodology for aircraft trajectory optimization problems presented in [14]. We will here summarize the method for the sake of completeness.

2.1.1. Robust Optimal Control. Let us consider a dynamical system with a randomly parametrized differential-algebraic equation and constraints. Uncertainty is described using a standard Kolmogorov probability space $(\Omega, \mathcal{F}, P)$, composed of a sample space of possible outcomes Ω, a σ-algebra of events $\mathcal{F}$ containing sets of outcomes, and the probability

function P assigning probabilities to each of these events. The uncertain parameters of the system will be modelled as a no time-dependent random variable $\xi : \Omega \to \mathbb{R}^{n_\xi}$. For each possible outcome $\omega \in \Omega$, the random variables take a different value $\xi(\omega)$.

Let us denote the state vector $\mathbf{x} \in \mathbb{R}^{n_x}$, the control vector $\mathbf{u} \in \mathbb{R}^{n_u}$, the algebraic variables $\mathbf{z} \in \mathbb{R}^{n_z}$, and $t \in \mathbb{R}$ as the independent variable (typically time). For each outcome $\omega_0 \in \Omega$, there exist a unique trajectory path $t \to (\mathbf{x}(\omega_0, t), \mathbf{z}(\omega_0, t), \mathbf{u}(\omega_0, t))$ that corresponds to the realization of the random variables $\xi(\omega_0)$. The dynamics of the system are given by the functions $f : \mathbb{R}^{n_x} \times \mathbb{R}^{n_z} \times \mathbb{R}^{n_u} \times \mathbb{R}^{n_\xi} \times \mathbb{R} \to \mathbb{R}^{n_x}$, $h : \mathbb{R}^{n_x} \times \mathbb{R}^{n_z} \times \mathbb{R}^{n_u} \times \mathbb{R}^{n_\xi} \times \mathbb{R} \to \mathbb{R}^{n_h}$, and $g : \mathbb{R}^{n_x} \times \mathbb{R}^{n_z} \times \mathbb{R}^{n_u} \times \mathbb{R}^{n_\xi} \times \mathbb{R} \to \mathbb{R}^{n_g}$, such that valid trajectories fulfill the conditions almost surely (i.e., with probability 1) (the $\leq$ sign applies in an element-wise fashion in equation (3) and analogous equations.):

$$\frac{d}{dt}\mathbf{x}(\omega, t) = f(\mathbf{x}(\omega, t), \mathbf{z}(\omega, t), \mathbf{u}(\omega, t), \xi(\omega), t), \tag{1}$$

$$h(\mathbf{x}(\omega, t), \mathbf{z}(\omega, t), \mathbf{u}(\omega, t), \xi(\omega), t) = 0, \tag{2}$$

$$g_L \leq g(\mathbf{x}(\omega, t), \mathbf{z}(\omega, t), \mathbf{u}(\omega, t), \xi(\omega), t) \leq g_U, \tag{3}$$

where $\omega \in \Omega$ is the sample point on the underlying abstract probability space. Therefore, for each possible scenario or realization of the random parameters $\xi(\omega)$, the trajectory will follow the deterministic differential equation (1) for the corresponding fixed value of ξ. We employ the notation $\mathbf{x}(\omega, t)$ and $\mathbf{u}(\omega, t)$ in order to emphasize the fact that the trajectory depends on the realization of the random parameters. Note that, because the random parameters are constant in time and thus the system is not described by a full stochastic differential equation (as in, for example, [16]), there is no need to consider filtered σ-algebras to deal with potential measurability issues.

We follow the optimal *guidance* scheme of [14] that relies on the notion of *tracked* states.

Definition 1. A state is said to be *tracked* if its trajectory is assumed to be independent of the realization of the random variables almost surely, i.e., with probability one.

In this concept, the controls are specific to each scenario in order to guarantee that the tracked states follow the unique computed trajectory of those states that are tracked. Naturally, the practical consideration of this framework requires a dynamical system where the controls can be computed online to ensure that the realization of the trajectory of the tracked states stays close to its precomputed value. This is the case of the aircraft, since the flight control systems of an aircraft can follow a given route and vertical profile. For an in-depth explanation of this concept and why it is adequate for a flight planning problem, we refer the reader to [14]. We now proceed to illustrate the main concepts.

Definition 2. The amount *control degrees of freedomd* of the dynamical system is defined, in this work, as the number of controls and free algebraic variables minus the number of algebraic restrictions: $d = n_z + n_u - n_h$.

Let $q_x \leq \min\{n_x, d\}$ be the number of tracked states; without loss of generality, we can assume that the tracked states are the first q_x states (rearrange the state vector otherwise), i.e.,

$$\mathbf{x} = \begin{bmatrix} x_1 \cdots x_{q_x} x_{q_x+1} \cdots x_{n_x} \end{bmatrix}^T = \begin{bmatrix} \mathbf{x}_q \\ \mathbf{x}_r \end{bmatrix}, \tag{4}$$

where $\mathbf{x}_q$ is the tracked part of the state vector and $\mathbf{x}_r$ is the untracked part. Let $\mathbb{I}_n$ be the identity matrix of shape $n \times n$ and $0_{n_1,n_2}$ be the zero matrix (i.e., a matrix with zeroes in all its entries) of shape $n_1 \times n_2$. We define the matrix $E_x \in \mathbb{R}^{q_x \times n_x}$ as

$$E_x = \begin{bmatrix} \mathbb{I}_{q_x} & 0_{q_x, n_x - q_x} \end{bmatrix}. \tag{5}$$

This matrix transforms the state vector into the tracked states vector $\mathbf{x}_q = E_x\mathbf{x}$ that contains only the states whose evolution is equal in all scenarios. In this work, $q_x = d$ will hold so that there are enough tracked states to consume all available control degrees of freedom. This is not necessary in general. With the aid of the tracking matrices, we can now define the tracking conditions (which, again, apply almost surely):

$$\begin{aligned} E_x(\mathbf{x}(\omega_1, t) - \mathbf{x}(\omega_2, t)) &= 0, \forall t, \forall \omega_1, \omega_2 \in \Omega, \\ E_z(\mathbf{z}(\omega_1, t) - \mathbf{z}(\omega_2, t)) &= 0, \forall t, \forall \omega_1, \omega_2 \in \Omega, \\ E_u(\mathbf{u}(\omega_1, t) - \mathbf{u}(\omega_2, t)) &= 0, \forall t, \forall \omega_1, \omega_2 \in \Omega. \end{aligned} \tag{6}$$

The tracking conditions enforce equality in the tracked variables between realizations: note that, $E_x(\mathbf{x}(\omega_1, t) - \mathbf{x}(\omega_2, t))$ is the vector of differences between the tracked states in outcome ω_1 and the tracked states in outcome ω_2. The other two conditions are analogous tracking conditions for the dependent variables and the controls.

Let us define a Bolza-type functional in optimal control problems:

$$\widehat{J} = \Phi\left(t_0, t_f, \mathbf{x}(t_0), \mathbf{x}\left(t_f\right)\right) + \int_{t_0}^{t_f} \mathscr{L}(\mathbf{x}, \mathbf{z}, \mathbf{u}, \xi, t)dt. \tag{7}$$

For each possible scenario or realization of the random parameters $\xi(\omega)$, we have an objective value of $\widehat{J}$. In order to build a scalar objective function, we rely on both expectations and dispersions. Without generality, the latter can be characterized using the central moments, the range, or the interquartile range (IQR), just to mention a few. In our case, and in order to account for worst-case scenarios, we choose the range.

Let us then define the range R of $\widehat{J}$ as

$$R\left(\widehat{J}\right) = \left(\max_{\omega \in \Omega} \widehat{J} - \min_{\omega \in \Omega} \widehat{J}.\right) \tag{8}$$

The robust optimal control problem with tracking is now formulated as follows (an alternative formulation could, for instance, rely on the n^{th} central moment of a random variable $\widehat{J}$ as $\mu_n = \mathbb{E}[(J\wedge - \mathbb{E}[J\wedge])^n]$ and then substituting the range in $R(\widehat{J})$ by μ_n.) [14]:

$$\min J = \mathbb{E}\left[\widehat{J}\right] + \mathrm{dp} \cdot \left(\max_{\omega\in\Omega}\widehat{J} - \min_{\omega\in\Omega}\widehat{J}\right) \tag{9}$$

subject to: initial conditions

$$\mathbf{x}(t_0) = \mathbf{x}_0\,; \tag{10}$$

final conditions

$$\mathbb{E}\left[\Psi\left(t_f, \mathbf{x}\left(t_f\right)\right)\right] = 0\,; \tag{11}$$

differential-algebraic equations and constraints (1)–(3) grouped as

$$\begin{aligned} \frac{d}{dt}\mathbf{x} &= f(\mathbf{x}, \mathbf{z}, \mathbf{u}, \xi, t),\\ h(\mathbf{x}, \mathbf{z}, \mathbf{u}, \xi, t) &= 0,\\ g_L \le g(\mathbf{x}, \mathbf{z}, \mathbf{u}, \xi, t) &\le g_U, \end{aligned} \tag{12}$$

and the tracking conditions (6).

Where in the above, $\mathbb{E}[\cdot]$ is the expectation operator associated with the probability space $(\Omega, \mathcal{F}, P)$; the terminal cost or the Mayer term is $\Phi : \mathbb{R}\times\mathbb{R}\times\mathbb{R}^{n_x}\times\mathbb{R}^{n_x}\to\mathbb{R}$; the running cost or the Lagrange term is $\mathscr{L} : \mathbb{R}^{n_x}\times\mathbb{R}^{n_z}\times\mathbb{R}^{n_u}\times\mathbb{R}^{n_\xi}\times\mathbb{R}\to\mathbb{R}$; dp is a weighting parameter (dispersion penalty); and function $\Psi : \mathbb{R}\times\mathbb{R}\times\mathbb{R}^{n_x}\times\mathbb{R}^{n_x}\to\mathbb{R}$ denotes the final conditions.

2.1.2. Probabilistic Discretization. In order to deal with potentially continuous random variables, we make use of discretization techniques. These methods will be referred to as stochastic quadrature rules (SQRs).

Definition 3. Given a random variable with probability measure P, a *stochastic quadrature rule (SQR)* is defined as a function or algorithm that produces a finite set of quadrature points $\{\xi_k\}$, $k\in\{1,\cdots,N\}$ and weights $\{w_k\}$, $k\in\{1,\cdots,N\}$ that approximates the integral $I = \mathbb{E}[G(\xi)] = \int G(\xi)dP$ with the sum:

$$QG = \sum_{k=1}^{N} w_k G(\xi_k), \tag{13}$$

with the approximation converging to the true value as $N\to\infty$.

In the present work, we employ a trivial quadrature rule (each ensemble member is a scenario with $w_k = 1/N$), as uncertainty is already characterized by discrete scenarios from EPS forecasts. However, the integration of additional sources of uncertainty in the future may require the usage of a nontrivial SQR.

Let $\mathbf{x}_q(t)$: $\mathbb{R}\to\mathbb{R}^{q_x}$ define a trajectory for the tracked states and $\mathbf{z}_q(t)$ and $\mathbf{u}_q(t)$ analogously. Suppose a SQR has been chosen, with a number of points N (in our case, corresponding to the N possible scenarios). For each one of these points ξ_k, the tracking trajectory $(\mathbf{x}_q, \mathbf{z}_q, \mathbf{u}_q)(t)$ defines a unique trajectory given a full set of initial conditions; we will now collect each one of these N trajectories in a *trajectory ensemble*. We define the trajectory ensemble associated with a tracking trajectory $(\mathbf{x}_q, \mathbf{z}_q, \mathbf{u}_q)(t)$ as the set of trajectories $\{(\mathbf{x}_k, \mathbf{z}_k, \mathbf{u}_k)(t)\}$ with $k\in\{1,\cdots,N\}$ such that the trajectory k is generated by the initial conditions $\mathbf{x}_k(t_0) = \mathbf{x}_0$ and the tracking trajectory with $\xi = \xi_k$, i.e.,

$$\begin{aligned} \frac{d}{dt}\mathbf{x}_k &= f(\mathbf{x}_k, \mathbf{z}_k, \mathbf{u}_k, \xi_k, t),\\ h(\mathbf{x}_k, \mathbf{z}_k, \mathbf{u}_k, \xi_k, t) &= 0,\\ g_L \le g(\mathbf{x}_k, \mathbf{z}_k, \mathbf{u}_k, \xi_k, t) &\le g_U,\\ E_x\mathbf{x}_k(t) &= \mathbf{x}_q(t),\\ E_z\mathbf{z}_k(t) &= \mathbf{z}_q(t),\\ E_u\mathbf{u}_k(t) &= \mathbf{u}_q(t). \end{aligned} \tag{14}$$

We will now build a virtual dynamical system where the state vectors of all the trajectories in the trajectory ensemble are merged into a single large state vector, which represents the collective trajectory. Its state vector $\mathbf{x}_E\in\mathbb{R}^{n_x N}$ contains the state vector of all the trajectories in the ensemble (the control $\mathbf{u}_E\in\mathbb{R}^{n_u N}$ and algebraic $\mathbf{z}_E\in\mathbb{R}^{n_z N}$ vectors are analogous), and each individual trajectory follows the dynamics associated with each scenario (with $\xi = \xi_k$).

$$\begin{aligned} \mathbf{x}_E &= \begin{bmatrix} \mathbf{x}_1 \\ \vdots \\ \mathbf{x}_N \end{bmatrix};\\ \mathbf{z}_E &= \begin{bmatrix} \mathbf{z}_1 \\ \vdots \\ \mathbf{z}_N \end{bmatrix};\\ \mathbf{u}_E &= \begin{bmatrix} \mathbf{u}_1 \\ \vdots \\ \mathbf{u}_N \end{bmatrix}. \end{aligned} \tag{15}$$

We define the differential equation, algebraic equations, and inequality constraints of this augmented dynamical system as

$$f_E(\mathbf{x}_E, \mathbf{z}_E, \mathbf{u}_E, t) = \begin{bmatrix} f(\mathbf{x}_1, \mathbf{z}_1, \mathbf{u}_1, \xi_1, t) \\ \vdots \\ f(\mathbf{x}_N, \mathbf{z}_N, \mathbf{u}_N, \xi_N, t) \end{bmatrix}, \quad (16)$$

$$h_E(\mathbf{x}_E, \mathbf{z}_E, \mathbf{u}_E, t) = \begin{bmatrix} h(\mathbf{x}_1, \mathbf{z}_1, \mathbf{u}_1, \xi_1, t) \\ \vdots \\ h(\mathbf{x}_N, \mathbf{z}_N, \mathbf{u}_N, \xi_N, t) \end{bmatrix}, \quad (17)$$

$$g_E(\mathbf{x}_E, \mathbf{z}_E, \mathbf{u}_E, t) = \begin{bmatrix} g(\mathbf{x}_1, \mathbf{z}_1, \mathbf{u}_1, \xi_1, t) \\ \vdots \\ g(\mathbf{x}_N, \mathbf{z}_N, \mathbf{u}_N, \xi_N, t) \end{bmatrix}. \quad (18)$$

Let us define the approximate cost functional, divided into Mayer and Lagrange terms, using the trajectory ensemble:

$$\widehat{J}_E = \Phi_E\left(\mathbf{x}_E(t_0), \mathbf{x}_E\left(t_f\right)\right) + \int_{t_0}^{t_f} \mathscr{L}_E(\mathbf{x}_E, \mathbf{z}_E, \mathbf{u}_E, t)dt, \quad (19)$$

$$\Phi_E\left(\mathbf{x}_E(t_0), \mathbf{x}_E\left(t_f\right)\right) = \sum_{k=1}^{N} w_k \phi\left(\mathbf{x}_k(t_0), \mathbf{x}_k\left(t_f\right)\right), \quad (20)$$

$$\mathscr{L}_E(\mathbf{x}_E, \mathbf{z}_E, \mathbf{u}_E, t) = \sum_{k=1}^{N} w_k \mathscr{L}(\mathbf{x}_k, \mathbf{z}_k, \mathbf{u}_k, t), \quad (21)$$

and discretize the boundary conditions as

$$\Psi_E\left(t_f, \mathbf{x}_E\left(\omega, t_f\right)\right) = \sum_{k=1}^{N} w_k \Psi\left(t_f, \mathbf{x}_k\left(t_f\right)\right). \quad (22)$$

For concise writing of the discretization of the tracking conditions (6), we will define the matrix $E_x^N \in \mathbb{R}^{q_x(N-1)\times n_x N}$ as

$$E_x^N = \begin{bmatrix} E_x & & \\ & \ddots & \\ & & E_x \end{bmatrix} \begin{bmatrix} \mathbb{I}_{n_x} & -\mathbb{I}_{n_x} & & & \\ & \mathbb{I}_{n_x} & -\mathbb{I}_{n_x} & & \\ & & \ddots & \ddots & \\ & & & \mathbb{I}_{n_x} & -\mathbb{I}_{n_x} \end{bmatrix}. \quad (23)$$

$E_z^N \in \mathbb{R}^{q_z(N-1)\times n_z N}$ and $E_u^N \in \mathbb{R}^{q_u(N-1)\times n_u N}$ can be defined in analogous fashion. These matrices map the ensemble state vector to the differences in the tracked states between trajectories.

Making use of equations (14), (15), (16), (17), and (18) as well as equations (19), (20), (21), (22), and (23), we can complete now the formulation of the deterministic approximant:

$$\left.\begin{array}{ll} \text{minimize} & J_E = \mathbb{E}\left[\widehat{J}_E\right] + \mathrm{dp} \cdot R\left(\widehat{J}_E\right) \\ \text{subject to} & \dot{\mathbf{x}}_E = f_E(\mathbf{x}_E, \mathbf{z}_E, \mathbf{u}_E, t) \\ & h_E(\mathbf{x}_E, \mathbf{z}_E, \mathbf{u}_E, t) = 0 \\ & I_G g_L \le g_E(\mathbf{x}_E, \mathbf{z}_E, \mathbf{u}_E, t) \le I_G g_U \\ & E_x^N \mathbf{x}_E = 0 \\ & E_z^N \mathbf{z}_E = 0 \\ & E_u^N \mathbf{u}_E = 0 \\ & \psi_E\left(t_0, t_f, \mathbf{x}_E(\omega, t_0), \mathbf{x}_E\left(\omega, t_f\right)\right) = 0 \end{array}\right\}, \quad (24)$$

where $I_G = \left[\mathbb{I}_{n_g} \cdots \mathbb{I}_{n_g}\right]^T \in \mathbb{R}^{n_g N \times n_g}$.

2.2. Application to Flight Planning

2.2.1. Modelling Assumptions. We consider a free-routing airspace and 3-DoF point-mass model based on BADA 3 [17]. We restrict ourselves to the analysis of the cruise phase for the sake of illustration. In addition, we assume the constant flight level and airspeed profiles. Note however that our methodology could be extended to full 4D problems. We consider an ellipsoidal Earth as in the WGS84 model (which offers slightly more precision than a spheroid model), with radii of curvature of ellipsoid meridian and prime vertical denoted by R_M and R_N, respectively. We take the wind and temperature fields from an EPS forecast and compute density with the ideal gas law (as the pressure is determined by the flight level). We assume the heading as a control variable instead of the bank angle, thus allowing it to change instantaneously.

All in all, aircraft dynamics can be described by the following set of differential equations expressed in the Geographic Reference System (GRS) coordinate system (f in quation (12)):

$$\dot{\mathbf{x}} = \frac{d}{dt}\begin{bmatrix} \phi \\ \lambda \end{bmatrix} = \begin{bmatrix} (R_N(\phi) + h)^{-1}(v\cos(\chi) + w_x(\phi, \lambda, t)) \\ (R_M(\phi) + h)^{-1}\cos^{-1}(\phi)\left(v\sin(\chi) + w_y(\phi, \lambda, t)\right) \end{bmatrix}, \quad (25)$$

where ϕ is the latitude, λ is the longitude, v is the true airspeed, h is the geodetic altitude, χ is the heading, and w_x and w_y are the zonal and meridional components of the wind. The control vector is composed by the heading χ.

2.2.2. System Reformulation. We reformulate the dynamical system above as a differential-algebraic system (DAE) with the addition of the ground speed v_G as an algebraic variable and the course ψ as a control variable, linked to the remaining variables by two new equality constraints. The reformulated system is given by the dynamical function:

$$\frac{d}{dt}\begin{bmatrix}\phi\\ \lambda\end{bmatrix} = \begin{bmatrix}(R_N + h)^{-1} v_G \cos\psi\\ (R_M + h)^{-1} \cos^{-1}(\phi) v_G \sin\psi\end{bmatrix}, \tag{26}$$

and the equality constraints (h in equation (12)):

$$\begin{aligned} v_G \cos\psi &= v \cos(\chi) + w_x(\phi, \lambda, t),\\ v_G \sin\psi &= v \sin(\chi) + w_y(\phi, \lambda, t). \end{aligned} \tag{27}$$

We add the inequality constraint:

$$v_G \geq 0 \tag{28}$$

to ensure uniqueness of v_G and ψ (otherwise, $(-v_G^*, \psi^* + \pi/2)$ would produce the same left-hand side of equation (27) as (v_G^*, ψ^*)).

2.2.3. Time to Distance Transformation. We apply a coordinate transformation to make the distance flown along the route (s) be the new independent variable. This allows us to apply our methodology in a manner that is consistent with existing planning and flight procedures (again, see the discussion in [14]). As a consequence, the time t becomes a state variable, and the new dynamical function can be obtained by dividing the time derivatives by $ds/dt = v_G$:

$$\frac{d}{ds}\begin{bmatrix}\phi\\ \lambda\\ t\end{bmatrix} = \begin{bmatrix}(R_N + h)^{-1} \cos\psi\\ (R_M + h)^{-1} \cos^{-1}(\phi) \sin\psi\\ v_G^{-1}\end{bmatrix}. \tag{29}$$

All constraints remain the same as in the untransformed system of differential-algebraic equations.

2.2.4. Problem Statement. An ensemble forecast contains a set of ensemble members, each one defining a different wind forecast (and, therefore, different functions w_x and w_y). Consider the ensemble contains N members, then we define N scenarios, each one having weight $w_k = 1/N$. We choose to track the course ψ, i.e., the function $\psi(s)$ is the same in every scenario (thus, we do not need to implement scenario-specific versions). As a consequence of (29), this implies that the evolution of the latitude ϕ is unique (as it only depends on the evolution of the unique variable ψ) and λ is also unique (as it only depends on ϕ and ψ). Therefore, the position variables also act like tracked variables, which is a desired goal (since we want to obtain a unique route).

We can define the dynamical system associated with the trajectory ensemble with the dynamical function:

$$\frac{d}{ds}\begin{bmatrix}\phi\\ \lambda\\ t_1\\ \vdots\\ t_N\end{bmatrix} = \begin{bmatrix}(R_N + h)^{-1} \cos\psi\\ (R_M + h)^{-1} \cos^{-1}(\phi) \sin\psi\\ 1/v_{\mathrm{G},1}\\ \vdots\\ 1/v_{\mathrm{G},N}\end{bmatrix},$$

$$\begin{bmatrix}v_{\mathrm{G},1} \cos(\psi)\\ \vdots\\ v_{\mathrm{G},N} \cos(\psi)\\ v_{\mathrm{G},1} \sin(\psi)\\ \vdots\\ v_{\mathrm{G},N} \sin(\psi)\end{bmatrix} = \begin{bmatrix}v \cos(\chi_i) + w_{y,1}(\phi, \lambda)\\ \vdots\\ v \cos(\chi_i) + w_{y,N}(\phi, \lambda)\\ v \sin(\chi_i) + w_{x,1}(\phi, \lambda)\\ \vdots\\ v \sin(\chi_i) + w_{x,N}(\phi, \lambda)\end{bmatrix}. \tag{30}$$

The boundary conditions are

$$\begin{aligned} &(\phi(0), \lambda(0)) = (\phi_0, \lambda_0),\\ &\left(\phi(s_f), \lambda(s_f)\right) = \left(\phi_f, \lambda_f\right),\\ &t_i(0) = 0 \forall i \in \{1, \cdots, N\},\\ &t_{f,\min} \leq t_i(r_f) \leq t_{f,\max} \forall i \in \{1, \cdots, N\}, \end{aligned} \tag{31}$$

where $t_{f,\min}$ and $t_{f,\max}$ are scalar decision variables.

We complete the definition of the discretized robust optimal control problem by adding the cost function. We apply the robust optimal control methodology to find routes that minimize a weighted sum of average fuel consumption and flight time dispersion (weighted with the dispersion penalty parameter dp). The cost functional to minimize is then

$$J = \mathbb{E}\left[t_i(r_f)\right] + \mathrm{dp} \cdot \underbrace{\left(\max\left(t_i(r_f)\right) - \min\left(t_i(r_f)\right)\right)}_{\mathrm{uncertainty\,in}\,t_f}. \tag{32}$$

Note that $(\max(t_i(r_f)) - \min(t_i(r_f)))$ is the difference between the earliest and the latest arrival time.

With this cost functional, the parameter dp regulates the solution flight plan depending on the preferences of the flight planner. High values of dp will produce more predictable trajectories by avoiding regions where the wind is more unpredictable. Low values of the parameter will produce flight plans that are more efficient in average but less predictable.

3. Trajectory Predictor

The trajectory predictor determines the aircraft trajectory for a weather scenario. The objective of the TP is to provide the aircraft variable values, i.e., flight times, aircraft mass, and ground speed, along the previously defined route (sequence of nodes/waypoints) provided by the ROC problem.

Mass at discrete node/waypoint $i + 1$ is computed following quation (33) (note that this equation can be applied because the aircraft is flying at constant speed and altitude):

$$m_{i+1} = \sqrt{\frac{A_{\mathrm{aux}}}{B_{\mathrm{aux}}}} \tan(E + F), \tag{33}$$

where

$$
\begin{aligned}
A_{\text{aux}} &= \eta \cdot A,\\
B_{\text{aux}} &= \eta \cdot B,\\
\eta &= \frac{C_{f1}}{(1000 \cdot 60)} \cdot \left(1 + \frac{v \cdot kt2ms}{C_{f2}}\right),\\
A &= 0.5 \cdot \rho \cdot S \cdot v^2 \cdot CD_{0_{CR}},\\
B &= \frac{2 \cdot CD_{2_{CR}} \cdot g}{(0.5 \cdot \rho \cdot S \cdot v^2)},\\
E &= \arctan\left(\sqrt{\frac{B_{\text{aux}}}{A_{\text{aux}}}} \cdot m_i\right),\\
F &= \sqrt{B_{\text{aux}} \cdot A_{\text{aux}}} \cdot (t_i - t_{i+1}),
\end{aligned}
\tag{34}
$$

where C_{f1} and C_{f2} are first and second thrust-specific fuel consumption coefficient, respectively, v is the true airspeed (TAS), $kt2ms$ is a constant to convert m/s to knots, S is the reference wing surface area, ρ is the air density, $CD_{0_{CR}}$ is the parasitic drag coefficient (cruise), $CD_{2_{CR}}$ is the induced drag coefficient (cruise), g is the gravity, t_i and t_{i+1} are the flight time at discrete node/waypoint i and node/waypoint $i+1$, respectively, and m_i is the aircraft mass at node/waypoint i.

Ground speed is computed as

$$
v_{G_{i+1}} = \sqrt{\left(v^2 - w_{yPr}^2\right)} + w_{xPr}, \tag{35}
$$

where

$$
\begin{aligned}
w_{xPr} &= \cos\left(\psi_{(i)\to(i+1)}\right) \cdot w_y + \sin\left(\psi_{(i)\to(i+1)}\right) \cdot w_x,\\
w_{yPr} &= \cos\left(\psi_{(i)\to(i+1)}\right) \cdot w_x - \sin\left(\psi_{(i)\to(i+1)}\right) \cdot w_y.
\end{aligned}
\tag{36}
$$

Note that $\psi_{(i)\to(i+1)}$ is the aircraft course between node/waypoint i and node/waypoint $i+1$ calculated as shown in equation (37) to (38).

$$
\psi_{(i)\to(i+1)} = \operatorname{sign}(\lambda_{i+1} - \lambda_i) \cdot \frac{\pi}{2}, \quad \forall \phi_i = \phi_{i+1}, \tag{37}
$$

$$
\psi_{(i)\to(i+1)} = \arctan 2\left(\lambda_{i+1} - \lambda_i, ln\left[\frac{\tan\left(\pi/4 - \phi_i/2\right)}{\tan\left(\pi/4 - \phi_{i+1}/2\right)}\right]\right), \quad \forall \phi_i \neq \phi_{i+1}. \tag{38}
$$

Flight time at node/waypoint $i+1$ is computed as the distance (d) between nodes/waypoints i and $i+1$ over v_G. It is assumed that v_G is constant between nodes/waypoints. Distance between nodes/waypoint is the orthodromic distance.

$$
t_{i+1} = t_i + \frac{d_{(i)\to(i+1)}}{v_{G_{i+1}}}. \tag{39}
$$

4. Wind Data and Modelling

4.1. Wind Data. In order to incorporate wind into the models, we make use of two meteorological products, namely, EPS, which provide ensemble-wise uncertainty information and reanalysis, considered to be a sufficiently good approximation to weather's realization.

4.1.1. EPS. Uncertainty of wind fields will be derived from EPS. Ensemble forecasting is a prediction technique that generates a representative sample of the possible future states of the atmosphere. An ensemble forecast is a collection of typically 10 to 50 weather forecasts (referred to as members) with a common valid time, which can be obtained using different Numerical Weather Prediction (NWP) models with varying initial conditions. Each forecast is based on a model which is close, but not identical, to the best estimate of the model equations, thus representing also the influence of model uncertainties on forecast error. Thus, the spread of solutions can be used as a measure of uncertainty. In this paper, we focus on the output data of the global ensemble forecast system ECMWF EPS. Data can be accessed (among others) at the TIGGE dataset by the European Center for Medium-Range Weather Forecasts (ECMWF) [18] (http://apps.ecmwf.int/datasets/http://apps.ecmwf.int/datasets/).

(1) ECMWF EPS. The European Centre for Medium-Range Weather Forecasts EPS (ECMWF EPS) is based on 51 ensemble members with approximately 32 km resolution up to forecast day 10 and 65 km resolution thereafter, with 62 vertical levels.

4.1.2. Reanalysis. Meteorological reanalysis is based on meteorological data assimilation. The aim is at assimilating historical observational data spanning an extended period, using a given model. Reanalysis is considered to be the best estimate on many variables (such as winds and temperature).

ECMWF ERA-5 reanalysis will be used in the course of the validation activities. The data assimilation system used to produce ERA-5 includes a 4-dimensional variational analysis with a 12-hour analysis window. The spatial resolution of the dataset is approximately 31 km (in the high resolution version) on 32 vertical levels from the surface up to 0.01 hPa. ERA-5 products are normally updated once daily, with a delay of two months to allow for quality assurance and for correcting technical problems with the production, if any. ERA-5 data can be downloaded from the ECMWF Public Datasets.

4.2. Wind Approximation. Note that in order to incorporate winds in Problem (24), functions $w_x(\phi, \lambda, t)$: $\mathbb{R}^3 \to \mathbb{R}$ and $w_y(\phi, \lambda, t)$: $\mathbb{R}^3 \to \mathbb{R}$ in equation (27) must ideally be class C^2 functions, i.e., continuous and twice derivable functions (in lack of this, they should be at least Lipschitz continuous functions). This in practice translates into the need of approximating raw, tabular data from either EPS or reanalysis into smooth functions with the abovementioned properties.

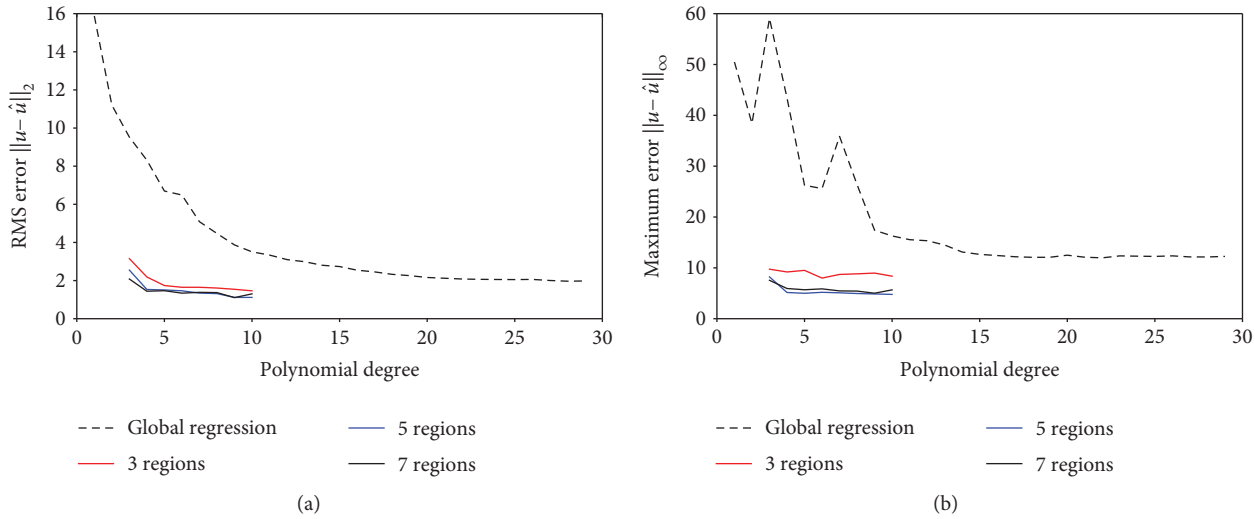

FIGURE 2: Polynomial approximation accuracy in L^2 (RMS) norm (a) and L^∞ (maximum) norm (b) [14].

We describe two possible approximations: a multiregion polynomial regression and a spline interpolation method. Approximation errors cannot be obviated; they end up distorting results as we will show in the sequel.

4.2.1. Multiregion Polynomial Regression. We seek to compute an approximation of the wind field in the area of interest. We subdivide this area into regions and consider an approximating polynomial for each region:

$$p_{a,s}(\phi, \lambda) = \sum_{\substack{i+j \le n \\ i,j \ge 0}} a_{s,ij} \phi^i \lambda^j, \tag{40}$$

where s denotes the index of the region.

We compute the coefficients $a_{s,ij}$ by solving the following least squares problem:

$$\min_{a_{s,ij} \in \mathbb{R}} \sum_{s=1}^{N_{\text{regions}}} \sum_{k=1}^{N} \sum_{l=1}^{M} \left(p_{a,s}(\phi_{kl,s}, \lambda_{kl,s}) - u_{kl,s} \right)^2, \tag{41}$$

where the points $(\phi_{kl,s}, \lambda_{kl,s})$ are generated by applying to a rectangular, equispaced grid on $[0,1] \times [0,1]$ the affine transformation $T_s : \mathbb{R}^2 \to \mathbb{R}^2$ such that $T_s([0,1] \times [0,1]) = R_s$, where $R_s \subset \mathbb{R}^2$ denotes the region number s. The values $u_{kl,s}$ are generated by sampling a cubic spline interpolant of the original grid values at this new grid.

We also add continuity and differentiability requirements at the boundaries between regions. Consider the boundary between region s and region $s+1$ and parametrize it by $\xi_s \in [0,1]$ by building the affine transformations $(\phi_s(\xi_s), \lambda_s(\xi_s))$. By composition, we can build the polynomials:

$$\begin{aligned} b_{a,s}(\xi_s) &= p_{a,s}(\phi_s(\xi_s), \lambda_s(\xi_s)), \\ b_{a,s+1}(\xi_s) &= p_{a,s+1}(\phi_s(\xi_s), \lambda_s(\xi_s)), \end{aligned} \tag{42}$$

that represent the value of the field approximation at the boundaries at each one of the adjacent regions. By construction, both b_s and b_{s+1} are polynomials of degree n in ξ_s; therefore, by equating them at $n+1$ points, we can guarantee that they are equal. We choose $n+1$ equispaced points along the boundary, $\{\xi_{s,m}\}$ $(m \in \{0, \cdots, n\})$ and augment problem (41) with the equality constraints $b_{a,s}(\xi_{s,m}) = b_{a,s+1}(\xi_{s,m})$. Note that these are constraints on the value of the coefficients a, which are the decision variables for this problem. This constraints guarantee continuity between regions.

In order to deal with differentiability constraints, we similarly define the polynomials:

$$\begin{aligned} b^{q,r}_{a,s}(\xi_s) &= \frac{\partial^q}{\partial \phi^q} \frac{\partial^r}{\partial \lambda^r} p_{a,s}(\phi_s(\xi_s), \lambda_s(\xi_s)), \\ b^{q,r}_{a,s+1}(\xi_s) &= \frac{\partial^q}{\partial \phi^q} \frac{\partial^r}{\partial \lambda^r} p_{a,s+1}(\phi_s(\xi_s), \lambda_s(\xi_s)), \end{aligned} \tag{43}$$

where $q, r \ge 0$ are the orders of the differentiability constraints. The degree of this polynomial on ξ is $n - q - r$, so we only need to equate $b^{q,r}_{a,s}$ and $b^{q,r}_{a,s+1}$ in $n + 1 - q - r$ points in order to enforce differentiability across boundaries.

Figure 2 presents the approximation error of the global and regional regression approaches, measured in a band of $\pm$ 3 deg around the reference trajectory as computed in [14]. A significant improvement can be observed in both number of regions and degree of the polynomial, thus justifying the advantages of this approach. Nonetheless, a residual error always persists and that is why we resort to spline interpolation.

4.2.2. Spline Interpolation. An alternative method to do wind field spline interpolation is a well-established field of knowledge. Amodei and Benbourhim in [19] introduced a new family of vector field splines with application to wind fields. More recently, Le Guyader et al. [20] studied the use of a spline-bases approximation considering conservative vector

fields as it happens with winds (winds derive from temperature potentials). We herein use the b-spline interpolation functionality implemented in CasADi [21], a symbolic framework for algorithmic differentiation and numeric optimization. The spline S takes values in the region of interest $[\lambda, \phi]$ and maps them to $\mathbb{R}$.

4.3. Wind Errors. To illustrate errors with both wind approximation models and its effects in the results to Problem (24), we bring herein an example. It corresponds to case 5th October 2016 in the single O-D flight case study, so please refer therein for more details.

Needless to say, it can be readily observed comparing Figures 3(a) and 3(b) that the wind uncertainty (computed as the standard deviation of wind norm across all members in the EPS, see equation (44)) in both multiregion polynomial regression and spline interpolation approaches substantially differ. One could qualitatively say that there is a *displacement of the wind uncertainty*. This is mainly due to the fact that wind approximation errors (see definition bellow) committed using the multiregion polynomial regression itself are of the same order of magnitude as the uncertainty. This fact can be observed in Figure 3(d); indeed, the higher the uncertainty, the higher the error. This is of course expected, since regression is a smoothing technique. On the contrary (see Figure 3(c)), spline interpolation errors are neglectable with orders of magnitude of $1 \cdot e - 12$.

$$\sigma_w = \sqrt{\sigma_{w_x}^2 + \sigma_{w_y}^2}, \tag{44}$$

where σ_w is the wind uncertainty, and σ_{w_x} and σ_{w_y} represent the standard deviation of wind east-west and north-south components across all members in the EPS, respectively.

$$\begin{aligned} \sigma_{w_x} &= \sqrt{\sum_{n=1}^{N} \frac{\left(w_{x_n} - \bar{w}_x\right)}{N}}, \\ \sigma_{w_y} &= \sqrt{\sum_{n=1}^{N} \frac{\left(w_{y_n} - \bar{w}_y\right)}{N}}, \end{aligned} \tag{45}$$

where w_{x_n} and w_{y_n} are the wind east-west and north-south components of member n in the EPS and $\bar{w}_x$ and $\bar{w}_y$ represent the average with east-west and north-south components across all members in the EPS, respectively, being N is the number of members in the EPS, i.e.,

$$\begin{aligned} \bar{w}_x &= \sum_{n=1}^{N} \frac{w_{x_n}}{N}, \\ \bar{w}_y &= \sum_{n=1}^{N} \frac{w_{y_n}}{N}. \end{aligned} \tag{46}$$

Let us define wind uncertainty error as $\varepsilon_{\sigma_w} = \sigma_{w_f} - \sigma_{w_a}$, where σ_{w_f} is the standard deviation of wind across all members in the EPS forecast (considering raw, tabular wind data) and σ_{w_a} is the standard deviation of wind across all members in the EPS (considering the polynomial/n-spline approximation functions.)

Figure 4 provides evidence on errors' effects in the calculated trajectories (solving Problem (24) with both wind approximations). While darker trajectories (representing the problem computed with low dp values, thus weighting less the effects of uncertainty) are very similar, brighter ones behave in rather disimilar manner. Indeed, in Figure 4(b), trajectories computed with the multiregion polynomial regression approximation and high dp values (bright colors) seek to deviate southwards to avoid a region of high uncertainty (according to the approximated wind). This region is indeed biased by approximation errors. If one looks at Figure 4(a) (approximated with splines and thus with no error), the high-uncertainty region has moved slightly south and thus trajectories do not go south anymore, rather go straight.

We bring now readers' attention to Figure 5. Flight times and flight dispersions are represented for different dp values in boxplots, which provide qualitative information on quartiles (upper and lower box) and median (red line). The whiskers indicate variability outside the upper and lower quartiles. Outliers are plotted (should they exist) as individual points. All in all, one can readily have an idea of median (or mean) flight times and dispersions. The solution to Problem (24) should provide increasing average flight times and reduced time dispersions as dp values grow. This is as expected in Figure 5(a), where results are represented with the direct output of the optimization problem (in which wind reads as in the approximated functions). However, if ones takes the obtained discrete path (λ, θ, h) and computes flight times using a trajectory predictor (TP) over the original raw, tabular wind, results do not show this behaviour anymore. This can be noticed in Figure 5(b), e.g., comparing dp = 0 and dp = 1. Also, looking now at Figure 5(c), which includes the same simulation with the spline interpolation (note that herein wind errors are zero), flight times are substantially different; yet, dispersions are consistent.

Please refer to Table 1 for quantitative data, including also data for fuel consumptions and fuel dispersions with spline wind approximation. Remark also that this analysis has been made for the whole scenario in Case 1 and this reasoning holds for the whole set of flights. These findings motivate the use of precise wind approximation methodology, though reader should advert there is always a trade-off between accurate modelling and solvability. All in all, we resorted to spline interpolation to circumvent these problems.

5. Key Performance Indicators (KPIs)

The following variables will be analyzed:

(i) Total flight time (FT)

(ii) Total fuel consumption (FC)

For the sake of simplicity, henceforth, variable x will be sued (denoting either FT or FC interchangeably). Note the reader that the solution to the robust flight planning provides

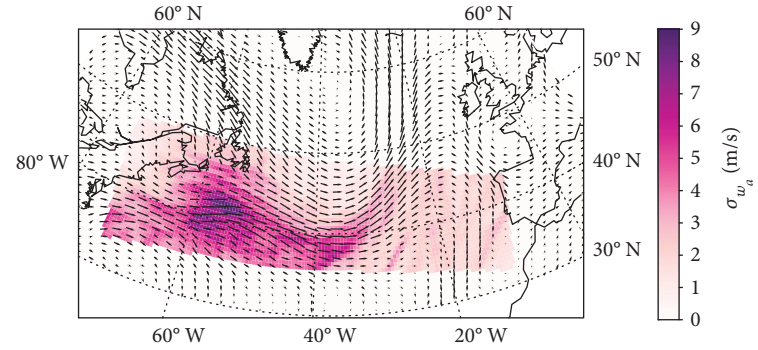

(a) Wind uncertainty (n-spline approx.)

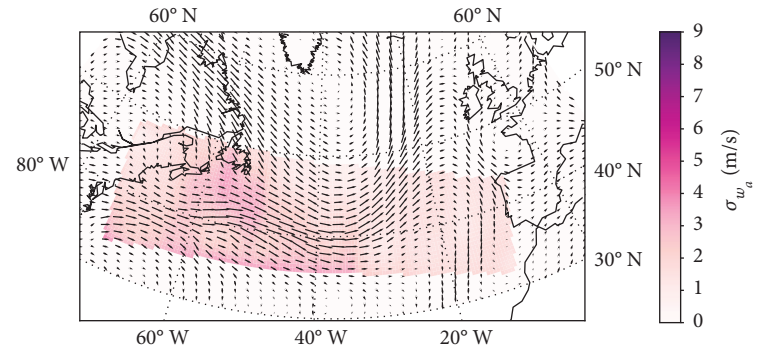

(b) Wind uncertainty (polynomial approx.)

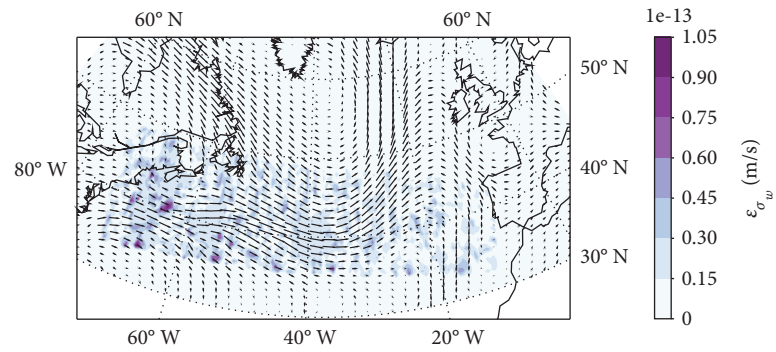

(c) Wind uncertainty approximation error (n-spline approx.)

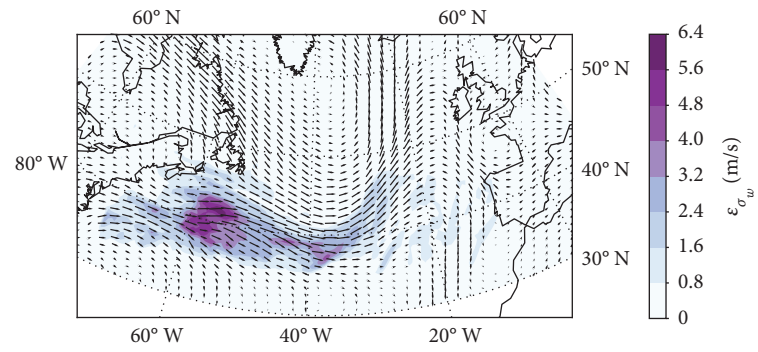

(d) Wind uncertainty approximation error (polynomial approx.)

Figure 3: Wind approximations and associated errors (in m/s).

a discrete number N (equal to the number of members in the ensemble forecast) of possible values for both flight time and fuel consumption. Thus, in order to compare the robust flight planning results with hypothetical realizations (considered to be that of the reanalysis), we should statistically characterize flight times and fuel consumptions. Figure 6 sketches the

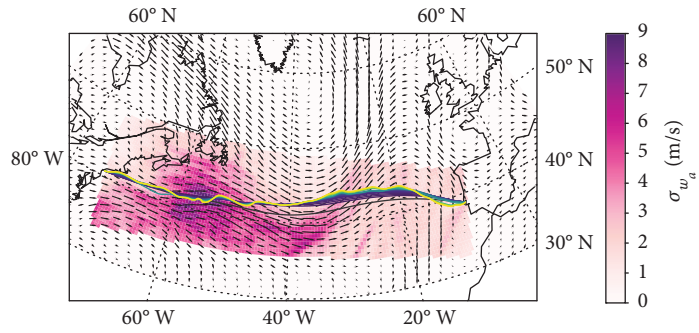

(a) Using n-spline wind approximation

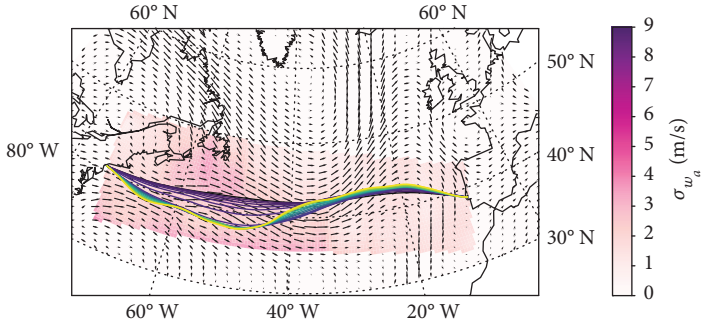

(b) Using polynomial approximation

Figure 4: Optimal paths (for different dp values).

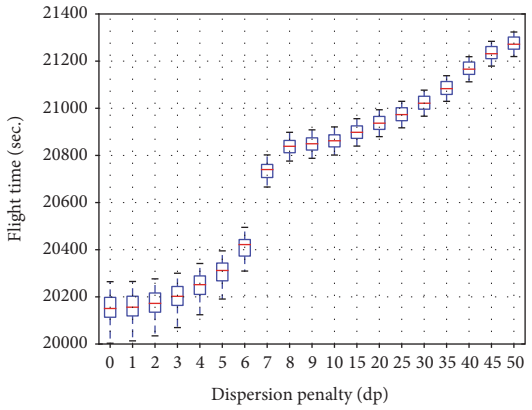

(a) Using wind polynomial approx

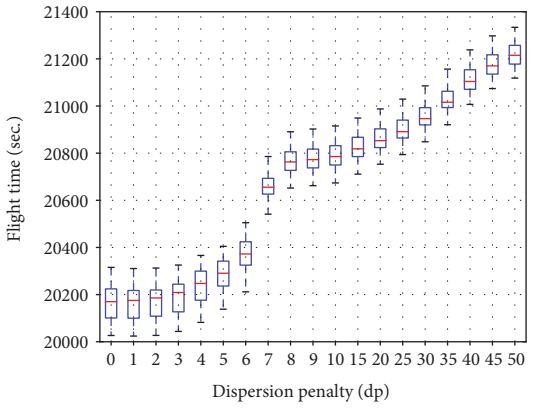

(b) Using wind polynomial approx and TP

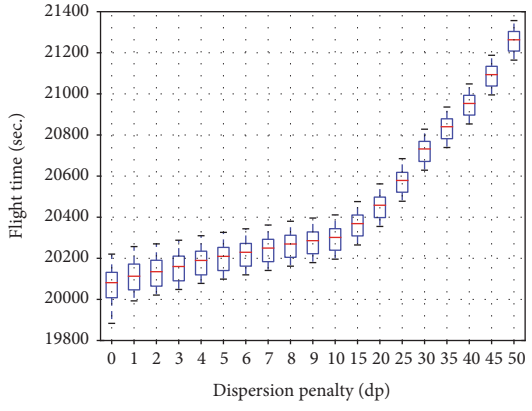

(c) Using wind spline approx

Figure 5: Boxplot diagrams showing flight dispersion results for different dp values.

Table 1: Top five days in terms of time and fuel dispersion. Tol = 30 sec. (FT) and 70 kg (FC).

Variable	Date	FT (sec.)					FC (kg)				
		dp0	dp5	dp10	dp15	dp20	dp0	dp5	dp10	dp15	dp20
$\mathbb{R}(x)^{R-Trj}$	2016-Oct-05	337.0	227.6	215.4	211.1	207.1	487.2	328.8	311.0	304.7	298.8
$\bar{x}^{R-Trj}$		20073.5	20203.0	20296.9	20365.0	20454.4	30525.4	30712.5	30848.2	30946.4	31075.5
x^{Rea}		20205.7	20295.1	20383.3	20450.0	20538.4	30716.5	30845.6	30972.9	31069.2	31196.7
Δx^{Mean}		-132.2	-92.1	-86.4	-85.1	-84.0	-191.1	-133.0	-124.7	-122.8	-121.3
$\mathbb{B}(x)^{IQR}$		False	False	False	False	False	False	False	False	False	False
$\mathbb{B}(x)^{Exp\pm Tol}$		False	False	False	False	False	False	False	False	False	False
$\%x^{Rea\pm Tol}$		16.0	20.0	24.0	24.0	24.0	20.0	28.0	30.0	34.0	34.0
$\mathbb{R}(x)^{R-Trj}$	2016-Sep-05	314.2	247.0	225.7	203.4	182.6	451.8	354.9	324.2	291.9	261.6
$\bar{x}^{R-Trj}$		21185.9	21327.5	21477.4	21605.9	22001.7	32129.1	32332.7	32548.1	32732.5	33300.0
x^{Rea}		21217.1	21358.7	21509.5	21650.4	22025.4	32174.1	32377.6	32594.1	32796.4	33333.9
Δx^{Mean}		-31.2	-31.2	-32.1	-44.5	-23.6	-45.0	-44.9	-46.0	-63.9	-33.9
$\mathbb{B}(x)^{IQR}$		True	True	True	True	True	True	True	True	True	True
$\mathbb{B}(x)^{Exp\pm Tol}$		False	False	False	False	True	True	True	True	True	True
$\%x^{Rea\pm Tol}$		36.0	32.0	30.0	30.0	26.0	56.0	48.0	48.0	46.0	50.0
$\mathbb{R}(x)^{R-Trj}$	2016-May-05	300.7	176.1	129.5	107.4	100.0	435.7	254.9	187.3	155.1	144.3
$\bar{x}^{R-Trj}$		19584.8	19751.8	20046.4	20256.5	20447.0	29818.2	30060.0	30486.2	30789.8	31064.8
x^{Rea}		19578.0	19750.7	20054.3	20249.2	20443.3	29808.4	30058.4	30497.6	30779.2	31059.5
Δx^{Mean}		6.8	1.1	-7.9	7.4	3.7	9.8	1.5	-11.4	10.6	5.3
$\mathbb{B}(x)^{IQR}$		True	True	True	True	True	True	True	True	True	True
$\mathbb{B}(x)^{Exp\pm Tol}$		True	True	True	True	True	True	True	True	True	True
$\%x^{Rea\pm Tol}$		62.0	66.0	74.0	66.0	62.0	84.0	82.0	86.0	94.0	94.0
$\mathbb{R}(x)^{R-Trj}$	2016-Jan-25	261.7	180.2	173.2	168.1	149.0	380.2	261.7	251.5	244.1	215.8
$\bar{x}^{R-Trj}$		18981.2	19025.9	19083.4	19153.7	19638.3	28942.4	29007.3	29090.8	29192.9	29895.7
x^{Rea}		19011.9	19070.8	19128.9	19199.9	19700.5	28987.0	29072.6	29157.0	29260.0	29985.7
Δx^{Mean}		-30.7	-44.9	-45.5	-46.2	-62.2	-44.6	-65.3	-66.1	-67.1	-90.0
$\mathbb{B}(x)^{IQR}$		False	False	False	False	False	False	False	False	False	False
$\mathbb{B}(x)^{Exp\pm Tol}$		False	False	False	False	False	True	True	True	True	False
$\%x^{Rea\pm Tol}$		34.0	32.0	26.0	24.0	22.0	62.0	52.0	50.0	50.0	38.0
$\mathbb{R}(x)^{R-Trj}$	2016-May-20	234.8	189.5	166.6	151.9	121.4	341.3	275.4	241.9	220.5	175.7
$\bar{x}^{R-Trj}$		18873.7	18976.7	19140.0	19260.1	19778.1	28786.1	28935.8	29173.1	29347.3	30098.0
x^{Rea}		18895.8	18996.3	19145.6	19253.6	19768.9	28818.2	28964.3	29181.1	29337.9	30084.9
Δx^{Mean}		-22.1	-19.6	-5.5	6.5	9.1	-32.2	-28.5	-8.0	9.4	13.2
$\mathbb{B}(x)^{IQR}$		True	True	True	True	True	True	True	True	True	True
$\mathbb{B}(x)^{Exp\pm Tol}$		True	True	True	True	True	True	True	True	True	True
$\%x^{Rea\pm Tol}$		42.0	46.0	64.0	64.0	70.0	62.0	68.0	82.0	86.0	90.0

solutions provided by the robust trajectory predictor (including its statistical characterization in quartiles and mean values) and the realization (based on reanalysis).

Let us consider the following sets:

(i) $\mathcal{F} \rightarrow$ (set of flights)

(ii) $\mathscr{DP} \rightarrow$ (set of dp values)

(iii) $\mathscr{S} \rightarrow$ (set of forecast steps in the EPS)

(iv) $\mathscr{N} \rightarrow$ (set of ensemble *members* in the EPS)

Let us consider the following variables:

$$\begin{aligned} &\mathrm{x}^{\mathrm{R-Trj}}_{i,j,k,n}, \quad \forall i \in \mathscr{F}, \forall j \in \mathscr{DP}, \forall k \in \mathscr{S}, \forall n \in \mathscr{N}; \\ &\mathrm{x}^{\mathrm{Rea}}_{i,j,k}, \quad \forall i \in \mathscr{F}, \forall j \in \mathscr{DP}, \forall k \in \mathscr{S}; \end{aligned} \tag{47}$$

where super-index R-Trj refers to variables obtained from the robust trajectory predictor and computed using EPS forecasts, and super-index Rea refers to the trajectory flown under a hypothetical realization of wind (considered to be the reanalysis).

Taking mean values across all members in the EPS:

$$\bar{\mathrm{x}}^{\mathrm{R-Trj}}_{i,j,k} = \sum_{n=1}^{N} \frac{\mathrm{x}^{\mathrm{R-Trj}}_{i,j,k,n}}{N}, \quad \forall i \in \mathscr{F}, \forall j \in \mathrm{DP}, \forall k \in \mathscr{S}. \tag{48}$$

Consider also the following conditions:

$$\mathrm{x}^{\mathrm{Rea}}_{i,j,k} \in \mathrm{IQR}^{\mathrm{R-Trj}}_{i,j,k}, \quad \forall i \in \mathscr{F}, \forall j \in \mathscr{DP}, \forall k \in \mathscr{S}; \tag{49}$$

$$\mathrm{x}^{\mathrm{Rea}}_{i,j,k} \in \left[\bar{x}^{\mathrm{R-Trj}}_{i,j,k} \pm \mathrm{tol}\right], \quad \forall i \in \mathscr{F}, \forall j \in \mathscr{DP}, \forall k \in \mathscr{S}; \tag{50}$$

$$\mathrm{x}^{\mathrm{R-Trj}}_{i,j,k,n} \in \left[x^{\mathrm{Rea}}_{i,j,k} \pm \mathrm{tol}\right], \quad \forall i \in \mathscr{F}, \forall j \in \mathscr{DP}, \forall k \in \mathscr{S}, \forall n \in \mathscr{N}; \tag{51}$$

where tol is a user-specified tolerance.

Let us define the indicator functions that takes value one if the condition is true and zero elsewhere:

$$\begin{aligned} &\mathbb{1}_{\mathrm{cond.}(49),(i,j,k)} \quad \forall i \in \mathscr{F}, \forall j \in \mathscr{DP}, \forall k \in \mathscr{S}; \\ &\mathbb{1}_{\mathrm{cond.}(50),(i,j,k)} \quad \forall i \in \mathscr{F}, \forall j \in \mathscr{DP}, \forall k \in \mathscr{S}; \\ &\mathbb{1}_{\mathrm{cond.}(51),(i,j,k,n)} \quad \forall i \in \mathscr{F}, \forall j \in \mathscr{DP}, \forall k \in \mathscr{S}, \forall n \in \mathscr{N}. \end{aligned} \tag{52}$$

The flight-wise Key Validation Indicators are defined as follows:

$$\begin{aligned} \mathbb{R}(\mathrm{x})^{\mathrm{R-Trj}}_{i,j,k} &= \max_{n\in\mathscr{N}} \mathrm{x}^{\mathrm{R-Trj}}_{i,j,k,n} - \min_{n\in\mathscr{N}} \mathrm{x}^{\mathrm{R-Trj}}_{i,j,k,n}, \\ &\forall i \in \mathscr{F}, \forall j \in \mathscr{DP}, \forall k \in \mathscr{S}; \\ \Delta\mathrm{x}^{\mathrm{Mean}}_{i,j,k} &= \bar{\mathrm{x}}^{\mathrm{R-Trj}}_{i,j,k} - \mathrm{x}^{\mathrm{Rea}}_{i,j,k}, \quad \forall i \in \mathscr{F}, \forall j \in \mathscr{DP}, \forall k \in \mathscr{S}; \\ \mathbb{B}(\mathrm{x})^{\mathrm{IQR}}_{i,j,k} &= \mathbb{1}_{\mathrm{cond.}(49),(i,j,k)}, \quad \forall i \in \mathscr{F}, \forall j \in \mathscr{DP}, \forall k \in \mathscr{S}; \\ \mathbb{B}(\mathrm{x})^{\mathrm{Exp\pm Tol}}_{i,j,k} &= \mathbb{1}_{\mathrm{cond.}(50),(i,j,k)}, \quad \forall i \in \mathscr{F}, \forall j \in \mathscr{DP}, \forall k \in \mathscr{S}; \\ \%\mathrm{x}^{\mathrm{Rea\pm Tol}}_{i,j,k} &= \sum_{n\in\mathscr{N}} \frac{\mathbb{1}_{\mathrm{cond.}(51),(i,j,k,n)}}{N}, \quad \forall i \in \mathscr{F}, \forall j \in \mathscr{DP}, \forall k \in \mathscr{S}; \end{aligned} \tag{53}$$

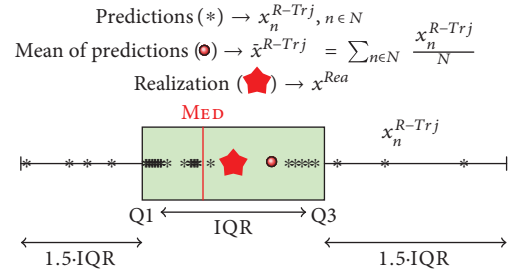

Figure 6: Schematic boxplot including the N robust prediction and the realization of a hypothetical variable.

where $\mathbb{R}(\mathrm{x})^{\mathrm{R-Trj}}_{i,j,k}$ represents the predicted flight time or fuel burnt dispersions using the robust flight planing methodology; $\Delta\mathrm{x}^{\mathrm{Mean}}_{i,j,k}$ represents the deviations of the expected value (the mean) with respect to the observation (assumed herein to be the calculated using reanalysis); $\mathbb{B}(\cdot)$ denotes boolean, and thus, the associated indicator can take value true or false, depending on whether the realization fits into the defined domains (IQR; expected prediction ± tolerances) for both flight time and fuel consumption; last but not the least, $\%(\cdot)$ denotes the percentage of predictions that fin within the realization ± a given tolerance. Notice that these indicators are calculated for all flights, all dp values and all forecast steps.

Let us also define the following aggregated KPIs:

$$\begin{aligned} \bar{\mathbb{R}(\mathrm{x})}_{j,k} &= \sum_{i\in\mathscr{F}} \frac{\mathbb{R}(\mathrm{x})^{\mathrm{R-Trj}}_{i,j,k}}{N_{\mathrm{flights}}}, \quad \forall j \in \mathscr{DP}, \forall k \in \mathscr{S}; \\ \bar{\Delta\mathrm{x}}_{j,k} &= \sum_{i\in\mathscr{F}} \frac{\Delta\mathrm{x}^{\mathrm{Mean}}_{i,j,k}}{N_{\mathrm{flights}}}, \quad \forall j \in \mathscr{DP}, \forall k \in \mathscr{S}; \\ \%\mathbb{B}(\mathrm{x})^{\mathrm{IQR}}_{j,k} &= \sum_{i\in\mathscr{F}} \frac{\mathbb{B}(\mathrm{x})^{\mathrm{IQR}}_{i,j,k}}{N_{\mathrm{flights}}}, \quad \forall j \in \mathscr{DP}, \forall k \in \mathscr{S}; \\ \%\mathbb{B}(\mathrm{x})^{\mathrm{Exp\pm Tol}}_{j,k} &= \sum_{i\in\mathscr{F}} \frac{\mathbb{B}(\mathrm{x})^{\mathrm{Exp\pm Tol}}_{i,j,k}}{N_{\mathrm{flights}}}, \quad \forall j \in \mathscr{DP}, \forall k \in \mathscr{S}; \\ \%\bar{\mathrm{x}}^{\mathrm{Rea\pm Tol}}_{j,k} &= \sum_{i\in\mathscr{F}} \frac{\%\mathrm{x}^{\mathrm{Rea\pm Tol}}_{i,j,k}}{N_{\mathrm{flights}}}, \quad \forall j \in \mathscr{DP}, \forall k \in \mathscr{S}; \end{aligned} \tag{54}$$

where they provide an aggregated vision over all flights in the different scenarios of the same variables as above, namely, flight time and fuel burnt dispersions, and deviations of the predicted mean flight time and fuel burnt with respect to the observation.

6. Case Studies

Two case studies have been selected in order to characterize and illustrate potential reductions in both flight time and fuel burnt uncertainty, namely,

(1) A single origin-destination flight (over the North Atlantic) along a set of characteristic days along year

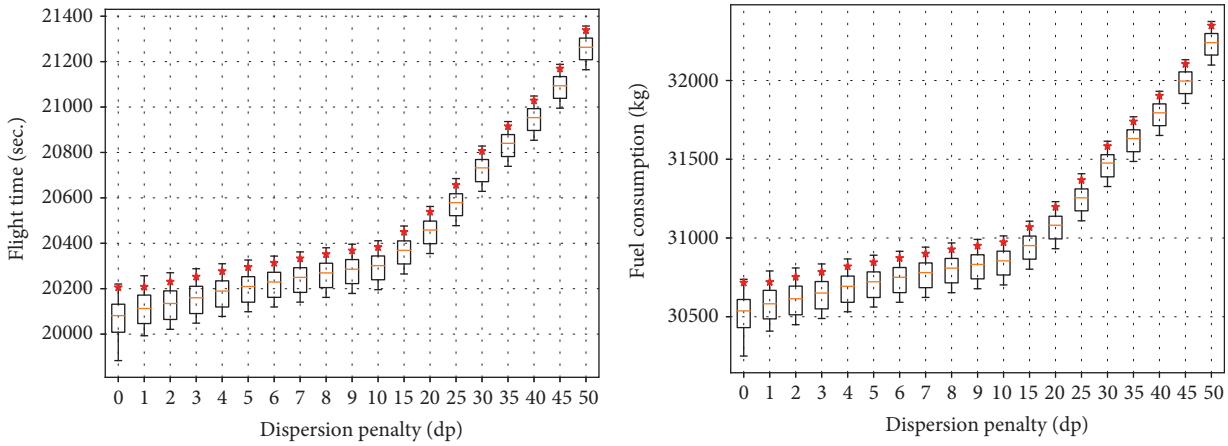

(a) Flight times

(b) Fuel consumptions

Figure 7: 2016-Oct-05 results: boxplots denote predicted uncertainties (based on EPS data and computed using the robust flight planning algorithm); red stars denote realized values (based on reanalysis data).

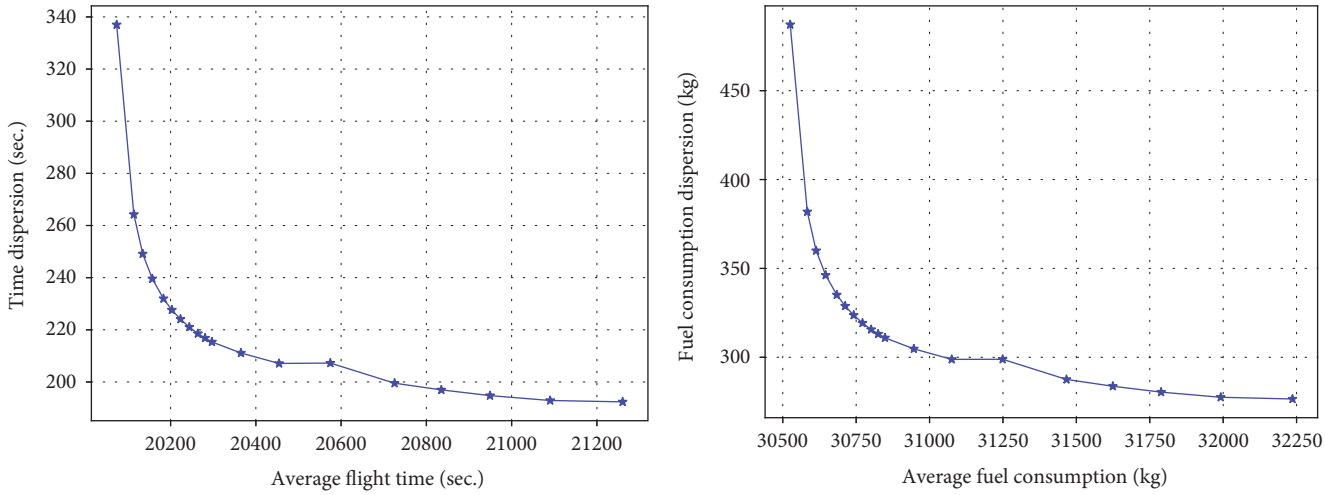

(a) Pareto front time dispersion vs. average flight time

(b) Pareto front fuel dispersion vs. average fuel consumption

Figure 8: 2016-Oct-05: trade-off solutions of the problem.

2016. The flights are computed considering a single step of 6 hours, i.e., a characteristic times at flight dispatching level. Please refer to Section 6.1 for additional details

(2) A multiple origin-destination set of flights in a representative day, i.e., day with more time dispersion in the single origin-destination case study. The flights are computed considering multiple steps, from 0 to 48 hours, i.e., characteristic times at flow management level. Please refer to Section 6.2 for additional details

All robust flight planning have been simulated using the robust flight planning approach in Section 2.1, considering EPS forecasts as input data and approximated using the spline interpolation in Section 4. The realization of the trajectory is computed using the route provided by the robust flight planning (a sequence of (lat, long) coordinates) and considering reanalysis wind data approximated by spline interpolation. A trajectory predictor is used for that purpose. KPIs introduced in Section 5 are used to quantify results.

6.1. Single O-D Flight, Single Step, Multiple Days. We choose a flight between KJFK and LPPT, flying at constant barometric FL380, and constant Mach of 0.82. A free routing airspace is considered. Aircraft is modelled as a A330 BADA3 model with an initial mass of 200000 kg. We select a set of characteristic days along year 2016, all together 72 days (1st, 5th, 10th, 15th, 20th, and 25th of each month). The corresponding EPS forecasts produced at 00.00 of the day and with forecast of 06 step are considered. We present in Table 1 the top five days in terms of time and fuel dispersions, respectively. We proceed on discussing the results for the day with the greatest dispersion (2016-Oct-05, herein termed representative day).

6.1.1. Representative Day "2016-Oct-05." Figure 7 includes boxplot information on flight times, fuel consumptions, time dispersions, and fuel burnt dispersions for this representative

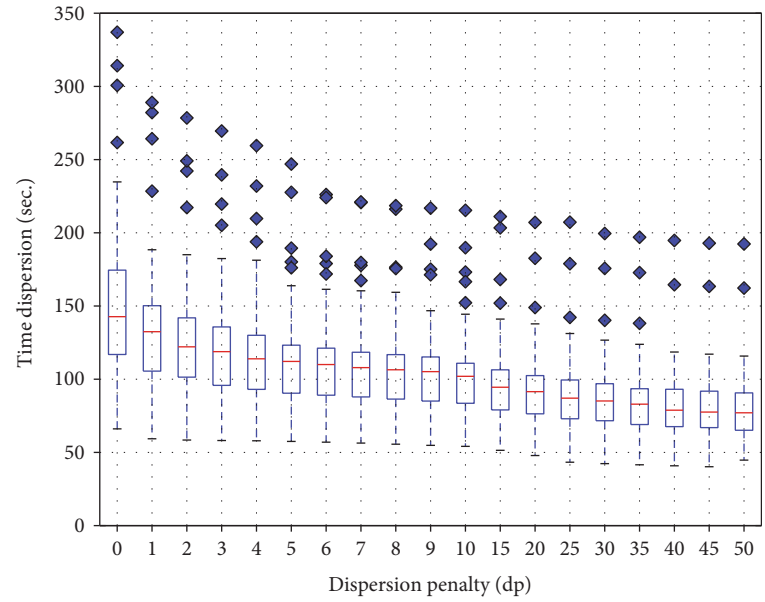

(a) Final time dispersion (max-min value)

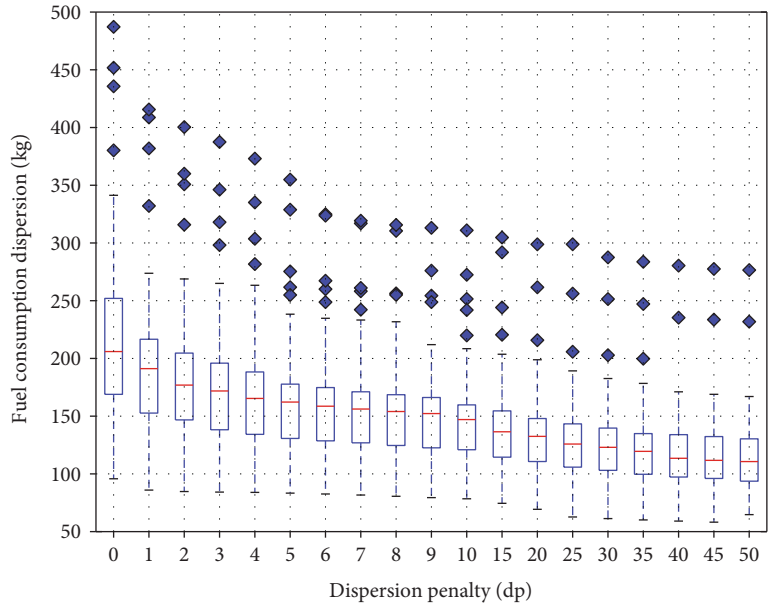

(b) Fuel consumption dispersion (max-min value)

Figure 9: Aggregated dispersion boxplots for the single origin-destination case study.

day and different dp values ranging 0 to 50. Furthermore, the realization computed using reanalysis is represented (as a star). It can be seen that flight time dispersions and fuel burnt consumptions systematically reduce as dp increases. Similarly, expected flight times and fuel burns increase. It is also interesting to remark that $\Delta\mathrm{FT}^{\mathrm{Mean}}$ and $\Delta\mathrm{FC}^{\mathrm{Mean}}$ decrease as dp increases; in other words, the predicted values get closer to the realization. Indeed, it is remarkable that the greater the dp value is, the more likely the realization to fit within the predicted bounds.

Quantitative information is presented in Table 1 (row 1). For the sake of illustration, it can be observed that maximum dispersions $\mathbb{R}(\mathrm{FT})^{\mathrm{R-Trj}}$ can reach up to roughly 337 sec. This dispersion could be reduced to 207 sec. (130 sec. or 38% reduction) by setting dp = 20. This would come at a cost of roughly 381 sec. of extra flight time in average $\bar{\mathrm{FT}}^{\mathrm{R-Trj}}$. Similarly, in terms of consumption, dispersion can be reduced from 487 kg to 298 kg (189 kg or 38%), all in all with a cost of roughly 550 kg of extra fuel burnt. The Pareto frontier of the problem weighting dispersion and time/consumption is presented in Figure 8. The reader is referred therein and to Table 1 for a quantitative insight on other intermediate trade-offs and additional days.

Moreover, the deviations of the expected time (as predicted) with respect to the realization $\Delta\mathrm{FT}^{\mathrm{Mean}}$ is decreasing as dp increases, from 132 sec. to 84 sec. (negative sign means

the trajectory flown under reanalysis has greater flight time than under the EPS forecast), i.e, roughly 48.2 sec. or, in other words, predicted trajectories with dp = 20 are 47.6% more predictable. Similarly with fuel consumption ΔFC^{Mean}, we reduce the deviations with respect to the expected consumption from 191 kg to 121 kg, i.e., 70 kg of reduction.

Last but not the least, it holds (as expected) that the higher dp, the greater the percentage of prediction fitting within the realization ± tolerances $\%x^{Rea\pm Tol}$. On the contrary, it should be noted that the realization is not fitting within the predicted interquartile range $\mathbb{B}(FT)^{IQR}$ (the same reasoning holds *mutatis mutandis* for FC), neither within the expected flight time ± 30 sec. range $\mathbb{B}(FT)^{Exp\pm Tol}$. Notice however that the realization hits closer to the IQR as dp grows (see Figure 7). This is partially due to the high uncertainty. In other words, we are able to substantially improve predictability; however, the predictability is still rather poor. The reader is referred to Section 6.3 for a discussion on accuracy of realizations (as considered herein).

6.1.2. 2016 Aggregated Results. Figure 9 shows aggregated values for dispersion and for all 72 days considered. Table 2 presents all aggregated KPIs. On average, flight time dispersion can be reduced roughly 1 min (from 151 sec. to 92 sec.) by computing flight plans with dp equal to 20. Similarly, fuel consumption dispersion could be reduced roughly 85 kg (from 219 to 133 kg). This represents 39% dispersion reduction in both times and fuel consumption. This nevertheless would come at an average cost of extra 300 sec. and 450 kg of fuel.

As for the indicators that take into consideration the realizations, we can observe that deviations from the expected times and fuels decrease slightly (from 29.5 to 27.3 sec. and 42.7 to 39.4 kg, respectively). It is however remarkable to look at the percentage of times the realization is within the IQR (around 40%), yet also at the percentage of time flights are within the expected value ± a given tolerance (30 sec. and 70 kg in this case), over 60% and almost 90% for times and consumptions, respectively. Again, readers are referred to Section 6.3 for a discussion on accuracy of realizations (as considered herein).

6.2. Multiple O-D Flights, Multiple Steps, Single Day. We keep the focus on the same day "2016-Oct-05." We choose now a set of 164 flights flying to different destinations (according to British Airways' schedule for that day). Figure 10 provides a snapshot of the flight set. We assume all of them fly at constant barometric altitude FL380 and constant Mach M0.82. A free routing airspace is also assumed. Different aircraft types are considered, all modeled as BADA3, and considering their corresponding reference masses as initial mass. As for wind, we take EPS forecasts produced on 2016-Oct-05 at 00.00 with forecast steps ranging from 00 to 48 hours.

For the sake of representativeness, we have clustered them into 64 short-, 46 medium-, and 54 long-haul flights. We present the top three long-haul flights in Table 3. Top three medium- and short-haul flights can be seen in Table 4 and Table 5, respectively. All in all, results show a consistent behaviour; dispersions are systematically reduced as we increase dp values; yet, they increase as we increase the forecast step. Needless to say, this corresponds to the expected behaviour. We discuss in what follows flight EGLL to SBGL (first row in Table 3).

Table 2: Aggregated KPIs. Tol = 30 sec. (FT) and 70 kg (FC).

Variable	dp0	dp5	dp10	dp15	dp20
$\overline{\mathbb{R}(FT)}$	151.6	113.3	102.6	96.7	92.6
$\overline{\mathbb{R}(FC)}$	219.4	163.9	148.4	139.7	133.7
$\overline{\Delta FT}^{Mean}$	29.5	25.8	26.3	27.4	27.3
$\overline{\Delta FC}^{Mean}$	42.7	37.3	38.0	39.6	39.4
$\overline{\overline{FT}}^{R-Trj}$	19918.2	19980.9	20061.5	20136.1	20218.2
$\overline{\overline{FC}}^{R-Trj}$	30298.6	30389.2	30505.7	30613.5	30732.0
$\%\mathbb{B}(FT)^{IQR}$	38.9	45.8	44.4	38.9	40.3
$\%\mathbb{B}(FC)^{IQR}$	38.9	45.8	44.4	38.9	40.3
$\%\mathbb{B}(FT)^{Exp\pm Tol}$	58.3	65.3	66.7	63.9	62.5
$\%\mathbb{B}(FC)^{Exp\pm Tol}$	87.5	93.1	87.5	88.9	87.5
$\%FT^{Rea\pm Tol}$	47.6	52.2	52.8	51.9	52.6
$\%FC^{Rea\pm Tol}$	69.1	73.8	74.7	74.2	74.9

6.2.1. Representative Flight EGLL to SBGL. First, it is interesting to look at how dispersions grow as prediction horizon (or step) does. Indeed, at one day look-ahead time, they can be more than 10 minutes; yet, at two days look-ahead time, they can go up 20 minutes. Second, it is also very important to observe how we are able to substantially reduce flight time uncertainty as we increase the dp parameter. For instance, at one day prediction step, we are able to cut it by almost two (459 to 249 sec., i.e., 46% reduction) by moving from dp = 0 to dp = 10. All in all, this could be of course very relevant for the ATFM units at pretactical level, where they do the capacity-demand balancing the day before operation. Nonetheless, this increase of predictability would come at the cost of increasing flight time and fuel consumption (roughly 800 sec. or 1000 kg in this case). Other trade-off values (also for the other top 2 flights) can be checked both in Table 3 and Figure 11, where the Pareto frontiers of the problem are shown for this specific flight. Moreover, Figure 12 shows boxplot information, including the obtained realization. It can be seen that dispersions reduce as dp increases. On the contrary, expected flight times and fuel burns increase. It is also interesting to remark that in general, ΔFT^{Mean} and ΔFC^{Mean} decrease as dp increases; in other words, the predicted values get closer to the realization. Nonetheless, no conclusive results can be extracted in this sense as forecast step increases. Similar analysis holds for other flights. Of course, medium- and short-haul flights present lower dispersion values. Detailed information on them can be checked in Tables 3, 6–9.

6.2.2. Aggregated Results. An aggregated analysis (for all 164 flights considered) is presented in both Table 5 and

Figure 10: Optimal Trjs dp equal to 0 and weather forecast step equal to 0 (05/10/2016 multiple routes).

Figure 13. Also, Figures 13–16 show aggregated values considered as per haul. One can readily observe that fuel and time dispersions are systematically reduced as we increase dp values; yet, they increase as we increase the forecast step. Aggregated results in Table 5 show, e.g., for one day planning horizon, roughly 75 sec. of time dispersion reduction with an associated cost of roughly 400 sec. of flight time (580 kg of extra fuel). If one looks at forecast step 48, one would get 133 sec. of reduction in time dispersion with a flight time cost of 664 sec. (almost 1000 kg). As for the indicator associated with the realization, we can see that the realizations are typically close to the expected values, meaning that we would be quite predictable in aggregated terms.

6.3. Discussion on the realization. So far, we have observed a systematic consistency in the behaviour of the robust trajectory planning: predicted dispersions are reduced as dp grows, yet at the cost of flying longer. This is however not the case when computing the flight as with the realizations of wind based on reanalysis. This is in principle expected, since we do not know a priori what the wind would be. Nonetheless, we have observed some features that indicate further research is needed.

(i) First, one should expect the realization to be within the EPS. However, this is not always the case. We have indeed found strong deviations, which are in general very dependant of the geographic coordinates. This is due to EPS usually presenting spread-error correlation, tending to be biased and underdispersed. Indeed, different techniques for the statistical postprocessing and calibration of EPS are around, e.g., based on ensemble model output statistics and Bayesian model averaging. Thus, research efforts in improving the quality of the EPS (at the barometric levels) are needed

(ii) Reanalysis is not realized wind; it is just an assimilation. Aircraft-derived data should be used instead (AMDAR data). Nevertheless, these date are not uniform (they populate the network of airways), bringing in associated drawbacks (e.g., the need of estimation outside this network). Thus, using AMDAR data would lead to similar problems as using reanalysis. Initiatives such as the recent launch of Eolus by ESA, aiming at providing a worldwide gridded measurement of winds at different altitudes, will be paramount in the future

7. Conclusions

This study explored the characterization and enhancement of flight planning predictability under wind uncertainty. For these purposes two analyses (single and multiple origin-destination; single and multiple step prediction horizon) were carried out.

Table 3: Top three long-haul flights in terms of flight time dispersion. Tol = 30 sec.

Variable	Airp. Orig-Dest	Step 0			Step 12			Step 24			Step 36			Step 48		
		dp0	dp10	dp20	dp0	dp10	dp20	dp0	dp10	dp20	dp0	dp10	dp20	dp0	dp10	dp20
$\mathbb{R}(\mathrm{FT})^{\mathrm{R-Trj}}$	EGLL-SBGL	253.3	142.6	122.0	358.3	237.2	219.4	459.2	249.8	213.9	495.5	388.8	340.8	1126.4	492.8	465.2
$\overline{\mathrm{FT}}^{\mathrm{R-Trj}}$	EGLL-SBGL	38013.3	38370.5	38766.7	37873.9	38205.9	38517.7	37997.2	38689.3	39371.4	38419.6	38958.8	39787.6	39329.7	39810.0	40357.3
$\mathrm{FT}^{\mathrm{Rea}}$	EGLL-SBGL	38093.9	38470.9	38854.3	37809.4	38170.0	38469.1	37780.1	38474.2	39158.0	38289.4	38804.2	39644.4	39122.9	39776.1	40306.1
$\Delta\mathrm{FT}^{\mathrm{Mean}}$	EGLL-SBGL	-80.6	-100.4	-87.6	64.5	35.9	48.6	217.1	215.1	213.3	130.2	154.6	143.2	206.9	33.9	51.3
$\mathbb{B}(\mathrm{FT})^{\mathrm{IQR}}$	EGLL-SBGL	False	False	False	True	True	True	False	False	False	False	False	False	False	True	True
$\mathbb{B}(\mathrm{FT})^{\mathrm{Exp\pm Tol}}$	EGLL-SBGL	False	False	False	False	False	False	False	False	False	False	False	False	False	False	False
$\%\mathrm{FT}^{\mathrm{Rea\pm Tol}}$	EGLL-SBGL	12.0	2.0	4.0	26.0	24.0	26.0	6.0	0.0	0.0	8.0	4.0	10.0	6.0	8.0	8.0
$\mathbb{R}(\mathrm{FT})^{\mathrm{R-Trj}}$	TAPA-EGKK	211.6	84.3	78.9	451.0	219.2	212.3	537.0	332.7	328.3	765.1	429.4	389.6	1112.7	567.9	459.9
$\overline{\mathrm{FT}}^{\mathrm{R-Trj}}$	TAPA-EGKK	25561.4	25752.3	25934.8	25786.3	26191.7	26480.6	26385.1	27416.1	27954.4	26873.5	27678.2	28396.5	26496.8	27666.7	29487.5
$\mathrm{FT}^{\mathrm{Rea}}$	TAPA-EGKK	25450.9	25647.3	25834.2	25792.5	26189.1	26469.5	26411.1	27464.6	27973.4	26961.0	27707.6	28401.7	26612.5	27552.8	29427.6
$\Delta\mathrm{FT}^{\mathrm{Mean}}$	TAPA-EGKK	110.5	105.0	100.7	-6.2	2.6	11.0	-26.0	-48.5	-19.0	-87.4	-29.4	-5.1	-115.7	113.9	59.9
$\mathbb{B}(\mathrm{FT})^{\mathrm{IQR}}$	TAPA-EGKK	False	False	False	True	True	True	True	True	True	True	True	True	False	False	True
$\mathbb{B}(\mathrm{FT})^{\mathrm{Exp\pm Tol}}$	TAPA-EGKK	False	False	False	True	True	True	True	False	True	False	True	True	False	False	False
$\%\mathrm{FT}^{\mathrm{Rea\pm Tol}}$	TAPA-EGKK	2.0	0.0	0.0	24.0	36.0	34.0	24.0	18.0	18.0	20.0	8.0	6.0	2.0	14.0	12.0
$\mathbb{R}(\mathrm{FT})^{\mathrm{R-Trj}}$	EGKK-MMUN	254.4	76.9	70.5	370.3	246.9	220.0	639.8	321.0	273.3	899.3	460.4	436.5	971.6	574.9	545.2
$\overline{\mathrm{FT}}^{\mathrm{R-Trj}}$	EGKK-MMUN	35990.1	36365.6	36598.8	34405.0	34821.4	35212.8	34633.1	36014.6	36426.2	35048.7	36491.1	37286.9	35639.6	36281.0	37070.0
$\mathrm{FT}^{\mathrm{Rea}}$	EGKK-MMUN	36124.7	36428.3	36662.4	34309.6	34768.9	35146.8	34691.2	36117.0	36612.5	35033.4	36511.5	37317.4	35718.1	36458.5	37230.3
$\Delta\mathrm{FT}^{\mathrm{Mean}}$	EGKK-MMUN	-134.5	-62.7	-63.6	95.5	52.5	66.0	-58.1	-102.4	-186.2	15.3	-20.4	-30.5	-78.5	-177.6	-160.3
$\mathbb{B}(\mathrm{FT})^{\mathrm{IQR}}$	EGKK-MMUN	False	False	False	False	False	False	True	False	False	True	True	True	True	False	False
$\mathbb{B}(\mathrm{FT})^{\mathrm{Exp\pm Tol}}$	EGKK-MMUN	False	False	False	False	False	False	False	False	False	True	True	False	False	False	False
$\%\mathrm{FT}^{\mathrm{Rea\pm Tol}}$	EGKK-MMUN	6.0	16.0	4.0	20.0	32.0	20.0	16.0	10.0	0.0	4.0	10.0	12.0	16.0	8.0	8.0

Table 4: Top three medium-haul flights in terms of flight time dispersion. Tol = 30 sec.

Variable	Airp. Orig-Dest	Step 0			Step 12			Step 24			Step 36			Step 48		
		dp0	dp10	dp20	dp0	dp10	dp20	dp0	dp10	dp20	dp0	dp10	dp20	dp0	dp10	dp20
$\mathbb{R}(\mathrm{FT})^{\mathrm{R-Trj}}$	EGLL-KSAN	71.3	35.7	33.4	156.3	118.6	86.8	181.0	126.6	121.7	537.8	349.2	249.8	896.0	331.9	256.7
$\overline{\mathrm{FT}}^{\mathrm{R-Trj}}$	EGLL-KSAN	9758.4	9881.2	9911.8	9594.4	9746.3	9958.0	9882.8	10006.9	10090.9	10284.7	11149.2	12503.2	10959.2	11772.1	12744.0
$\mathrm{FT}^{\mathrm{Rea}}$	EGLL-KSAN	9753.3	9896.4	9926.9	9574.7	9725.5	9940.2	9842.9	9967.6	10054.3	10235.0	11078.0	12461.5	10932.5	11958.0	12917.7
$\Delta\mathrm{FT}^{\mathrm{Mean}}$	EGLL-KSAN	5.1	-15.2	-15.1	19.7	20.8	17.8	39.8	39.3	36.6	49.7	71.1	41.7	26.7	-185.9	-173.6
$\mathbb{B}(\mathrm{FT})^{\mathrm{IQR}}$	EGLL-KSAN	True	False	False	True	True	False	False	False	False	True	False	True	True	False	False
$\mathbb{B}(\mathrm{FT})^{\mathrm{Exp\pm Tol}}$	EGLL-KSAN	True	True	True	True	True	True	False	False	False	False	False	False	True	False	False
$\%\mathrm{FT}^{\mathrm{Rea\pm Tol}}$	EGLL-KSAN	96.0	90.0	88.0	52.0	64.0	66.0	38.0	48.0	48.0	20.0	22.0	34.0	6.0	0.0	0.0
$\mathbb{R}(\mathrm{FT})^{\mathrm{R-Trj}}$	EGKK-LPMA	70.9	35.6	34.0	150.2	130.5	109.5	169.6	120.2	117.3	508.8	334.2	212.7	867.3	337.2	267.7
$\overline{\mathrm{FT}}^{\mathrm{R-Trj}}$	EGKK-LPMA	9721.7	9822.8	9845.3	9504.8	9558.5	9833.1	9740.0	9883.2	9936.2	10122.9	10897.7	11698.1	10772.7	11758.9	12555.2
$\mathrm{FT}^{\mathrm{Rea}}$	EGKK-LPMA	9722.8	9841.3	9863.4	9484.7	9536.2	9806.3	9698.2	9841.7	9896.1	10063.8	10831.1	11690.9	10723.3	11947.4	12734.8
$\Delta\mathrm{FT}^{\mathrm{Mean}}$	EGKK-LPMA	-1.1	-18.5	-18.1	20.1	22.2	26.7	41.8	41.5	40.1	59.1	66.6	7.2	49.5	-188.5	-179.6
$\mathbb{B}(\mathrm{FT})^{\mathrm{IQR}}$	EGKK-LPMA	True	False	False	True	True	False	False	False	False	True	False	True	True	False	False
$\mathbb{B}(\mathrm{FT})^{\mathrm{Exp\pm Tol}}$	EGKK-LPMA	True	True	True	True	True	True	False	False	False	False	False	True	False	False	False
$\%\mathrm{FT}^{\mathrm{Rea\pm Tol}}$	EGKK-LPMA	96.0	78.0	82.0	52.0	54.0	52.0	36.0	42.0	42.0	20.0	22.0	32.0	8.0	0.0	0.0
$\mathbb{R}(\mathrm{FT})^{\mathrm{R-Trj}}$	EGLL-KSJC	65.8	46.7	35.5	143.3	132.2	128.3	286.0	224.1	205.9	555.8	360.3	262.4	610.9	234.5	232.2
$\overline{\mathrm{FT}}^{\mathrm{R-Trj}}$	EGLL-KSJC	9084.1	9173.2	9349.9	9402.7	9446.7	9519.9	9879.4	10090.3	10354.7	10365.6	10443.8	11113.9	9842.0	10702.4	10810.3
$\mathrm{FT}^{\mathrm{Rea}}$	EGLL-KSJC	9045.3	9127.0	9301.8	9377.9	9423.4	9496.8	9871.3	10095.7	10356.0	10235.9	10298.1	10985.4	9901.9	10725.1	10828.5
$\Delta\mathrm{FT}^{\mathrm{Mean}}$	EGLL-KSJC	38.9	46.2	48.1	24.8	23.3	23.1	8.1	-5.4	-1.3	129.7	145.7	128.5	-59.9	-22.7	-18.2
$\mathbb{B}(\mathrm{FT})^{\mathrm{IQR}}$	EGLL-KSJC	False	False	False	False	False	False	True	True	True	False	False	False	False	True	True
$\mathbb{B}(\mathrm{FT})^{\mathrm{Exp\pm Tol}}$	EGLL-KSJC	False	False	False	True	True	True	True	True	True	False	False	False	False	True	True
$\%\mathrm{FT}^{\mathrm{Rea\pm Tol}}$	EGLL-KSJC	24.0	16.0	0.0	56.0	58.0	60.0	38.0	36.0	40.0	14.0	12.0	20.0	14.0	24.0	22.0

Table 5: Top three short-haul flights in terms of flight time dispersion. Tol = 30 sec.

Variable	Airp. Orig-Dest	Step 0			Step 12			Step 24			Step 36			Step 48		
		dp0	dp10	dp20	dp0	dp10	dp20	dp0	dp10	dp20	dp0	dp10	dp20	dp0	dp10	dp20
$\mathbb{R}(\mathrm{FT})^{\mathrm{R-Trj}}$	EGKK-LPPR	39.2	36.8	36.1	95.8	86.2	83.2	151.2	84.3	75.1	309.3	291.6	134.3	493.8	272.3	244.8
$\overline{\mathrm{FT}}^{\mathrm{R-Trj}}$	EGKK-LPPR	5409.5	5415.3	5425.8	5097.5	5139.4	5186.8	5049.8	5280.3	5405.8	5171.1	5227.0	7044.2	5571.7	6514.7	6882.0
$\mathrm{FT}^{\mathrm{Rea}}$	EGKK-LPPR	5409.4	5414.9	5425.5	5085.2	5128.9	5176.8	5044.7	5270.2	5395.4	5130.7	5183.4	7021.9	5564.1	6617.9	6980.3
$\Delta\mathrm{FT}^{\mathrm{Mean}}$	EGKK-LPPR	0.1	0.4	0.4	12.3	10.5	10.0	5.0	10.1	10.4	40.4	43.6	22.3	7.5	-103.2	-98.2
$\mathbb{B}(\mathrm{FT})^{\mathrm{IQR}}$	EGKK-LPPR	True	True	True	True	True	True	True	False	False	True	False	True	True	False	False
$\mathbb{B}(\mathrm{FT})^{\mathrm{Exp\pm Tol}}$	EGKK-LPPR	True	True	True	True	True	True	True	True	True	False	False	True	True	False	False
$\%\mathrm{FT}^{\mathrm{Rea\pm Tol}}$	EGKK-LPPR	100.0	100.0	100.0	72.0	78.0	80.0	76.0	86.0	88.0	30.0	30.0	44.0	22.0	20.0	18.0
$\mathbb{R}(\mathrm{FT})^{\mathrm{R-Trj}}$	EGLL-KDEN	31.8	30.5	29.4	120.0	94.0	84.4	118.0	84.7	80.4	254.0	120.7	116.2	451.1	371.1	346.6
$\overline{\mathrm{FT}}^{\mathrm{R-Trj}}$	EGLL-KDEN	5703.1	5709.9	5727.2	5450.9	5622.9	5746.9	5153.0	5284.7	5347.3	5194.3	5887.1	5951.4	5490.1	5742.3	6093.2
$\mathrm{FT}^{\mathrm{Rea}}$	EGLL-KDEN	5689.1	5697.5	5716.4	5437.7	5603.3	5727.4	5141.8	5272.5	5334.0	5140.9	5865.5	5931.2	5401.5	5628.3	5988.2
$\Delta\mathrm{FT}^{\mathrm{Mean}}$	EGLL-KDEN	14.0	12.3	10.8	13.2	19.5	19.5	11.2	12.1	13.3	53.4	21.6	20.2	88.6	114.0	105.0
$\mathbb{B}(\mathrm{FT})^{\mathrm{IQR}}$	EGLL-KDEN	False	False	False	True	False	False	True	False	False	False	True	True	True	False	False
$\mathbb{B}(\mathrm{FT})^{\mathrm{Exp\pm Tol}}$	EGLL-KDEN	True	True	True	True	True	True	True	True	True	False	True	True	False	False	False
$\%\mathrm{FT}^{\mathrm{Rea\pm Tol}}$	EGLL-KDEN	100.0	100.0	100.0	76.0	72.0	74.0	84.0	84.0	84.0	32.0	56.0	58.0	12.0	18.0	18.0
$\mathbb{R}(\mathrm{FT})^{\mathrm{R-Trj}}$	EGLL-LEMD	31.1	29.9	29.3	105.0	69.8	67.8	115.1	85.4	80.8	221.5	108.4	106.4	402.4	344.8	316.3
$\overline{\mathrm{FT}}^{\mathrm{R-Trj}}$	EGLL-LEMD	5329.8	5334.9	5345.3	5153.9	5261.4	5290.6	4826.6	4902.1	4969.3	4828.0	5359.0	5389.2	5078.5	5268.6	5685.1
$\mathrm{FT}^{\mathrm{Rea}}$	EGLL-LEMD	5312.5	5319.4	5329.4	5142.1	5257.0	5285.5	4823.3	4898.2	4964.1	4784.7	5339.1	5369.7	4982.3	5157.5	5582.8
$\Delta\mathrm{FT}^{\mathrm{Mean}}$	EGLL-LEMD	17.3	15.5	15.9	11.8	4.4	5.2	3.3	3.9	5.1	43.3	19.9	19.5	96.2	111.1	102.3
$\mathbb{B}(\mathrm{FT})^{\mathrm{IQR}}$	EGLL-LEMD	False	False	False	True	True	True	True	True	True	False	True	True	False	False	False
$\mathbb{B}(\mathrm{FT})^{\mathrm{Exp\pm Tol}}$	EGLL-LEMD	True	True	True	True	True	True	True	True	True	False	True	True	False	False	False
$\%\mathrm{FT}^{\mathrm{Rea\pm Tol}}$	EGLL-LEMD	92.0	96.0	94.0	78.0	94.0	94.0	90.0	90.0	90.0	40.0	66.0	66.0	16.0	18.0	18.0

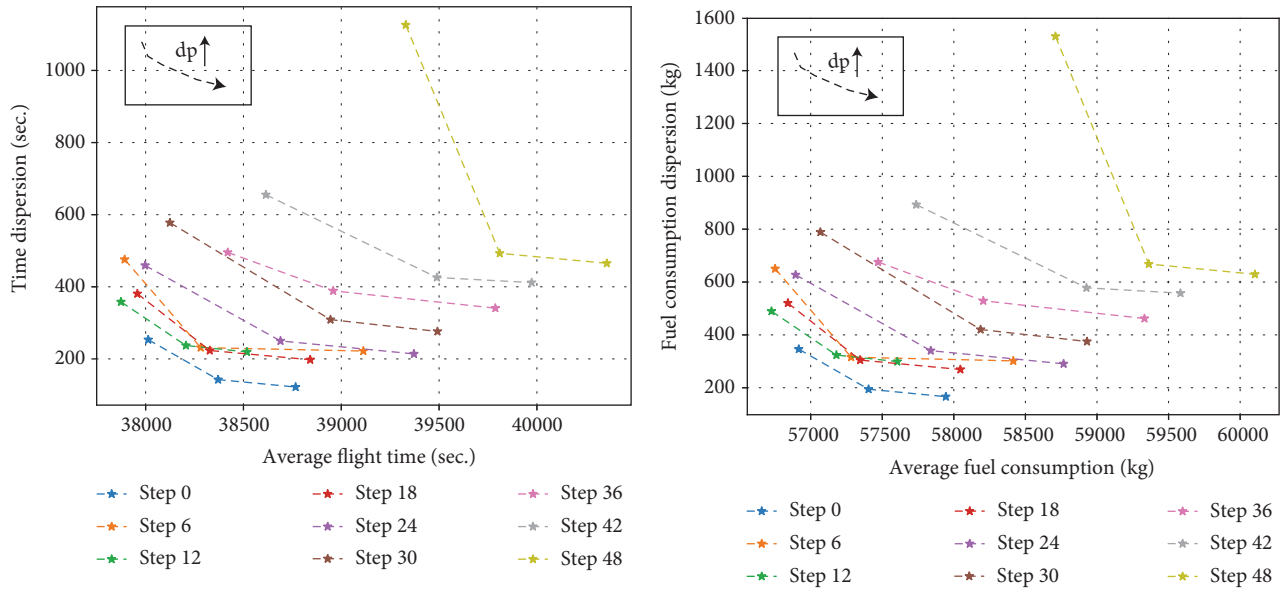

(a) Pareto front time dispersion vs. average flight time

(b) Pareto front fuel dispersion vs. average fuel consumption

Figure 11: EGLL to SBGL results trade-off solutions of the problem: dispersion vs. dp values; and flight times/fuel consumption vs. dispersion.

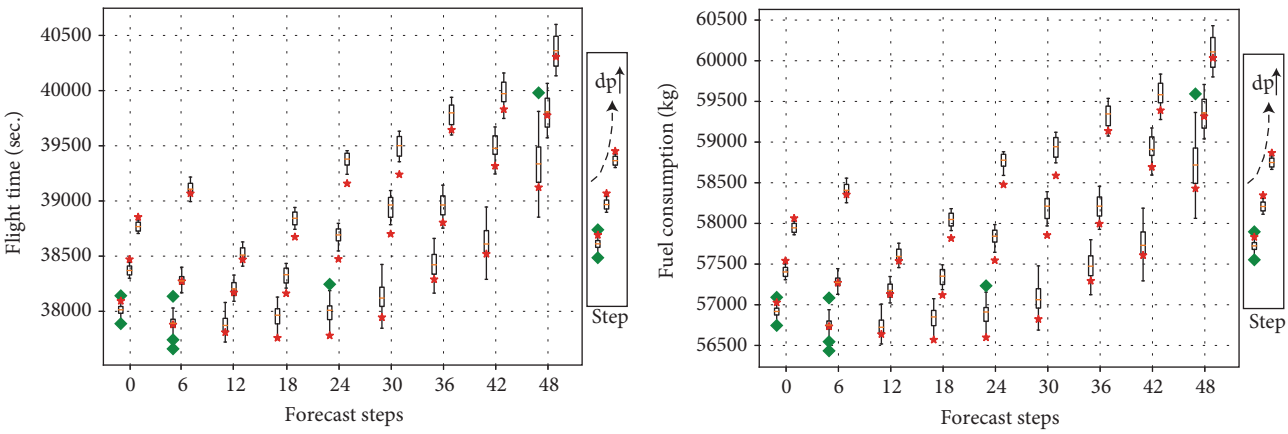

(a) Flight times (spline)

(b) Fuel consumptions (spline)

Figure 12: EGLL to SBGL results. Boxplots denote predicted uncertainties (based on EPS data and computed using the robust flight planning algorithm); red stars denote realized values (based on reanalysis data).

The single origin-destination flight (KJFK-LPPT), over a set of days along year 2016, was computed considering a forecast step used that represents the characteristic flight dispatching level. In average, the cost of increasing 1 sec. of predictability is 5 seconds of extra flight time. Also in average, the cost of reducing fuel burnt uncertainty 1 kg is 5 kg of extra fuel burnt. For some extreme days, increasing 1 sec. predictability (reducing also fuel burnt uncertainty by 1 kg) would cost 2.5 sec. (2.5 kg) of extra fuel burnt. This improvement in flight predictability has some direct relationship with airline savings via fuel reserves, yet also has important indirect effects such as less ATC tactical intervention, less delays, and thus potential miss connections. Further studies on quantifying both these direct and indirect effects should be addressed. As for the multiple origin-destination analysis, we covered a global study considering 164 flights with different origin-destinations. The forecast step used (up to two days) represents the characteristic air traffic flow management pretactical and tactical time horizons. Similarly, for 1 to 2 days forecast steps, the cost of increasing 1 sec. of predictability is between 5 and 5.5 seconds of extra flight time (also, 5 to 5.5 kg of extra fuel burnt for reducing 1 kg of fuel burnt uncertainty). Yet, we can observe that the higher the forecasting step, the higher the uncertainty: uncertainty grows between 50 and 70 secs. in flight times every 12 hours when considering minimum time trajectories. We are

Table 6: Top three long-haul flights in terms of fuel consumption dispersion. Tol = 70 kg.

Variable	Airp. Orig-Dest	Step 0			Step 12			Step 24			Step 36			Step 48		
		dp0	dp10	dp20	dp0	dp10	dp20	dp0	dp10	dp20	dp0	dp10	dp20	dp0	dp10	dp20
$\mathbb{R}(\mathrm{FC})^{\mathrm{R-Trj}}$	EGLL-SBGL	346.1	194.5	166.2	489.7	323.8	299.1	627.4	340.4	290.6	675.8	529.0	462.1	1529.8	668.2	629.4
$\overline{\mathrm{FC}}^{\mathrm{R-Trj}}$	EGLL-SBGL	56916.7	57404.2	57944.3	56726.1	57179.7	57605.0	56894.6	57838.8	58766.7	57471.2	58205.8	59331.6	58710.0	59361.9	60103.3
$\mathrm{FC}^{\mathrm{Rea}}$	EGLL-SBGL	57026.8	57541.2	58063.5	56638.0	57130.7	57538.8	56597.9	57545.7	58476.8	57293.6	57995.4	59137.4	58429.0	59316.0	60034.0
$\Delta\mathrm{FC}^{\mathrm{Mean}}$	EGLL-SBGL	-110.1	-137.0	-119.3	88.2	49.1	66.2	296.8	293.1	289.9	177.6	210.4	194.3	281.0	46.0	69.3
$\mathbb{B}(\mathrm{FC})^{\mathrm{IQR}}$	EGLL-SBGL	False	False	False	True	True	True	False	False	False	False	False	False	False	True	True
$\mathbb{B}(\mathrm{FC})^{\mathrm{Exp\pm Tol}}$	EGLL-SBGL	False	False	False	False	True	True	False	False	False	False	False	False	False	True	True
$\%\mathrm{FC}^{\mathrm{Rea\pm Tol}}$	EGLL-SBGL	28.0	22.0	30.0	36.0	44.0	46.0	8.0	0.0	0.0	18.0	22.0	26.0	14.0	22.0	14.0
$\mathbb{R}(\mathrm{FC})^{\mathrm{R-Trj}}$	TAPA-EGKK	305.7	121.7	113.7	650.8	315.7	305.3	772.6	476.4	468.9	1098.5	614.2	555.3	1600.1	812.4	652.5
$\overline{\mathrm{FC}}^{\mathrm{R-Trj}}$	TAPA-EGKK	39430.5	39706.2	39969.5	39755.2	40339.7	40755.5	40618.1	42098.0	42868.0	41320.1	42473.1	43498.9	40778.7	42456.7	45050.3
$\mathrm{FC}^{\mathrm{Rea}}$	TAPA-EGKK	39271.0	39554.6	39824.3	39764.2	40336.0	40739.6	40655.6	42167.5	42895.1	41445.6	42515.3	43506.3	40945.2	42293.8	44965.3
$\Delta\mathrm{FC}^{\mathrm{Mean}}$	TAPA-EGKK	159.6	151.6	145.2	-9.0	3.7	15.9	-37.4	-69.5	-27.1	-125.6	-42.2	-7.4	-166.5	162.9	85.0
$\mathbb{B}(\mathrm{FC})^{\mathrm{IQR}}$	TAPA-EGKK	False	False	False	True	True	True	True	True	True	True	True	True	False	False	True
$\mathbb{B}(\mathrm{FC})^{\mathrm{Exp\pm Tol}}$	TAPA-EGKK	False	False	False	True	True	True	True	True	True	False	True	True	False	False	False
$\%\mathrm{FC}^{\mathrm{Rea\pm Tol}}$	TAPA-EGKK	2.0	0.0	0.0	32.0	50.0	54.0	30.0	30.0	22.0	26.0	20.0	16.0	4.0	18.0	14.0
$\mathbb{R}(\mathrm{FC})^{\mathrm{R-Trj}}$	EGKK-MMUN	350.6	105.8	96.9	513.8	342.0	304.3	886.6	442.3	375.9	1244.3	633.0	598.1	1340.9	791.2	747.7
$\overline{\mathrm{FC}}^{\mathrm{R-Trj}}$	EGKK-MMUN	54140.7	54657.7	54978.4	51948.7	52525.9	53067.6	52265.0	54174.3	54741.1	52840.5	54830.2	55922.6	53657.0	54541.1	55625.3
$\mathrm{FC}^{\mathrm{Rea}}$	EGKK-MMUN	54326.0	54743.9	55065.8	51816.3	52453.2	52976.4	52345.5	54315.5	54997.1	52819.5	54858.3	55964.5	53765.5	54785.5	55845.1
$\Delta\mathrm{FC}^{\mathrm{Mean}}$	EGKK-MMUN	-185.4	-86.2	-87.4	132.4	72.7	91.2	-80.6	-141.1	-256.0	21.0	-28.1	-41.8	-108.5	-244.4	-219.8
$\mathbb{B}(\mathrm{FC})^{\mathrm{IQR}}$	EGKK-MMUN	False	False	False	False	False	False	True	False	False	True	True	True	True	False	False
$\mathbb{B}(\mathrm{FC})^{\mathrm{Exp\pm Tol}}$	EGKK-MMUN	False	False	False	False	False	False	False	False	False	True	True	True	False	False	False
$\%\mathrm{FC}^{\mathrm{Rea\pm Tol}}$	EGKK-MMUN	10.0	32.0	36.0	32.0	42.0	42.0	26.0	24.0	0.0	14.0	18.0	22.0	20.0	14.0	12.0

Table 7: Aggregated KPI multiple origin-destination. Tol = 30 sec. (FT) and 70 kg (FC).

Variable	Step 0			Step 12			Step 24			Step 36			Step 48		
	dp0	dp10	dp20	dp0	dp10	dp20	dp0	dp10	dp20	dp0	dp10	dp20	dp0	dp10	dp20
$\overline{\mathbb{R}(\mathrm{FT})}$	90.2	53.9	49.1	137.2	99.7	90.8	198.9	135.4	122.6	274.8	187.1	162.3	344.1	232.5	211.2
$\overline{\mathbb{R}(\mathrm{FC})}$	130.0	77.2	70.2	198.9	143.1	129.9	284.9	192.9	174.8	396.3	269.9	234.5	480.2	321.3	288.2
$\overline{\Delta \mathrm{FC}}^{\mathrm{Mean}}$	23.6	24.1	23.1	17.5	19.0	19.4	21.1	22.2	21.9	39.8	39.1	40.1	56.4	50.3	49.9
$\overline{\Delta \mathrm{FC}}^{\mathrm{Mean}}$	33.3	34.1	32.8	24.1	26.8	27.3	30.4	32.6	31.8	56.3	55.2	57.1	79.1	68.2	69.4
$\overline{\overline{\mathrm{FT}}}^{\mathrm{R-Trj}}$	13296.2	13394.3	13477.5	12762.9	12891.1	13032.8	12779.8	13007.1	13192.0	12618.0	12918.4	13246.0	11654.9	12021.9	12319.4
$\overline{\overline{\mathrm{FC}}}^{\mathrm{R-Trj}}$	20564.1	20706.8	20827.7	19699.5	19888.6	20094.8	19643.2	19971.6	20232.1	19537.2	19972.1	20433.9	17678.7	18188.0	18639.7
$\%\mathbb{B}(\mathrm{FT})^{\mathrm{IQR}}$	23.8	25.6	25.6	61.2	56.2	53.1	70.6	60.0	63.8	54.5	42.3	39.7	64.6	51.4	48.6
$\%\mathbb{B}(\mathrm{FC})^{\mathrm{IQR}}$	23.8	25.6	25.6	61.2	56.2	53.1	70.6	60.0	63.8	54.5	42.3	39.7	64.6	51.4	48.6
$\%\mathbb{B}(\mathrm{FT})^{\mathrm{Exp}\pm\mathrm{Tol}}$	74.4	70.7	72.0	85.6	81.9	83.8	78.8	77.5	78.1	54.5	54.5	55.1	52.1	54.9	54.2
$\%\mathbb{B}(\mathrm{FC})^{\mathrm{Exp}\pm\mathrm{Tol}}$	89.0	86.6	87.8	91.2	88.8	89.4	89.4	90.0	88.8	75.0	74.4	73.7	61.1	65.3	66.7
$\%\mathrm{FT}^{\mathrm{Rea}\pm\mathrm{Tol}}$	69.8	69.3	70.4	68.0	70.7	71.4	58.2	61.7	63.1	41.0	43.6	45.3	37.0	41.6	42.1
$\%\mathrm{FC}^{\mathrm{Rea}\pm\mathrm{Tol}}$	83.4	83.9	85.1	80.7	82.0	83.1	74.8	77.3	78.0	63.3	65.4	67.0	54.8	59.6	60.2

Table 8: Top three medium-haul flights in terms of fuel consumption dispersion. Tol = 70 kg.

Variable	Airp. Orig-Dest	Step 0			Step 12			Step 24			Step 36			Step 48		
		dp0	dp10	dp20	dp0	dp10	dp20	dp0	dp10	dp20	dp0	dp10	dp20	dp0	dp10	dp20
$\mathbb{R}(\mathrm{FC})^{\mathrm{R-Trj}}$	EGLL-KSAN	144.4	72.3	67.6	317.0	240.3	175.6	366.3	256.1	245.9	1085.2	700.3	496.1	1799.1	662.7	509.0
$\overline{\mathrm{FC}}^{\mathrm{R-Trj}}$	EGLL-KSAN	20521.3	20770.0	20831.9	20188.8	20496.8	20925.4	20773.1	21024.3	21194.1	21585.3	23324.6	26026.5	22943.1	24570.9	26504.3
$\mathrm{FC}^{\mathrm{Rea}}$	EGLL-KSAN	20511.0	20800.8	20862.4	20148.9	20454.6	20889.4	20692.4	20944.8	21120.1	21485.1	23181.9	25943.7	22889.8	24941.9	26848.3
$\Delta\mathrm{FC}^{\mathrm{Mean}}$	EGLL-KSAN	10.2	-30.8	-30.5	40.0	42.2	36.0	80.7	79.4	74.0	100.2	142.6	82.8	53.3	-371.0	-344.0
$\mathbb{B}(\mathrm{FC})^{\mathrm{IQR}}$	EGLL-KSAN	True	False	False	True	True	False	False	False	False	True	False	True	True	False	False
$\mathbb{B}(\mathrm{FC})^{\mathrm{Exp\pm Tol}}$	EGLL-KSAN	True	True	True	True	True	True	False	False	False	False	False	False	False	False	False
$\%\mathrm{FC}^{\mathrm{Rea\pm Tol}}$	EGLL-KSAN	96.0	76.0	78.0	42.0	52.0	58.0	32.0	36.0	38.0	20.0	18.0	26.0	6.0	0.0	0.0
$\mathbb{R}(\mathrm{FC})^{\mathrm{R-Trj}}$	EGKK-LPMA	76.9	38.6	36.9	163.0	141.6	118.7	183.9	130.3	127.1	551.4	361.8	230.0	939.0	364.6	289.1
$\overline{\mathrm{FC}}^{\mathrm{R-Trj}}$	EGKK-LPMA	10624.5	10734.2	10758.5	10389.2	10447.5	10745.3	10644.4	10799.6	10857.1	11059.4	11898.7	12764.7	11763.4	12830.4	13690.9
$\mathrm{FC}^{\mathrm{Rea}}$	EGKK-LPMA	10625.7	10754.2	10778.1	10367.4	10423.4	10716.3	10599.0	10754.7	10813.6	10995.4	11826.6	12756.9	11709.8	13034.2	13884.9
$\Delta\mathrm{FC}^{\mathrm{Mean}}$	EGKK-LPMA	-1.2	-20.0	-19.6	21.8	24.1	29.0	45.3	45.0	43.5	64.0	72.1	7.8	53.5	-203.8	-194.0
$\mathbb{B}(\mathrm{FC})^{\mathrm{IQR}}$	EGKK-LPMA	True	False	False	True	True	False	False	False	False	True	False	True	True	False	False
$\mathbb{B}(\mathrm{FC})^{\mathrm{Exp\pm Tol}}$	EGKK-LPMA	True	True	True	True	True	True	True	True	True	False	False	True	False	False	False
$\%\mathrm{FC}^{\mathrm{Rea\pm Tol}}$	EGKK-LPMA	100.0	100.0	100.0	74.0	72.0	72.0	60.0	58.0	60.0	30.0	34.0	50.0	12.0	4.0	0.0
$\mathbb{R}(\mathrm{FC})^{\mathrm{R-Trj}}$	EGLL-KSJC	97.0	68.8	52.3	211.0	194.6	188.7	419.9	328.8	301.6	814.0	527.6	383.0	897.1	342.9	339.5
$\overline{\mathrm{FC}}^{\mathrm{R-Trj}}$	EGLL-KSJC	13700.8	13832.1	14092.4	14170.0	14234.8	14342.5	14870.8	15180.3	15567.9	15583.8	15698.4	16678.0	14815.9	16076.9	16234.6
$\mathrm{FC}^{\mathrm{Rea}}$	EGLL-KSJC	13643.5	13764.1	14021.6	14133.5	14200.5	14308.5	14858.9	15188.2	15569.8	15393.9	15485.0	16490.4	14903.9	16110.0	16261.3
$\Delta\mathrm{FC}^{\mathrm{Mean}}$	EGLL-KSJC	57.3	68.1	70.8	36.5	34.3	34.0	11.8	-7.9	-1.9	189.9	213.4	187.6	-88.0	-33.2	-26.7
$\mathbb{B}(\mathrm{FC})^{\mathrm{IQR}}$	EGLL-KSJC	False	False	False	False	False	False	True	True	True	False	False	False	False	True	True
$\mathbb{B}(\mathrm{FC})^{\mathrm{Exp\pm Tol}}$	EGLL-KSJC	False	False	False	True	True	True	True	True	True	False	False	False	False	True	True
$\%\mathrm{FC}^{\mathrm{Rea\pm Tol}}$	EGLL-KSJC	36.0	18.0	16.0	66.0	64.0	62.0	40.0	44.0	52.0	14.0	12.0	20.0	22.0	26.0	24.0

Table 9: Top three short-haul flights in terms of fuel consumption dispersion. Tol is 30 kg.

Variable	Airp. Orig-Dest	Step 0			Step 12			Step 24			Step 36			Step 48		
		dp0	dp10	dp20	dp0	dp10	dp20	dp0	dp10	dp20	dp0	dp10	dp20	dp0	dp10	dp20
$\mathbb{R}(\mathrm{FC})^{\mathrm{R-Trj}}$	EGKK-LPPR	42.8	40.2	39.4	104.6	94.2	90.9	165.1	92.0	82.0	337.8	318.4	146.3	539.0	296.7	266.6
$\overline{\mathrm{FC}}^{\mathrm{R-Trj}}$	EGKK-LPPR	5932.7	5938.9	5950.5	5592.0	5637.7	5689.5	5539.8	5791.5	5928.6	5672.3	5733.3	7715.0	6109.7	7138.2	7538.4
$\mathrm{FC}^{\mathrm{Rea}}$	EGKK-LPPR	5932.6	5938.5	5950.1	5578.5	5626.2	5678.6	5534.3	5780.5	5917.3	5628.2	5685.8	7690.7	6101.5	7250.7	7645.4
$\Delta\mathrm{FC}^{\mathrm{Mean}}$	EGKK-LPPR	0.1	0.4	0.4	13.4	11.5	10.9	5.5	11.0	11.3	44.1	47.6	24.3	8.2	-112.5	-107.0
$\mathbb{B}(\mathrm{FC})^{\mathrm{IQR}}$	EGKK-LPPR	True	True	True	True	True	True	True	False	False	True	False	True	True	False	False
$\mathbb{B}(\mathrm{FC})^{\mathrm{Exp\pm Tol}}$	EGKK-LPPR	True	True	True	True	True	True	True	True	True	False	False	True	True	False	False
$\%\mathrm{FC}^{\mathrm{Rea\pm Tol}}$	EGKK-LPPR	100.0	100.0	100.0	70.0	70.0	72.0	74.0	86.0	86.0	28.0	26.0	38.0	20.0	16.0	16.0
$\mathbb{R}(\mathrm{FC})^{\mathrm{R-Trj}}$	EGLL-KDEN	66.3	63.8	61.4	251.1	196.4	176.3	247.6	177.5	168.4	532.7	251.7	242.3	943.9	774.9	721.8
$\overline{\mathrm{FC}}^{\mathrm{R-Trj}}$	EGLL-KDEN	12179.2	12193.4	12229.7	11652.1	12011.6	12270.7	11027.8	11303.9	11435.1	11114.5	12563.3	12697.3	11733.9	12261.2	12992.9
$\mathrm{FC}^{\mathrm{Rea}}$	EGLL-KDEN	12150.1	12167.7	12207.1	11624.4	11970.8	12230.0	11004.4	11278.5	11407.3	11002.5	12518.4	12655.2	11548.6	12023.1	12774.2
$\Delta\mathrm{FC}^{\mathrm{Mean}}$	EGLL-KDEN	29.2	25.7	22.6	27.6	40.8	40.7	23.5	25.4	27.9	112.0	45.0	42.1	185.4	238.1	218.7
$\mathbb{B}(\mathrm{FC})^{\mathrm{IQR}}$	EGLL-KDEN	False	False	False	True	False	False	True	False	False	False	True	True	True	False	False
$\mathbb{B}(\mathrm{FC})^{\mathrm{Exp\pm Tol}}$	EGLL-KDEN	True	True	True	True	False	False	True	True	True	False	False	False	False	False	False
$\%\mathrm{FC}^{\mathrm{Rea\pm Tol}}$	EGLL-KDEN	52.0	58.0	62.0	32.0	34.0	36.0	52.0	48.0	48.0	10.0	40.0	38.0	2.0	10.0	8.0
$\mathbb{R}(\mathrm{FC})^{\mathrm{R-Trj}}$	EGLL-LEMD	33.7	32.5	31.8	114.1	75.8	73.6	125.1	92.8	87.8	240.7	117.7	115.5	437.0	374.3	343.2
$\overline{\mathrm{FC}}^{\mathrm{R-Trj}}$	EGLL-LEMD	5810.6	5816.1	5827.4	5619.7	5736.4	5768.1	5264.1	5346.2	5419.1	5265.7	5842.3	5875.1	5537.7	5744.1	6196.3
$\mathrm{FC}^{\mathrm{Rea}}$	EGLL-LEMD	5791.9	5799.3	5810.1	5606.8	5731.6	5762.5	5260.5	5341.9	5413.5	5218.6	5820.7	5853.9	5433.2	5623.5	6085.3
$\Delta\mathrm{FC}^{\mathrm{Mean}}$	EGLL-LEMD	18.7	16.8	17.3	12.9	4.8	5.6	3.6	4.3	5.6	47.1	21.6	21.2	104.5	120.6	111.0
$\mathbb{B}(\mathrm{FC})^{\mathrm{IQR}}$	EGLL-LEMD	False	False	False	True	True	True	True	True	True	False	True	True	False	False	False
$\mathbb{B}(\mathrm{FC})^{\mathrm{Exp\pm Tol}}$	EGLL-LEMD	True	True	True	True	True	True	True	True	True	False	True	True	False	False	False
$\%\mathrm{FC}^{\mathrm{Rea\pm Tol}}$	EGLL-LEMD	88.0	92.0	92.0	74.0	94.0	94.0	90.0	90.0	88.0	36.0	60.0	60.0	16.0	18.0	16.0

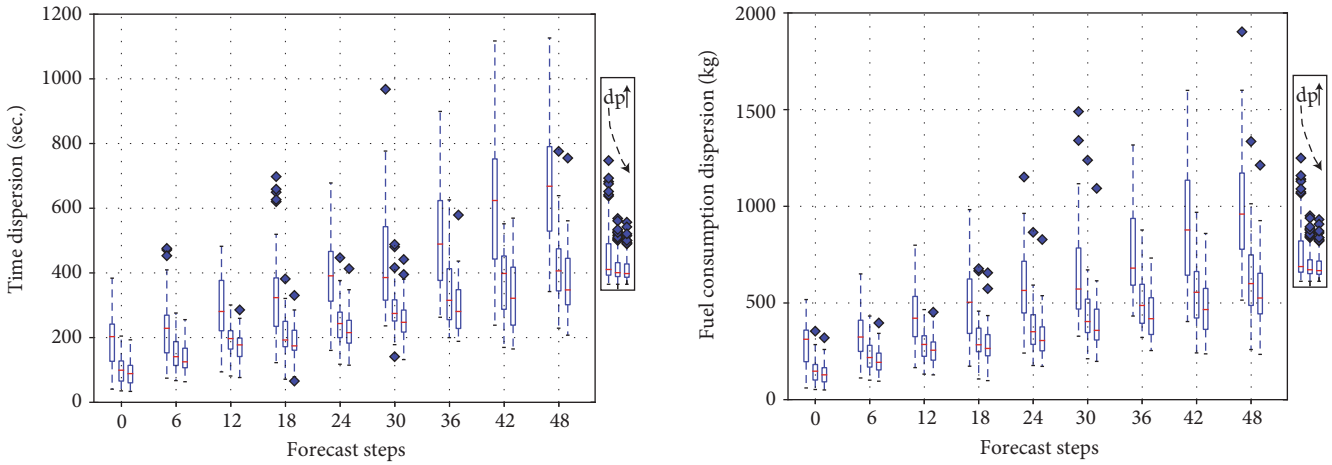

(a) Flight time dispersion (max-min value)

(b) Fuel consumption dispersion (max-min value)

Figure 13: Aggregated dispersion boxplots multiple origin-destination (long haul).

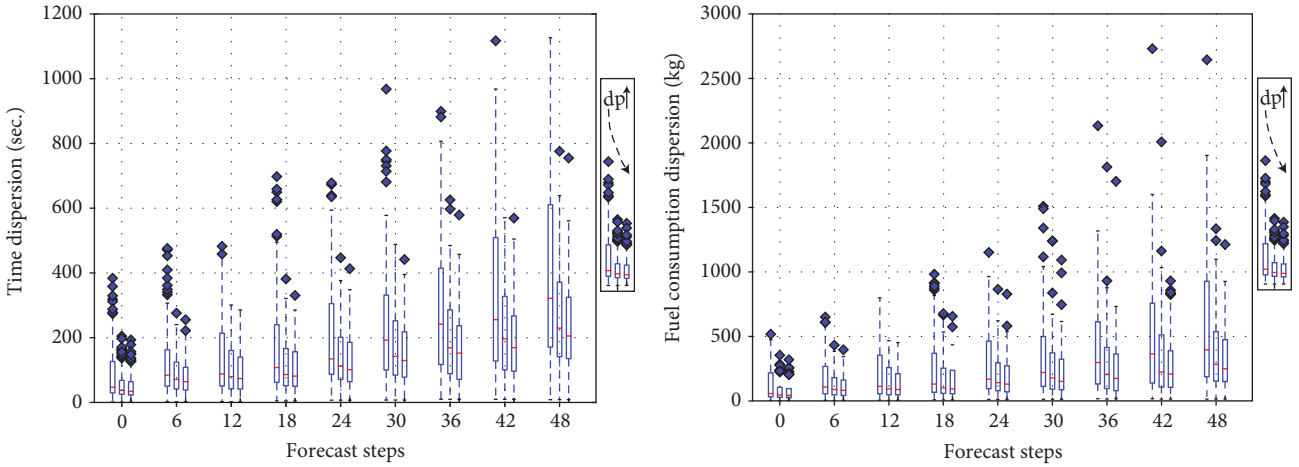

(a) Flight time dispersion (max-min value)

(b) Fuel consumption dispersion (max-min value)

Figure 14: Aggregated dispersion boxplots multiple origin-destination case study.

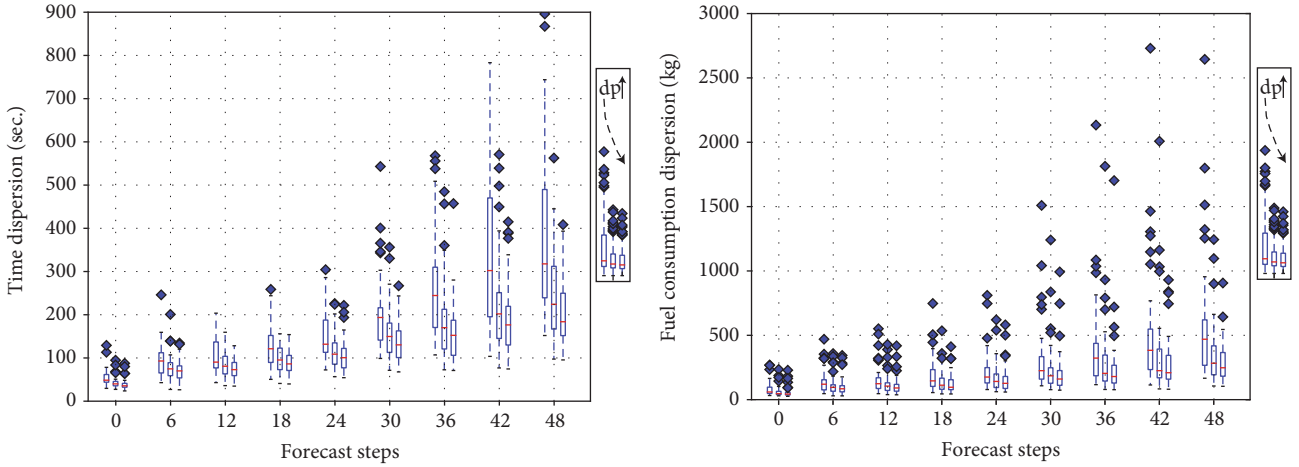

(a) Flight time dispersion (max-min value)

(b) Fuel consumption dispersion (max-min value)

Figure 15: Aggregated dispersion boxplot multiple origin-destination (medium haul).

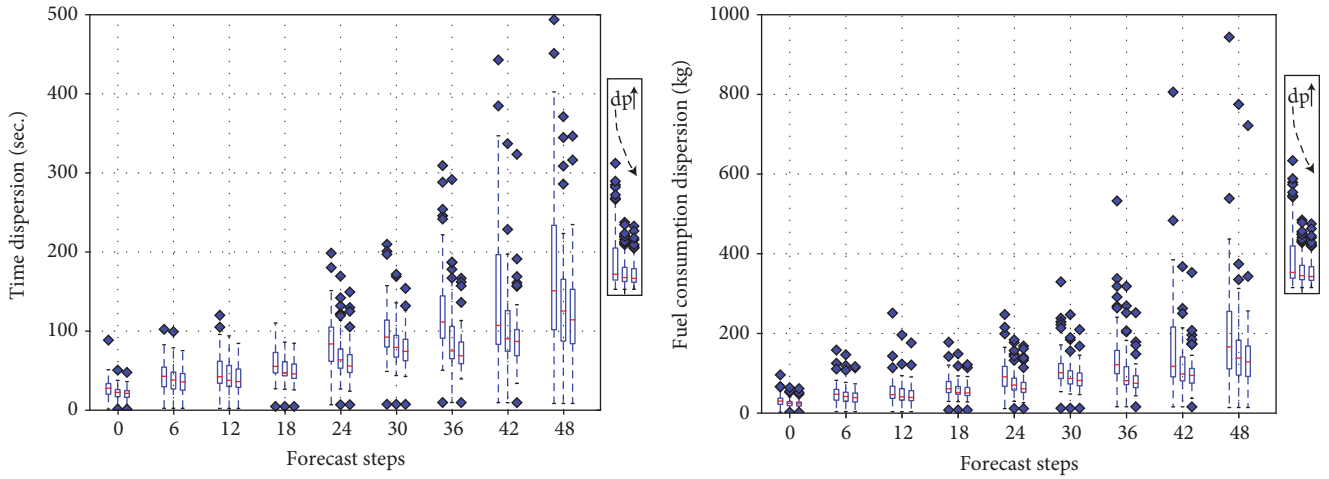

(a) Flight time dispersion (max-min value)

(b) Fuel consumption dispersion (max-min value)

Figure 16: Aggregated dispersion boxplot multiple origin-destination (short haul).

however able to reduce flight time uncertainty by roughly 40% in average. The direct effect of this would be a more accurate sector loading forecasting, leading to increase the capacity of the system. Indirectly, airlines would benefit from less regulations.

Data Availability

This research is using weather data from the ECMWF MARS public databases (https://www.ecmwf.int); therefore, the work can be replicated. Also, BADA data was used and it is accessible from the Eurocontrol website (https://simulations.eurocontrol.int/solutions/bada-aircraft-performance-model/).

Conflicts of Interest

The authors declare that there is no conflict of interest regarding the publication of this paper.

Acknowledgments

This work is partially supported by the Spanish Government through the project entitled "Analysis and Optimization of Aircraft Trajectories under the Effects of Meteorological Uncertainty-OptMet" (TRA2014-58413-C2-2-R) (https://optmet.wordpress.com/). The very first ideas of the present paper were introduced in a talk in the Workshop on Uncertainty and Air Traffic Management organized by the OptMet project on Wednesday 25th, October 2017 in Madrid (Spain).

References

[1] L. Hao, M. Hansen, M. S. Ryerson, and M. S Ryerson, "Fueling for contingencies: the hidden cost of unpredictability in the air transportation system," *Transportation Research Part D: Transport and Environment.*, vol. 44, pp. 199–210, 2016.

[2] A. Cook and D. Rivas, *Complexity Science in Air Traffic Management*, Routledge, London and New York, 2016.

[3] F. Goyens, F. Gonze, A. Simonetto, E. Huens, J. Boucquey, and R. M. Jungers, "A probabilistic model for precedence rules and reactionary delay in air traffic management," in *ICRAT 2018*, pp. 1–8, Castelldefels, Catalonia, Spain, 2018.

[4] A. Valenzuela, A. Franco, D. Rivas, J. García-Heras, and M. Soler, "Effects of reducing wind-induced trajectory uncertainty on sector demand," in *Seventh SESAR Innovation Days*, pp. 1–8, Belgrade, Serbia Republic, 2017.

[5] A. Cook, H. A. P. Blom, F. Lillo et al., "Applying complexity science to air traffic management," *Journal of Air Transport Management.*, vol. 42, pp. 149–158, 2015.

[6] E. Casado, M. L. Civita, M. Vilaplana, and E. W. McGookin, "Quantification of aircraft trajectory prediction uncertainty using polynomial chaos expansions," in *2017 IEEE/AIAA 36th Digital Avionics Systems Conference (DASC)*, pp. 1–11, St. Petersburg, FL, USA, 2017.

[7] J. Sun, J. Ellerbroek, and J. M. Hoekstra, "Aircraft initial mass estimation using Bayesian inference method," *Transportation Research Part C: Emerging Technologies*, vol. 90, pp. 59–73, 2018.

[8] R. Vazquez and D. Rivas, "Propagation of initial mass uncertainty in aircraft cruise flight," *Journal of Guidance, Control, and Dynamics*, vol. 36, no. 2, pp. 415–429, 2013.

[9] J. Cheung, J. L. Brenguier, J. Heijstek, A. Marsman, and H. Wells, "Sensitivity of flight durations to uncertainties in numerical weather prediction," in *Fourth SESAR Innovation Days*, UPM, Madrid, 2014.

[10] R. Vazquez, D. Rivas, and A. Franco, "Stochastic analysis of fuel consumption in aircraft cruise subject to along-track wind uncertainty," *Aerospace Science and Technology*, vol. 66, pp. 304–314, 2017.

[11] J. Cheung, A. Hally, J. Heijstek, A. Marsman, and J. L. Brenguier, "Recommendations on trajectory selection in flight planning based on weather uncertainty," in *Fifth SESAR Innovation Days*, Bologna, Italy, 2015.

[12] A. Franco, D. Rivas, and A. Valenzuela, "Probabilistic aircraft trajectory prediction in cruise flight considering ensemble wind forecasts," *Aerospace Science and Technology*, vol. 82-83, pp. 350–362, 2018, In Press.

[13] K. Legrand, S. Puechmorel, D. Delahaye, and Y. Zhu, "Robust aircraft optimal trajectory in the presence of wind," *IEEE Aerospace and Electronic Systems Magazine*, vol. 33, no. 11, pp. 30–38, 2018, In press.

[14] D. Gonzalez-Arribas, M. Soler, and M. Sanjurjo-Rivo, "Robust aircraft trajectory planning under wind uncertainty using optimal control," *Journal of Guidance, Control, and Dynamics*, vol. 41, no. 3, pp. 673–688, 2018.

[15] J. García-Heras, *Analysis of the geometric altimetry to support aircraft optimal trajectories within the future 4D trajectory management*, Universidad Politécnica de Madrid. School of Aeronautical Engineering, Madrid, 2014.

[16] B. Øksendal, *Stochastic Differential Equations*, Springer, Berlin, Heidelberg, 1998.

[17] A. Nuic, "User Manual for the Base of Aircraft Data (BADA)," rev 3.13, 2015.

[18] Y. Y. Park, R. Buizza, and M. Leutbecher, "TIGGE: preliminary results on comparing and combining ensembles," *Quarterly Journal of the Royal Meteorological Society.*, vol. 134, no. 637, pp. 2029–2050, 2008.

[19] L. Amodei and M. N. Benbourhim, "A vector spline approximation," *Journal of Approximation Theory.*, vol. 67, no. 1, pp. 51–79, 1991.

[20] C. Le Guyader, D. Apprato, and C. Gout, "Spline approximation of gradient fields: applications to wind velocity fields," *Mathematics and Computers in Simulation*, vol. 97, pp. 260–279, 2014.

[21] J. Andersson, J. Åkesson, and M. Diehl, "CasADi: a symbolic package for automatic differentiation and optimal control," in *Recent Advances in Algorithmic Differentiation*, Springer, Berlin, Heidelberg, 2012.

Hindawi
International Journal of Aerospace Engineering
Volume 2019, Article ID 1414279, 9 pages
https://doi.org/10.1155/2019/1414279

Research Article

Efficient Convex Optimization of Reentry Trajectory via the Chebyshev Pseudospectral Method

Chun-Mei Yu,[1,2] Dang-Jun Zhao,[3] and Ye Yang[2]

[1]*College of Aerospace and Material Engineering, National University of Defense Technology, Changsha 100854, China*
[2]*Beijing Aerospace Automatic Control Institute, Beijing 100854, China*
[3]*School of Aeronautics and Astronautics, Central South University, Changsha 410083, China*

Correspondence should be addressed to Dang-Jun Zhao; zhao_dj@csu.edu.cn

Received 5 November 2018; Revised 18 February 2019; Accepted 7 April 2019; Published 2 May 2019

Guest Editor: Xiang Li

A novel sequential convex (SCvx) optimization scheme via the Chebyshev pseudospectral method is proposed for efficiently solving the hypersonic reentry trajectory optimization problem which is highly constrained by heat flux, dynamic pressure, normal load, and multiple no-fly zones. The Chebyshev-Gauss Legend (CGL) node points are used to transcribe the original dynamic constraint into algebraic equality constraint; therefore, a nonlinear programming (NLP) problem is concave and time-consuming to be solved. The iterative linearization and convexification techniques are proposed to convert the concave constraints into convex constraints; therefore, a sequential convex programming problem can be efficiently solved by convex algorithms. Numerical results and a comparison study reveal that the proposed method is efficient and effective to solve the problem of reentry trajectory optimization with multiple constraints.

1. Introduction

The trajectory optimization problem for a hypersonic vehicle constrained by heat rating, dynamic pressure, normal load, and other constraints related to the specified mission is often a highly constrained nonlinear dynamic programming problem which, in general, can be solved by two types of methods: direct and indirect methods [1]. Indirect methods rely on solving the necessary conditions which is analytically derived from the Pontryagin minimum principles [2]. On the contrary, indirect methods, the analytical necessary conditions do not have to be derived, while the parameterization techniques are used to convert the original infinite-dimensional dynamic optimization problem to a finite-dimensional nonlinear programming problem (NLP) which can be solved by some nonlinear programming algorithms such as the well-known sequential quadratic programming (SQP) [1, 3]. There are some software packages such as GPOPS [4] and GPOCS [5] based on direct methods for addressing the trajectory optimization problems. However, these mentioned nonlinear programming algorithms cannot provide an a priori guarantee on the convergence and acquisition of a global optimal solution [6].

In recent years, convex optimization methods have been introduced to solve complex trajectory optimization problems because of their unique theoretical advantages: (1) rapid convergent rate and (2) insensitivity to the initial guess solution [7]. In [6, 8], Açıkmeşe and his coauthors proposed a lossless convexification method for solving the soft landing problem in the Mars exploration, then the highly constrained nonlinear dynamic programming problem is converted into its convex version which is efficiently solved by the second-order conic programming (SOCP) algorithm. Further, in [9], they improved their convex optimization algorithm based on the interior-point methods and thereby an efficient online algorithm for the guidance of soft landing. In [10], an SCvx optimization framework is proposed for solving nonconvex optimal control problems, in which the concave inequality constraint is successively approximated by linearization on the iterated solution rendering a

convex optimization problem suited to be solved by SOCP algorithms. This convex optimization method has been successfully used for addressing trajectory optimization problems of hypersonic vehicles [11].

Actually, as for the aforementioned SCvx optimization methods, the appropriate techniques of linearization and discretization are the key factors ensuring that the solution of the convexified problem is still the solution of the original problem. Hence, additional constraints of the trust region are applied to guarantee the validity of linearization in [10, 11]. Our previous study [7] reveals that the trust region should be carefully selected: if the trust region is given too large, the conditions of linearization will be violated and therefore the solution of the convexified problem is not that of the original problem; on the contrary, a smaller trust region will result in larger iterations and make the convergent rate slower.

In the procedure of discretization mentioned in [6–11], the uniformly distributed discretized points are chosen to transform the original infinite-dimensional optimization problem into a finite-dimensional parameter optimization problem. With such numerical discretization scheme, the discretized interval should be sufficiently small in order to obtain a sufficiently accurate solution, while this leads a high-dimensional transformed problem which is time-consuming to be solved. Actually, the pseudospectral methods have been widely used to solve the trajectory optimization problems, such as the Radau-Gauss pseudospectral method in [4, 5] and the Chebyshev method in [12–14]. The Chebyshev pseudospectral method is a special case of the general spectral methods, in which the functions can be expanded in terms of interpolating polynomials and the expansion coefficients are the values of the function at the Gauss quadrature node points, thereby having the best accuracy in interpolation of a function [12]. It has been shown that interpolation at the Chebyshev-Gauss Legend (CGL) nodes presents a closest result to the optimal polynomial approximation to a given function [15].

In this study, we develop a new SCvx optimization algorithm based on the Chebyshev pseudospectral method to improve the SCvx optimization method proposed in our previous work [7], in which the dynamic programming problem of reentry trajectory optimization is transcribed into a nonlinear programming problem by using the equispace discretizing technique, and then the convexification method and SCvx algorithm are employed to efficiently obtain the optimal trajectory. However, in order to obtain a sufficient well solution, the discretization points in the manner of equispace must be sufficiently large due to the requirement of discretizing accuracy. Based on the advantages of the Chebyshev psuedospectral method, CGL node points are used to discretize and approximate the state and control variables, therefore having more accurate approximations and less discretized points than using equispace discretized points. The less discretized points mean that less decision variables in the transformed SCvx problem and, consequently, the computational cost will be dramatically reduced, and this is validated by numerical study results in Section 4.

2. Problem Formulation

The reentry trajectory optimization problem, including the reentry motion model, various constraints, and the performance index, is formulated in this section. Further, the corresponding convexification techniques are particularly demonstrated.

2.1. Reentry Dynamics of CAV. For simplicity, the nonrotating earth with constant gravitational acceleration is applied during modelling the motion of CAV; meanwhile, it assumes that CAV's motion is with small flight path angle and limited control input (bank angle and angle of attack). Then, the nondimensional equation of CAV is given as [16].

$$\begin{cases} \dot{x} = v\cos\theta, \\ \dot{y} = v\sin\theta, \\ \dot{h} = v\gamma, \\ \dot{v} = \dfrac{-Bv^2 e^{-\beta R_e h}\left(1+\lambda^2\right)}{2E^*}, \\ \dot{\gamma} = Bve^{-\beta R_e h}\lambda\cos\sigma - 1/v + v, \\ \dot{\theta} = Bve^{-\beta R_e h}\lambda\sin\sigma. \end{cases} \tag{1}$$

Here, the independent variable is dimensionless time t which is normalized by $\sqrt{R_e/g_e}$ (R_e is the earth's radius, g_e is the gravitational acceleration at sea level), states x and y are the horizontal positions normalized by the earth's radius R_e, states h and v are the dimensionless altitude and velocity of the vehicle, and γ and θ are the flight path angle and heading angle, respectively. The vehicle-specific constant B is defined by$B = \rho_0 R_e S_{ref} C_L^*/(2m)$, in which ρ_0 is the atmospheric density at sea level, S_{ref} is the aerodynamic reference area, m is the vehicle mass, and C_L^* andC_D^*, respectively, are the coefficients of lift and drag which produce the maximum lift-to-drag ratio $E^* = C_L^*/C_D^*$ for CAV. The control variables in (1) are the bank angle σ and the normalized coefficient of lift $\lambda = C_L/C_L^*$ where C_L is the lift coefficient of the vehicle. Thus, the coefficient of lift and drag can be represented by $C_L = \lambda C_L^*$ and $C_D = C_L^*(1+\lambda^2)/2E^*$, respectively. The further details of the aerodynamics of CAV can be found in the literature [17]. For convenience, we rewrite (1) as the following general nonlinear system

$$\dot{\mathbf{x}} = \mathbf{f}(\mathbf{x}, \mathbf{u}, t), \tag{2}$$

where the state vector $\mathbf{x} = [x, y, h, v, \gamma, \theta]^T$ and the control vector is $\mathbf{u} = [\lambda, \sigma]^T$.

2.2. Flight Constraints. During the entry flight of CAV, the strong path constraints, such as heating flux, dynamic pressure, and load factor, should be satisfied for guaranteeing the safety of the vehicle. Moreover, in many cases, to avoid the enemy's detection and interception, no-fly zone constraints should be considered in the trajectory planning such that the vehicle keeps away from the area with the deployment of missile defense systems.

2.2.1. Path Constraints. In this research, the path constraints including the maximal heating rate, dynamic pressure, and load factor are considered for the safe flight of the vehicle. According to [7], the dimensional atmospheric density ρ is reasonably assumed be an exponential function of the nondimensional altitude $h = (R - R_e)/R_e$ with the form

$$\rho = \rho_0 e^{-\beta R_e h}. \tag{3}$$

Then, the normalized path constraints are defined by

$$\mathbf{P}_1(\mathbf{x}(t), t) = \begin{bmatrix} \bar{k}_Q e^{-0.5\beta R_e h} v^3 - 1 \\ \bar{k}_q e^{-\beta R_e h} v^2 - 1 \\ \bar{k}_n e^{-\beta R_e h} v^2 \sqrt{4E^{*2}\lambda^2 + \left(1+\lambda^2\right)^2} - 1 \end{bmatrix} \leq \mathbf{0}_{3\times 1}, \tag{4}$$

in which the normalized coefficients are defined by $\bar{k}_Q = k_Q \rho_0 (\sqrt{g_e R_e})^3 / \dot{Q}_{\max}$, $\bar{k}_q = 0.5\rho_0 g_e R_e / q_{\max}$, and $\bar{k}_n = 0.5\rho_0 R_e S_{\text{ref}} C_L^{*2} / (m n_{\max})$, where $\dot{Q}_{\max}$ (W/m^2), $q_{\max}$ (N/m^2), and $n_{\max}$, respectively, are the maximum allowable heating rate, dynamic pressure, and loading factor.

2.2.2. No-Fly Zone Constraints. No-fly zones (NFZs) are considered in this paper which are defined as circular exclusion zones in the horizontal plane with infinite altitude; thus, n_{NFZ} NFZs can be specified by their centre $\mathbf{C}_j^{\text{NFZ}} = [x_j y_j]^T$ and the corresponding radius R_j^{NFZ} for $j = 1, \cdots, n_{\text{NFZ}}$. Then, NFZs constraints are formulated as

$$N_{\substack{j \\ j=1,\cdots,n_{NFZ}}}\left(\mathbf{x}(t), \mathbf{C}_j^{\text{NFZ}}, R_j^{\text{NFZ}}\right) = \left\| \begin{bmatrix} x - x_j & y - y_j \end{bmatrix}^T \right\| \geq R_j^{\text{NFZ}}. \tag{5}$$

2.2.3. Boundary Constraints. According to the mission profile of CAV, the vehicle's entry start and the target point are prescribed; therefore, the following boundary constraints are

$$\mathbf{\Gamma}(\mathbf{x}(t_0), \mathbf{x}_0) = \mathbf{0}, \quad \mathbf{\Psi}\left(\mathbf{x}\left(t_f\right), \mathbf{x}_f\right) = \mathbf{0}, \tag{6}$$

where $\mathbf{x}_0$ and $\mathbf{x}_f$, respectively, are the given initial states and terminal states which should be satisfied in the optimized trajectory [16].

2.2.4. Control Constraints. During the entry of CAV, due to the vehicle's aerodynamic characteristics, the normalized lift coefficient λ is confined in a certain range (for example [0,2]). Further, the bank angle σ is bounded to guarantee the stability. Then, the inequality constraints imposed on the controls are formulated as

$$\mathbf{C}(\mathbf{u}, t) = \begin{bmatrix} |\sigma| - \sigma_{\max} \\ \lambda - 2 \\ -\lambda \end{bmatrix} \leq \mathbf{0}. \tag{7}$$

It is noteworthy that if we directly use σ and λ as control variables in the followed SCvx algorithm, the sinusoidal function of σ in (1) will result in the chattering phenomenon in the solution. The detailed reason can be found in [11]. Consequently, in accordance with the treatment proposed in [18], three new control variables are defined as follows to replace the original control variables in order to conveniently convexify the control constraints.

$$\begin{aligned} u_1 &= \lambda \cos\sigma, \\ u_2 &= \lambda \sin\sigma, \\ u_3 &= \lambda^2 = u_1^2 + u_2^2, \\ \mathbf{u} &= \left[u_1, u_2, u_3\right]^T. \end{aligned} \tag{8}$$

Then, the constraints in (7) are reformulated as

$$\tilde{\mathbf{C}}(\mathbf{u}, \tau) = \begin{bmatrix} -u_3 \\ u_3 - 4 \\ -u_2 - u_1 \tan\sigma_{\max} \\ u_2 - u_1 \tan\sigma_{\max} \end{bmatrix} \leq \mathbf{0}, \tag{9}$$

with an auxiliary equality constraint

$$C_e = u_1^2 + u_2^2 - u_3 = 0. \tag{10}$$

2.3. Reentry Trajectory Optimization Problem. In the general trajectory optimization problem, there are several choices of performance indices to specify different optimization objectives such as maximum range, minimum heat load, and minimum time. In this research, minimum time is chosen as the performance index; thus, the reentry trajectory optimization problem is formulated as

$$\begin{aligned} P0: \quad & \min \int_0^{t_f} 1 \mathrm{d}t, \\ & \text{subject to } (2), (4), (5), (6), (9), (10). \end{aligned} \tag{11}$$

3. Sequential Convex Optimization Based on the Chebyshev Pseudospectral Method

In this section, the Chebyshev pseudospectral method is introduced to reformulate the original dynamic optimization problem (11) as an SCvx programming problem in order to be efficiently solved by the convex optimization algorithms. First, the infinite-dimensional trajectory optimization problem is discretized by the Chebyshev pseudospectral method and henceforth a finite-dimensional parameter optimization problem. Then, the sequential convex optimization problem is formulated to be solved by the SOCP algorithm.

3.1. Chebyshev Pseudospectral Method. In the classical Chebyshev pseudospectral method, the CGL points are given by $\tau_k = \cos(\pi k/N)$ for $k = 0, \cdots, N$, then the node points range from 1 to -1. Since such order is inconvenient for the

trajectory optimization problem, then the modified CGL points proposed by [12] with the form,

$$\tau_k = -\cos\left(\frac{\pi k}{N}\right), \quad k = 0, \cdots, N, \tag{12}$$

are employed in this work. The corresponding i^{th} order Chebyshev polynomial is

$$P_i = \cos\left(i\cos^{-1}\tau\right), \quad i = 0, \cdots, N, \tag{13}$$

where $\tau \in [-1, 1]$ can be mapped from the independent variable t by the equation $t = (t_f - t_0)\tau/2 + (t_f + t_0)/2$. If $t_0 = 0$, then$t = t_f(\tau + 1)/2$. Consequently, problem P0 is equivalent to the following problem P1.

$$\text{P1} : \min \quad t(1), \tag{14}$$

$$\text{subject to} \quad \frac{\mathrm{d}\mathbf{X}}{\mathrm{d}\tau} = \frac{t_f}{2}\begin{bmatrix}\mathbf{f}(\mathbf{x}, \mathbf{u}, \tau)\\ 1\end{bmatrix} = \mathbf{F}(\mathbf{X}, \mathbf{U}, \tau), \quad \tau \in [-1, 1], \tag{15}$$

$$\begin{aligned}\boldsymbol{\Gamma}(\mathbf{X}(-1), \mathbf{X}_0) &= \mathbf{0},\\ \boldsymbol{\Psi}\left(\mathbf{X}(1), \mathbf{X}_f\right) &= \mathbf{0},\end{aligned} \tag{16}$$

$$\begin{aligned}\mathbf{G}(\mathbf{X}, \mathbf{U}, \tau) &= \begin{bmatrix}\mathbf{P}_1(\mathbf{x}(\tau), \tau)\\ -N_j\left(\mathbf{x}(\tau), \mathbf{C}_j^{\text{NFZ}}, R_j^{\text{NFZ}}\right)\\ {\scriptstyle j=1,\cdots,n_{\text{NFZ}}}\end{bmatrix}\\ &\le 0, \; j = 1, \cdots, n_{\text{NFZ}},\end{aligned} \tag{17}$$

$$\mathbf{C}(\mathbf{U}, \tau) = \begin{bmatrix}\tilde{\mathbf{C}}(\mathbf{u}, \tau)\\ -t_f\end{bmatrix} \le 0, \tag{18}$$

$$C_{\text{e}} = 0, \tag{19}$$

where the augment state $\mathbf{X} = [\mathbf{x}^T, t]^T$ and the control variable $\mathbf{U} = [\mathbf{u}^T, t_f]^T$ are used in (15) to reformulate the original time-free problem (11) as a time-fixed problem for the convenience of the following discretized manipulations; meanwhile, Lagrange's problem P0 is converted into Mayer's problem, which is suited to be solved by convex programming since its performance index is linear in nature. In (16), $\mathbf{X}_0 = [\mathbf{x}_0^T, t_0]^T$ and $\mathbf{X}_f = [\mathbf{x}_f^T, t_f]^T$. The constraints in (17) are the general form of the aforementioned nonlinear constraints (4) and (5). The augmented control variable t_f is constrained by $t_f \ge 0$ in (18). The state and control vectors of (15) can be approximated by

$$\mathbf{X}(\tau) = \sum_{i=0}^{N} \mathbf{X}(\tau_i)\Phi_i(\tau), \tag{20}$$

$$\mathbf{U}(\tau) = \sum_{i=0}^{N} \mathbf{U}(\tau_i)\Phi_i(\tau), \tag{21}$$

where the basis N-order Lagrange interpolating polynomials $\Phi_i(\tau)$ for $i = 0, 1, \cdots, N$ are given by

$$\Phi_i(\tau) = \frac{(-1)^{i+1}}{N^2 c_i}\frac{\left(1 - t^2\right)\dot{P}_N(\tau)}{\tau - \tau_i}, \tag{22}$$

with

$$c_i = \begin{cases}2, & i = 0, N,\\ 1, & 1 \le i \le N - 1.\end{cases} \tag{23}$$

Differentiating (20) at each CGL point yields the derivative approximation with the following form

$$\dot{\mathbf{X}}(\tau_k) = \sum_{i=0}^{N} \mathbf{X}(\tau_i)\dot{\Phi}_i(\tau_k) = \sum_{i=0}^{N} D_{ki}\mathbf{X}(\tau_i), \tag{24}$$

where D_{ki} are the entries of the differentiation matrix $\mathbf{D} \in \mathbb{R}^{(N+1)\times(N+1)}$and can be obtained by

$$\mathbf{D} \coloneqq [D_{ki}] \coloneqq \begin{cases}-\left(\dfrac{c_k}{c_i}\right)\left[\dfrac{(-1)^{i+k}}{\tau_k - \tau_i}\right], & j \ne k,\\ \dfrac{\tau_k}{2\left(1 - \tau_k^2\right)}, & 1 \le i = k \le N - 1,\\ -\dfrac{2N^2 + 1}{6}, & i = k = 0,\\ \dfrac{2N^2 + 1}{6}, & i = k = N.\end{cases} \tag{25}$$

Thus, the dynamic constraint of (15) is transcribed into an algebraic constraint as

$$\sum_{i=0}^{N} D_{ki}\mathbf{X}(\tau_i) - \mathbf{F}(\mathbf{X}_k, \mathbf{U}_k, \tau_k) = 0, \quad (k = 0, \cdots, N), \tag{26}$$

where $\mathbf{X}_k \equiv \mathbf{X}(\tau_k)$ and $\mathbf{U}_k \equiv \mathbf{U}(\tau_k)$. It is to be noted that if the function $\mathbf{F}(\mathbf{X}, \mathbf{U}, \tau)$ in (15) is a linear function of $\mathbf{X}$ and $\mathbf{U}$, then (26) will be a series of linear equality constraints which are convex in nature. Unfortunately, $\mathbf{F}(\mathbf{X}, \mathbf{U}, \tau)$ is a strong nonlinear function; hence, the further convexification technique should be employed in order to formulate an SCvx problem.

3.2. Convexification. In the above subsection, the dynamic constraint is transformed into an algebraic constraint via the Chebyshev pseudospectral method, and the trajectory optimization problem can be reformulated as an NLP problem which cannot be directly solved by convex optimization algorithms. Hence, appropriate convexification techniques are required to reformulate problem P1 as an SCvx problem. It is obvious that the constraints in (15) and (17)–(19) are concave and should be convexified.

3.2.1. Convexification of Dynamic Constraints. Due to the iterative nature of sequential optimization algorithms, we suppose a reference trajectory denoted by $\{\mathbf{X}^n(\tau), \mathbf{U}^n(\tau)\}$ which is provided by the n-th iteration solution of the SCvx algorithm, then in the $(n+1)^{-\text{th}}$ iteration, the dynamic equation (15) can be linearized along the reference trajectory $\{\mathbf{X}^n(\tau), \mathbf{U}^n(\tau)\}$ as

$$\frac{\mathrm{d}\mathbf{X}}{\mathrm{d}\tau} = \mathbf{A}^n(\mathbf{X}^n, \mathbf{U}^n, \tau)\mathbf{X} + \mathbf{B}^n(\mathbf{X}^n, \mathbf{U}^n, \tau)\mathbf{U} + \mathbf{C}^n(\mathbf{X}^n, \mathbf{U}^n, \tau), \tag{27}$$

where $\mathbf{A}^n$ and $\mathbf{B}^n$, the Jacobian matrices of $\mathbf{F}$ with respect to $\mathbf{X}$ and $\mathbf{U}$, are given by

$$\mathbf{A}^n = \partial\mathbf{F}/\partial\mathbf{X}\big|_{\mathbf{X}^n(\tau),\mathbf{U}^n(\tau)} = \frac{1}{2}\begin{bmatrix} 0 & 0 & 0 & t_f\cos\theta & 0 & -t_f v\sin\theta & 0 \\ 0 & 0 & 0 & t_f\sin\theta & 0 & t_f v\cos\theta & 0 \\ 0 & 0 & 0 & t_f\gamma & t_f v & 0 & 0 \\ 0 & 0 & \dfrac{t_f\beta R_e B v^2 e^{-\beta R_e h}(1+u_3)}{2E^*} & \dfrac{-t_f B v e^{-\beta R_e h}(1+u_3)}{E^*} & 0 & 0 & 0 \\ 0 & 0 & -t_f\beta R_e B v e^{-\beta R_e h}u_1 & t_f\left(B e^{-\beta r_0 h}u_1 + 1/v^2 + 1\right) & 0 & 0 & 0 \\ 0 & 0 & -t_f\beta R_e B v e^{-\beta R_e h}u_2 & t_f B e^{-\beta R_e h}u_2 & 0 & 0 & 0 \\ 0 & 0 & 0 & 0 & 0 & 0 & 0 \end{bmatrix}_{\mathbf{X}^n(\tau),\mathbf{U}^n(\tau)},$$

$$\mathbf{B}^n = \partial\mathbf{F}/\partial\mathbf{U}\big|_{\mathbf{X}^n(\tau),\mathbf{U}^n(\tau)} = \frac{1}{2}\begin{bmatrix} 0 & 0 & 0 & v\cos\theta \\ 0 & 0 & 0 & v\sin\theta \\ 0 & 0 & 0 & v\gamma \\ 0 & 0 & \dfrac{-t_f B v^2 e^{-\beta R_e h}}{2E^*} & \dfrac{-B v^2 e^{-\beta R_e h}(1+u_3)}{2E^*} \\ t_f B v e^{-\beta R_e h} & 0 & 0 & B v e^{-\beta R_e h}u_1 - 1/v + v \\ 0 & t_f B v e^{-\beta R_e h} & 0 & B v e^{-\beta R_e h}u_2 \\ 0 & 0 & 0 & 1 \end{bmatrix}_{\mathbf{X}^n(\tau),\mathbf{U}^n(\tau)}. \tag{28}$$

The residue term can be calculated by

$$\mathbf{C}^n(\mathbf{X}^n, \mathbf{U}^n, \tau) = \mathbf{F}(\mathbf{X}^n, \mathbf{U}^n, \tau) - \mathbf{A}^n(\mathbf{X}^n, \mathbf{U}^n, \tau)\mathbf{X}^n - \mathbf{B}^n(\mathbf{X}^n, \mathbf{U}^n, \tau)\mathbf{U}^n. \tag{29}$$

Similar to references [7, 10], additional constraints of the trust region are denoted by the following element-wise inequalities

$$\begin{aligned} |\mathbf{X} - \mathbf{X}^n| &< \boldsymbol{\varepsilon}_X, \\ |\mathbf{U} - \mathbf{U}^n| &< \boldsymbol{\varepsilon}_U, \end{aligned} \tag{30}$$

where $\boldsymbol{\varepsilon}_X \in \mathbf{R}^7$ and $\boldsymbol{\varepsilon}_U \in \mathbf{R}^4$ are imposed to make the linearized system sufficiently approximate to the original nonlinear system. Actually, the constraints of the trust region (30) confine the deviated trajectory in a prescribed neighbourhood about the reference trajectory $\{\mathbf{X}^n(\tau), \mathbf{U}^n(\tau)\}$.

Discretizing (27) on the CGL node points like (26) yields the following convex (linear) algebraic equality constraints:

$$\sum_{i=0}^{N} D_{ki}\mathbf{X} = \mathbf{A}_k^n(\mathbf{X}_k^n, \mathbf{U}_k^n, \tau)\mathbf{X} + \mathbf{B}_k^n(\mathbf{X}_k^n, \mathbf{U}_k^n, \tau)\mathbf{U} + \mathbf{C}_k^n(\mathbf{X}_k^n, \mathbf{U}_k^n, \tau), \quad (k = 0, \cdots, N), \tag{31}$$

which will enforce the solution at $N+1$ CGL node points exactly satisfying the dynamic constraint (15).

3.2.2. Convexification of Path Constraints. Each entry of the concave path constraints (17) can be represented by a generalized inequality as

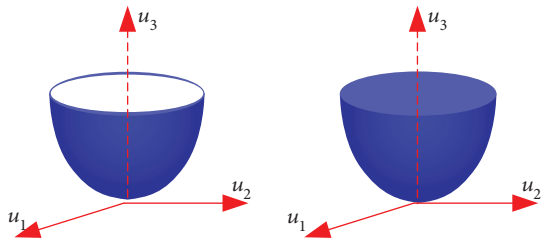

Figure 1: [18] Relaxation of control constraints. (Left) original nonconvex set: blue surface (10). (Right) relaxed convex set: blue cone includes its surface (34) Reproduced from Liu et al. [18] (under the Creative Commons Attribution License/public domain).

Table 1: CAV mission description.

	Latitude (deg)	Longitude (deg)	Radius (km)
Initial point	N 28.5	W -80.6	—
NFZ1	N 20.1	W -3.4	177.7920
NFZ2	N 55.6	E 58.5	277.8000
Target	N 31.2	E 65.7	—

$$g_p(\mathbf{X}, \mathbf{U}, \tau) \le 0, \quad p = 1, \cdots, m, \tag{32}$$

where m is the number of path constraints.

In the scenario of trajectory linearization and discretization, the abovementioned concave inequality constraints can be reformulated as

$$g_p(\mathbf{X}_k^n, \mathbf{U}_k^n) + \nabla g_p^T(\mathbf{X}_k^n)(\mathbf{X} - \mathbf{X}_k^n) + \nabla g_p^T(\mathbf{U}_k^n)(\mathbf{U} - \mathbf{U}_k^n) \le 0, \quad k = 0, 1, 2, \cdots N, \tag{33}$$

where $\nabla g_p(\mathbf{X}_k^n)$ and $\nabla g_p^T(\mathbf{U}_k^n)$, respectively, are the gradients of g_p at $\mathbf{X}_k^n$ and $\mathbf{U}_k^n$. Note that the trust region defined by (30) is necessary in order to guarantee the linearized constraints in (33) reasonably approximate to the original constraints in (17). Lemma 1 of [10] presented a theoretical illustration in which the feasible solution of P1 comes from the linearized inequality constraints. Equation (33) is also the feasible solution of the original problem.

3.2.3. Convexification of Control Constraints. The equality constraint on the control variables in (19) is obviously concave. We relax the strong equality constraints to a convex inequality constraint as follows [7, 18]:

$$u_1^2 + u_2^2 \le u_3, \tag{34}$$

which is shown by the blue cone including its surface on the right side of Figure 1. Auxiliary inputs u_1 and u_2 are limited by u_3 and the maximum bank angle $\sigma_{\max}$ as illustrated by the left image in Figure 1. And the relaxed constraint illustrated by the right image in Figure 1 is obviously convex.

3.3. Sequential Convex Optimization Problem. After the convexifications of path constraints and the control constraints,

Table 2: Comparison of the minimum-time solution for CAV.

Method	Number of discretized points	Iteration number	Optimal index (s)	CPU time (s)
Cheb-SCvx	25	7	3056.4	5.59
	30	18	2860.5	14.20
	40	8	2862.6	6.75
	60	6	2909.5	5.68
	80	6	2968.4	12.21
Eq-SCvx	300	7	2869.2	11.15
	250	10	2893.8	15.42
GPOPS	-	-	3100.0	20.430

the optimal solution of P1 is obtained by solving the following relaxed sequential convex optimal problems defined on the CGL node points for $n = 0,1,2 \cdots$:

$$\text{P2} : \min t(1), \tag{35}$$

$$\text{subject to} \quad \sum_{i=0}^{N} D_{ki}\mathbf{X} = \mathbf{A}_k^n(\mathbf{X}_k^n, \mathbf{U}_k^n, \tau)\mathbf{X} + \mathbf{B}_k^n(\mathbf{X}_k^n, \mathbf{U}_k^n, \tau)\mathbf{U} + \mathbf{C}_k^n(\mathbf{X}_k^n, \mathbf{U}_k^n, \tau), \quad (k = 0, \cdots, N, n = 1, 2, \cdots), \tag{36}$$

$$\begin{aligned} \boldsymbol{\Gamma}(\mathbf{X}(-1), \mathbf{X}_0) &= \mathbf{0}, \\ \boldsymbol{\Psi}(\mathbf{X}(1), \mathbf{X}_f) &= \mathbf{0}, \end{aligned} \tag{37}$$

$$g_p(\mathbf{X}_k^n, \mathbf{U}_k^n) + \nabla g_p^T(\mathbf{X}_k^n)(\mathbf{X} - \mathbf{X}_k^n) + \nabla g_p^T(\mathbf{U}_k^n)(\mathbf{U} - \mathbf{U}_k^n) \le 0, \quad k = 0, 1, 2, \cdots N, \tag{38}$$

$$u_1^2 + u_2^2 \le u_3, \tag{39}$$

$$0 \le u_3 \le 4, \tag{40}$$

$$-\tan(\sigma_{\max})u_1 \le u_2 \le \tan(\sigma_{\max})u_1, \tag{41}$$

$$\begin{aligned} |\mathbf{X} - \mathbf{X}^n| &< \boldsymbol{\varepsilon}_X, \\ |\mathbf{U} - \mathbf{U}^n| &< \boldsymbol{\varepsilon}_U. \end{aligned} \tag{42}$$

3.4. SCvx Algorithm. According to the solution procedure of the sequential convex programming method, the SCvx algorithm to find the original problem P0 is given as follows.

Step 1. Set $n = 0$, and choose an initial control profile $\mathbf{U}^0(\tau_k)$ $(k = 0, 1, 2, N)$ on the CGL node points. An easy choice is set $\lambda_k = 1$ and bank angle $\sigma_k = 0$. Then driven by $\mathbf{U}^0(\tau_k)$, numerical integration is conducted according to the dynamical model in (1); we henceforth have the initial state profile $\mathbf{X}^0(\tau_k)$.

Step 2. At the $(n+1)^{\text{th}}$ iteration, problem P2 is set up by using $\{\mathbf{X}^n(\tau_k), \mathbf{U}^n(\tau_k)\}$, meanwhile point-wisely checking

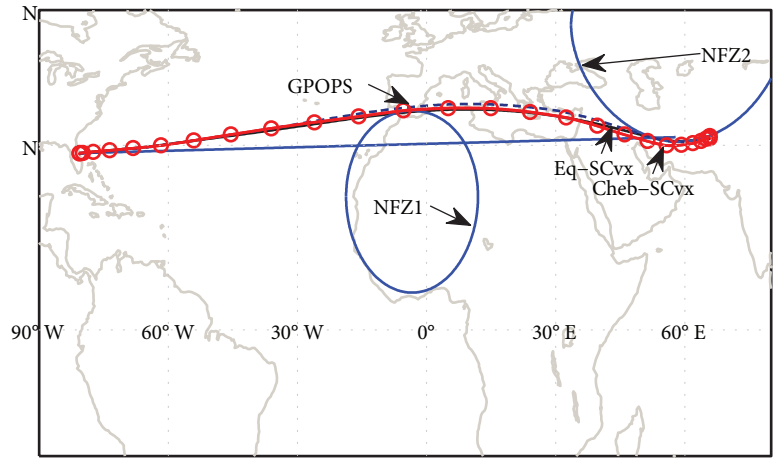

Figure 2: Ground tracks of CAV.

the violation states of the heat flux, dynamic pressure, load factor, and NFZ constraints defined in (4). If all or some of these constraints are violated, the corresponding convexified constraints in (38) are set up. Then solving problem P2 by the SOCP algorithm yields the solution denoted by $\{\mathbf{X}^{n+1}(\tau_k), \mathbf{U}^{n+1}(\tau_k)\}$.

Step 3. Check whether the convergence condition as follows is satisfied:

$$\max \quad \left|\mathbf{X}^{n+1} - \mathbf{X}^{n}\right| \le \boldsymbol{\delta}, \tag{43}$$

which consists of a series of component-wise inequalities; $\boldsymbol{\delta}$ is a prescribed sufficiently small constant vector. Moreover, the constraints defined in (4) are point-wisely calculated. If all these constraints on the CGL node points and the convergence condition in (43) are satisfied, go to Step 4; otherwise, set $n = n + 1$ and go back to Step 2.

Step 4. The solution for P0 is found to be $\{\mathbf{X}^{n+1}(\tau_k), \mathbf{U}^{n+1}(\tau_k)\}$. Stop.

4. Numerical Results

In this section, the hypersonic gliding vehicle (CAV-H) described by (1) is used to validate the proposed algorithm in the above section. The MATLAB modelling tool YALMIP [19] is used to formulate the SOCP problem P2, and a light embedded SOCP solver ECOS [20] is used to obtain the solution. The all-solution procedure is executed on a laptop computer with Intel Core i5-4200 at 2.5 GHz.

The CAV mission is described in Table 1, which defines the horizontal positions of the initial and target points, as well as two waypoints during the flight. The radius of the first NFZ is chosen to be much smaller than the turn capability of the CAV, while the second NFZ has a large enough radius. The path constraints imposed on the trajectory are given by $\dot{Q}_{\max} = 4000\,\mathrm{kW/m^2}$, $q_{\max} = 5 \times 10^5\,\mathrm{N/m^2}$, and $n_{\max} = 2.5 g_e$. The boundary conditions are as follows: $h_0 = 122\,\mathrm{km}$, $v_0 = 7315.2\,\mathrm{m/s}$, $\gamma_0 = -1.5^\circ$, $\theta_0 = 4^\circ$, $h_f \ge 20\,\mathrm{km}$, $v_f \ge 2000\,\mathrm{m/s}$, and $\gamma_f = -4^\circ$. The terminal flight heading angle is not constrained. In addition, the bank angle are limited by $\sigma_{\max} = \pi/3$. The trust region in (42) is given as

$$\begin{aligned} \left|\mathbf{X} - \mathbf{X}^{n}\right| &\le \left[\begin{array}{cccccc} 0.2 & 0.2 & \dfrac{10000}{R_e} & \dfrac{5000}{\sqrt{g_e R_e}} & \dfrac{\pi}{6} & \dfrac{\pi}{6} \end{array}\right]^T, \\ \left|\mathbf{U} - \mathbf{U}^{n}\right| &\le \left[\begin{array}{cccc} 0.5 & 0.5 & 1 & 0.5 \end{array}\right]^T, \end{aligned} \tag{44}$$

which is sufficiently large to satisfy Assumption 1 presented by [7]. The stopping criterion $\boldsymbol{\delta}$ in (43) is set as $\boldsymbol{\delta} = [0.03 \quad 0.03 \quad 0.003 \quad 0.04 \quad 0.06 \quad 0.03]^T$.

To verify the proposed SCvx algorithm via Chebyshev pseudospectral method (denoted by Cheb-SCvx), a comparison study between the proposed SCvx method in [7] (denoted by Eq-SCvx) as well as GPOPS is conducted. In the Eq-SCvx method, the equal-space discretized scheme is employed, while GPOPS uses the hp-adaptive Radau pseudospectral method to solve optimal control problems. Similar to the proposed method in Section 3, we use the new controls u_1, u_2, and u_3 to replace the original controls (λ and σ) in (1).

The comparison of numerical solutions obtained by Cheb-SCvx, Eq-SCvx, and GPOPS is presented in Table 2, which reveals that the proposed Cheb-SCvx method is more efficient and effective than Eq-SCvx and GPOPS while dealing with the highly constrained entry trajectory optimization problems. It is to be noted that, in the Eq-SCvx algorithm, when the discretized point number is less than 250, the algorithm cannot converge, and no solution can be obtained. The reason lies in the fact that less discretized points result in a larger distance between two adjacent points; thus, the linearization condition in (27) will be violated. And after multiple numerical experiments, we can ascertain that the appropriate number of CGL node points will extremely reduce the computational time and improve the performance index.

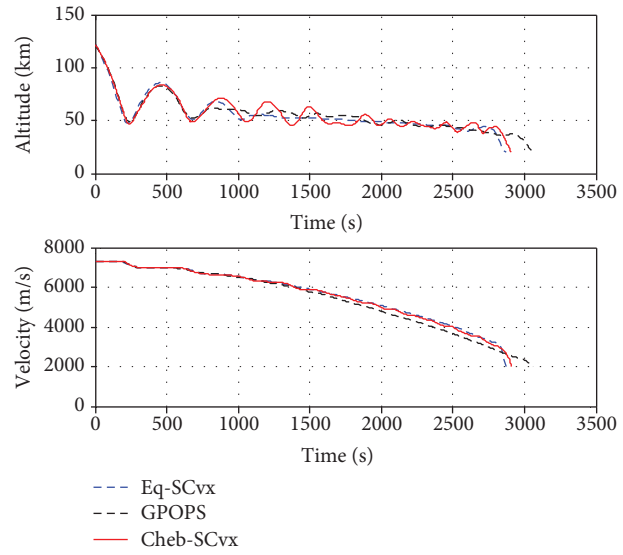

Figure 3: Altitude and velocity profile.

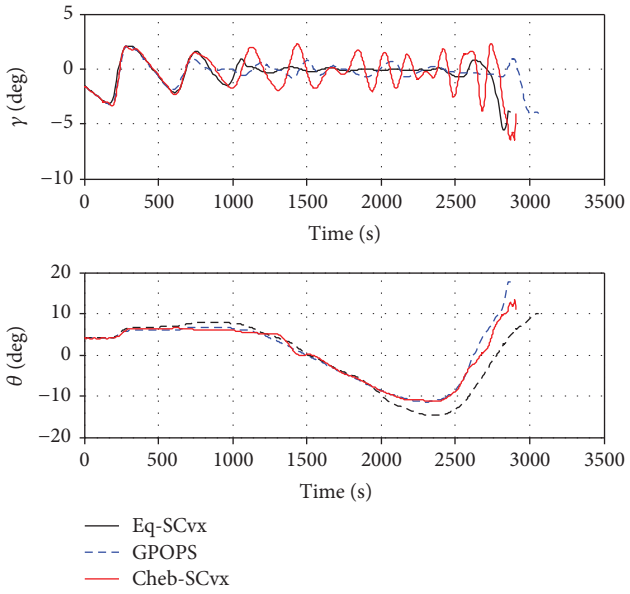

Figure 4: Flight path angle and heading angle histories.

The ground track of CAV constrained by NFZs is presented in Figure 2, which reveals that both target and NFZ constraints are satisfied by three methods. However, the proposed method renders lower cost than the other two methods do. Altitude and velocity profiles are given in Figure 3, while the flight path angle and heading angle histories are illustrated in Figure 4. Although the terminal altitude, velocity, and heading angle are not assigned a fixed value but limited in a prescribed range, the overall trend of the solutions provided by the three methods is similar. The optimized control variables' histories are presented in Figure 5, which shows that the bank angles obtained by the Cheb-SCvx method are with a more chattering phenomenon than those obtained

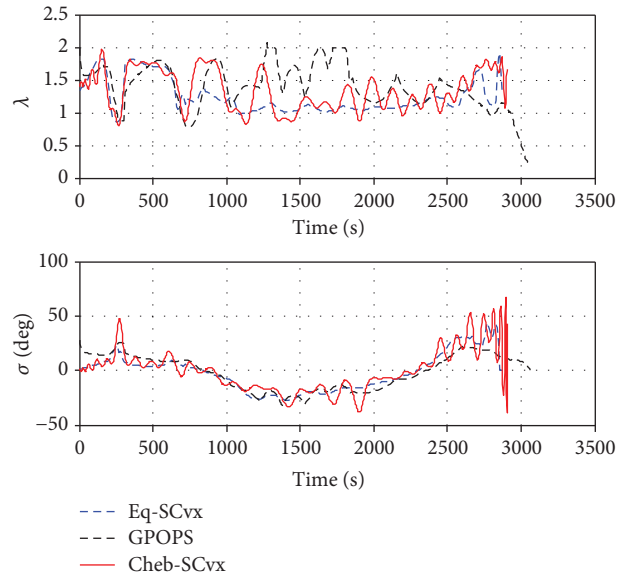

Figure 5: Control variables (normalized lift coefficient and bank angle) histories.

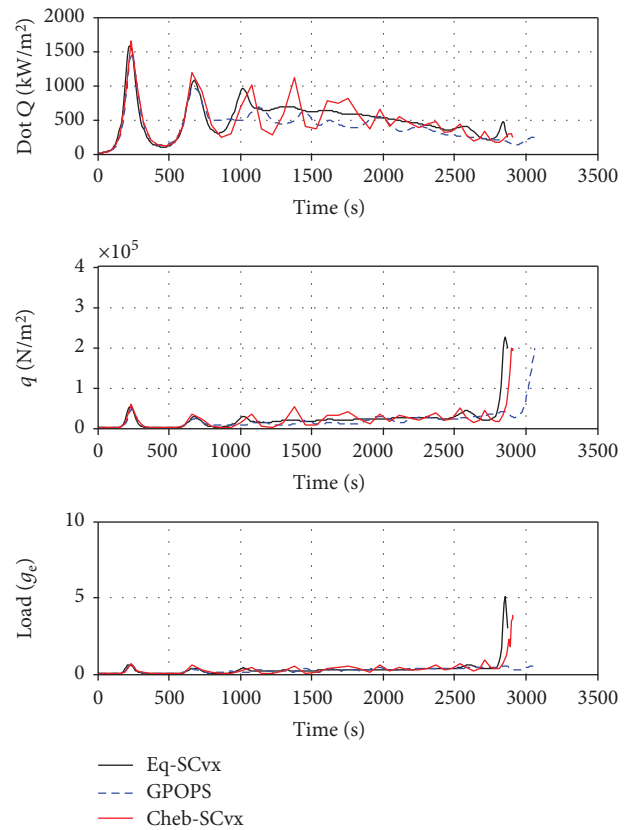

Figure 6: Heat flux, dynamic pressure, and normal load histories.

by the other methods during the final phase, but the constraints on the bank angle are well satisfied. Further, the constraints on the heat rate, dynamic pressure, and normal load are all satisfied (as shown in Figure 6).

5. Conclusions

Inspired by the application of convex optimization in aerospace trajectory generation and optimization, a novel sequential convex programming algorithm based on the classical Chebyshev pseudospectral method is proposed to solve a highly constrained entry trajectory optimization problem with free final time. By using sequential linearization, convexification, and discretization on the CGL node points, the original concave optimization problem is approximated by a series of SOCP problems, which are solved by open-source solver ECOS. In this work, we concentrate on the conversion of a nonconvex problem to a convex space, so that the converted problem can be efficiently solved by the SOCP method. An efficient and accurate discretization method based on the Chebyshev interpolating polynomials are proposed to facilitate transcribing the dynamic constraint into an algebraic equality constraint; then, the convexification technique based on the linearization is used to set up the convex version of the original trajectory optimization problem. The numeric results reveal that the proposed method can dramatically reduce computational cost by appropriately choosing the number of discretized points and will be very competitive to fulfill the onboard optimization in the future.

Data Availability

The data used to support the findings of this study are available from the corresponding author upon request.

Conflicts of Interest

The authors declare that there is no conflict of interest regarding the publication of this paper.

Acknowledgments

This work was supported in part by the National Key R&D Program of China (Grant No. 2018YFC0810202).

References

[1] A. V. Rao, "A survey of numerical methods for optimal control," *Advances in the Astronautical Sciences*, vol. 135, pp. 1–32, 2010.

[2] L. S. Pontryagin, V. G. Boltyanskii, R. V. Gamkrelidze, and E. F. Mishchenko, *The Mathematical Theory of Optimal Processes*, Interscience, New York, 1962.

[3] J. T. Betts, "Very low-thrust trajectory optimization using a direct SQP method," *Journal of Computational and Applied Mathematics*, vol. 120, no. 1-2, pp. 27–40, 2000.

[4] D. Garg, M. Patterson, C. Darby et al., "Direct trajectory optimization and costate estimation of general optimal control problems using a Radau pseudospectral method," in *Proceedings of the AIAA Guidance, Navigation, and Control Conference and Exhibit*, Chicago, Illinois, 2009.

[5] G. T. Huntington, "Advancement and analysis of a gauss pseudospectral transcription for optimal control problems," Ph.D dissertation, Massachusetts institute of Technology, 2007.

[6] B. Açıkmeşe and S. R. Ploen, "Convex programming approach to powered descent guidance for Mars landing," *Journal of Guidance, Control, and Dynamics*, vol. 30, no. 5, pp. 1353–1366, 2007.

[7] D.-J. Zhao and Z.-Y. Song, "Reentry trajectory optimization with waypoint and no-fly zone constraints using multiphase convex programming," *Acta Astronautica*, vol. 137, pp. 60–69, 2017.

[8] L. Blackmore, B. Acikmese, and D. P. Scharf, "Minimum-landing-error powered-descent guidance for Mars landing using convex optimization," *Journal of Guidance, Control, and Dynamics*, vol. 33, no. 4, pp. 1161–1171, 2010.

[9] D. Dueri, B. Açıkmeşe, D. P. Scharf, and M. W. Harris, "Customized real-time interior-point methods for onboard powered-descent guidance," *Journal of Guidance, Control, and Dynamics*, vol. 40, no. 2, pp. 197–212, 2017.

[10] X. Liu and P. Lu, "Solving nonconvex optimal control problems by convex optimization," *Journal of Guidance, Control, and Dynamics*, vol. 37, no. 3, pp. 750–765, 2014.

[11] X. Liu, Z. Shen, and P. Lu, "Entry trajectory optimization by second-order cone programming," *Journal of Guidance, Control, and Dynamics*, vol. 39, no. 2, pp. 227–241, 2016, Articles in advance.

[12] F. Fahroo and I. M. Ross, "Direct trajectory optimization by a Chebyshev pseudospectral method," *Journal of Guidance, Control, and Dynamics*, vol. 25, no. 1, pp. 160–166, 2002.

[13] S. Shahmirzaee Jeshvaghani, A. B. Novinzaddeh, and F. Pazooki, "Multiple stage satellite launch vehicle ascent optimization using Chebyshev wavelets," *Aerospace Science and Technology*, vol. 46, pp. 321–330, 2015.

[14] X. Wei, L. Liu, Y. Wang, and Y. Yang, "Reentry trajectory optimization for a hypersonic vehicle based on an improved adaptive fireworks algorithm," *International Journal of Aerospace Engineering*, vol. 2018, Article ID 8793908, 17 pages, 2018.

[15] G. N. Elnagar and M. A. Kazemi, "Pseudospectral Chebyshev optimal control of constrained nonlinear dynamical systems," *Computational Optimization and Applications*, vol. 11, no. 2, pp. 195–217, 1998.

[16] T. R. Jorris and R. G. Cobb, "Three-dimensional trajectory optimization satisfying waypoint and no-fly zone constraints," *Journal of Guidance, Control, and Dynamics*, vol. 32, no. 2, pp. 551–572, 2009.

[17] T. R. Jorris, "Common aero vehicle autonomous reentry trajectory optimization satisfying waypoint and no-fly zone constraints," Doctor, Engineering and Management, Air University, Ohio, US, 2007.

[18] X. Liu et al., "Exact convex relaxation for optimal flight of aerodynamically controlled missiles," *IEEE Transactions on Aerospace and Electronic Systems*, vol. 52, no. 4, pp. 1881–1892, 2016.

[19] J. Löfberg, "YALMIP : a toolbox for modeling and optimization in MATLAB," in *Proceedings of the CACSD Conference*, Taipei, Taiwan, 2004.

[20] A. Domahidi, E. Chu, and S. Boyd, "ECOS: an SOCP solver for embedded systems," in *European Control Conference*, Zurich, Switzerland, 2013.

Hindawi
International Journal of Aerospace Engineering
Volume 2019, Article ID 8939213, 8 pages
https://doi.org/10.1155/2019/8939213

Research Article

Cooperative Guidance of Seeker-Less Missiles for Precise Hit

Jianbo Zhao and Fenfen Xiong

School of Aerospace Engineering, Beijing Institute of Technology, Beijing 100081, China

Correspondence should be addressed to Jianbo Zhao; zhjb_cn@126.com

Received 18 October 2018; Revised 13 February 2019; Accepted 6 March 2019; Published 16 April 2019

Guest Editor: Manuel Soler

A novel cooperative guidance scenario is proposed that implements fire-and-forget attacks for seeker-less missiles with a cheap finder for stationary targets and without requiring real-time communication among missiles or precise position information. Within the proposed cooperative scenario, the classic leader-follower framework is utilized, and a two-stage cooperative guidance law is derived for the seeker-less missile. Linear-quadratic optimal control and biased proportional navigation guidance (PNG) are employed to develop this two-stage cooperative guidance law to minimize the control cost in the first stage and to reduce the maximum acceleration command in the second stage when the acceleration command is continuous. Simulations and comparisons are conducted that demonstrate the effectiveness and advantages of the proposed guidance law.

1. Introduction

Homing guidance systems that can implement fire-and-forget attacks have been rapidly developed and widely applied [1, 2]. In recent years, studies on homing guidance have dealt with constraints in the angle of impact [3], mostly through the employment of optimal control theory [4–13]. Moreover, constraints on the maximum acceleration command are also commonly considered [14, 15]. As is well-known, a seeker is essential to homing guidance systems, which is, however, very expensive. Therefore, it has become necessary to study guidance systems for seeker-less missiles.

Studies on the guidance of seeker-less missiles are mainly classified into two categories. The first category employs external guidance [1], whereby a ground station is utilized to control the trajectory of the seeker-less missile and to implement a precise hit [16, 17]. However, due to the involvement of a ground station, the fire-and-forget aspect of the missile attack cannot be implemented, and the position of the ground station is likely to be exposed. The other category is a scenario in which cooperative guidance is utilized, in which the seeker-less missile is guided by a separate missile with a seeker to hit the target [18, 19]. These two aforementioned cooperative guidance methods require real-time communication among the missiles and information on their precise position. It is well-known that the position of seeker-less missiles is commonly measured by the INS/GNSS (Inertial Navigation System and Global Navigation Satellite System), which inevitably induces localization errors. Moreover, real-time communication among missiles makes radio-silent attacks impossible, and the content of communications may be received and decoded by opponents, inducing difficulty for the defense penetration of missiles.

To address the aforementioned issues, a new cooperative guidance scenario is proposed to implement fire-and-forget attacks for seeker-less missiles without requiring real-time communication and precise position information. In this scenario, an onboard finder that is much cheaper than a seeker is employed for a seeker-less missile. Even though the measurement information produced by such a finder (the line-of-sight angle) is identical to that of the seeker, the finder has the following features that can clearly reduce costs, as the object of measurement would be another missile in the missile cluster: (1) the lock-on distance is remarkably reduced and (2) the requirements for identification capabilities are reduced, as information on the precise design of other missiles can be derived in advance, and there is no active disturbance or invisibility among these missiles. Therefore, this finder may be considered a cheaper version of a seeker, with a reduced lock-on distance and reduced requirements for

identification capabilities. To differentiate this device from commonly used seekers, this device will be defined in this paper as a "finder." Due to its features, a seeker-less missile with this finder will not be able to employ certain common laws of guidance, for a reduced lock-on distance and reduced identification capabilities for the finder would result in the target being undetectable.

Within this proposed cooperative guidance scenario, a missile with a seeker that can independently hit the target is located in the front of the missile cluster during the flight, while other seeker-less missiles equipped with finders can hit the target in sequence by tracking the position of the nearest missile at the front, including the missile with the seeker. In this scenario, the employment of the finder reduces costs, and the number of cooperative missiles may be conveniently increased, considering the reduced lock-on distance. In addition, to implement the aforementioned cooperative guidance scenario, a two-stage guidance law is designed for the seeker-less missile by employing linear-quadratic optimal control and biased proportional navigation guidance (PNG).

The remainder of this paper is organized as follows. In Section 2, the novel cooperative guidance scenario is introduced. In Section 3, the two-stage guidance law employing linear-quadratic optimal control and biased PNG is described for the implementation of the cooperative guidance scenario. In Section 4, the simulation results are presented and analyzed to verify the effectiveness and superiority of the proposed guidance law. Conclusions are drawn in the last section.

2. The Proposed Cooperative Guidance Scenario

Within the proposed cooperative guidance scenario (as shown in Figure 1), the classic leader-follower framework is employed, where n seeker-less missiles with finders are guided by a missile with a seeker (denoted as L) to cooperatively hit a stationary target. Considering the relatively short lock-on distance of the finder, the number of cooperative missiles, i.e., n, can be conveniently increased in this proposed cooperative guidance scenario. In Figure 1, only missile L is equipped with a seeker, and the seeker-less missile can easily implement a fire-and-forget attack by tracking the position of the nearest missile in front using its finder. In this work, for any two missiles with a tracking relationship, the tracked missile is considered as the leader and the tracking one the follower. Therefore, as shown in Figure 1, missile L is the leader of the missiles $F_1, F_2, \dots, F_n$, and missile F_1 is the leader of the missiles $F_{11}, F_{12}, \dots, F_{1n}$, etc.

In this cooperative guidance scenario, the missile L with the seeker could directly employ certain common guidance laws (e.g., PNG) to achieve an accurate hit, while the seeker-less missile can merely track its leader according to the information on relative motion derived by the finder. Considering that the finder of the follower missile will be ineffective if the lead missile has already hit its target, the law of guidance for seeker-less missiles is designed to be separated into two stages based on whether the leader has hit the target. Clearly, for the second stage of the seeker-less missile (i.e., its leader has hit the target), the initial relative motion between the target and seeker-less missile is derived by the finder with the assumption that the leader will finally arrive at the stationary target; thus, the seeker-less missile can implement certain common guidance laws (e.g., PNG) as the rate of change in the line-of-sight (LOS) angle for the target is derived in real time via the relative kinematic equations. Therefore, a precise hit by the seeker-less missile is achievable at the end of the second stage of guidance. Clearly, cooperative guidance between the seeker-less missile and its leader only exists during the first stage of guidance.

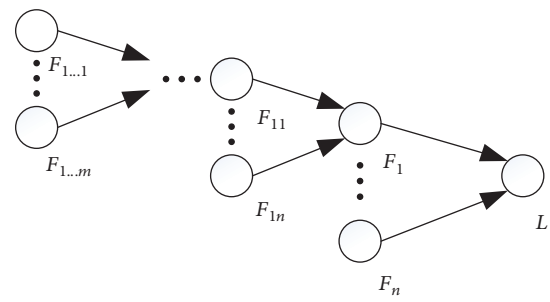

Figure 1: Proposed cooperative guidance scenario.

For the two-stage law of guidance for the seeker-less missile to be effective, any impact between the seeker-less missile and its leader must be avoided in the first stage, which will be studied later (Remark 2 of Section 3.2). In addition, during the first stage of guidance, the total cost of control for the seeker-less missile is minimized to save energy (as is commonly done in practice), while for the second stage of guidance, the maximum acceleration command is minimized in order to reduce requirements on the actuator.

3. Guidance Law Formulation

3.1. Model Linearization. Considering that the proposed cooperative guidance scenario consists of multiple groups with a leader-follower framework, a single leader-follower framework is first illustrated. During the first stage of a seeker-less missile (as a leader), its followers can be considered to be in the middle guidance stage, which is out of the scope of this work and thus not introduced here. Therefore, the missile L or only seeker-less missiles in the second stage are considered as leaders. The geometry between the leader M_l, follower M_i, and the target in the inertial reference coordinate X-O-Y is shown in Figure 2, in which the variables with the subscripts i and l, respectively, represent the states of the follower and leader in motion. Moreover, V, a, θ, q, and r denote the speed, normal acceleration, heading angle, LOS angle, and LOS distance, respectively.

The speed of all missiles is considered to be constant in this work, and the relative kinematic equations between the leader and follower are given as follows:

$$\dot{r}_i = -V_i \cos(q_i - \theta_i) + V_l \cos(q_i - \theta_l), \tag{1}$$

$$r_i \dot{q}_i = V_i \sin(q_i - \theta_i) - V_l \sin(q_i - \theta_l), \tag{2}$$

$$\eta_i = \theta_i - q_i, \tag{3}$$

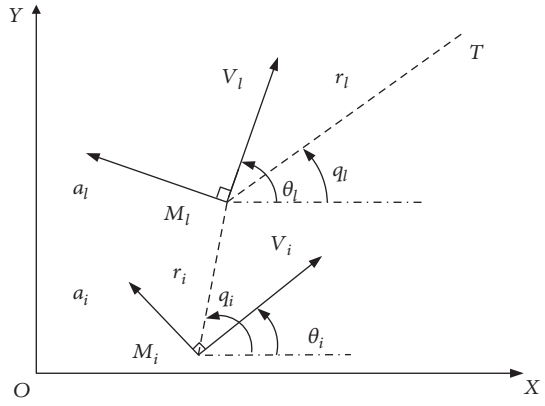

Figure 2: Geometry among the leader, follower, and target.

where η denotes the lead angle. The normal acceleration command of the follower is given as

$$a_i = V_i \dot{\theta}_i. \tag{4}$$

We define the error between the position coordinate for the leader and follower relative to the y-axis as y_i; thus,

$$\dot{y}_i = V_l \sin \theta_l - V_i \sin \theta_i. \tag{5}$$

To simplify the derivation of the guidance law, a linearization process is implemented. We approximate that there is no normal acceleration for the leader, as will be illustrated in Section 3.3. We also assume that θ_i is sufficiently small [20]. The reason is that for the leader implements the rectilinear motion and the x-axis of the employed inertial reference coordinate is defined as being approximately along the motion direction of the leader; the heading angle of the leader is small. Moreover, the heading angle of the follower would be essentially identical to that of the leader, as the terminal guidance for a maneuvering target commonly ends up in a tail-chase situation and the tracking target for the follower is the leader in this work. Therefore, the heading angle of the follower (θ_i) can be regarded as sufficiently small. The derivative of equation (5) is taken to be

$$\ddot{y}_i = -a_i. \tag{6}$$

As the leader flies straight, it is assumed without loss of generality that $\theta_l = 0$. The state vector is defined as

$$X = [y_i, \dot{y}_i, \theta_i]. \tag{7}$$

Therefore, the linearized guidance model can be derived as

$$\dot{X} = AX + Bu, \tag{8}$$

where

$$A = \begin{bmatrix} 0 & 1 & 0 \\ 0 & 0 & 0 \\ 0 & 0 & 0 \end{bmatrix},$$
$$B = \begin{bmatrix} 0 \\ -1 \\ 1/V_i \end{bmatrix}, \tag{9}$$
$$u = a_i.$$

3.2. Optimal Control Problem. As the follower only requires the employment of the common guidance law in the second stage, it is assumed that the PNG is utilized without loss of generality. Therefore, for the first stage of guidance, the following cost function is introduced to reduce the maximum acceleration for the second stage (the first term) and to minimize the control effort (the second term).

$$J = \frac{w}{2} \eta_i^2(t_{\mathrm{lf}}) + \frac{b}{2} \int_{t_0}^{t_{\mathrm{fl}}} u^2(t) dt, \tag{10}$$

where b is a positive constant and t_0 and t_{fl} denote the status at the initial and terminal instant of time, respectively, for the first stage of guidance. The constant w is defined as

$$w = \frac{c N_i^2 V_i^4}{r_i^2(t_{\mathrm{lf}})}, \tag{11}$$

where c is a positive constant and N_i is the navigation gain of follower M_i during the second stage of guidance. An explanation for the choice of w will be provided as the 2nd point of Remark 2.

As q_i is assumed to be sufficiently small, it can be approximated as

$$q_i = \frac{y_i}{r_i}. \tag{12}$$

Therefore, according to equation (3), the lead angle of the follower η_i can be formulated as

$$\eta_i = \theta_i - \frac{y_i}{r_i}. \tag{13}$$

Substituting equation (13) into equation (10) yields

$$J = \frac{w}{2} \left(\theta_i - \frac{y_i}{r_i} \right)^2 \Bigg|_{t=t_{\mathrm{fl}}} + \frac{b}{2} \int_{t_0}^{t_{\mathrm{fl}}} u^2(t) dt. \tag{14}$$

Then, the cost function shown in equation (14) can be classically reformulated as

$$J = \frac{1}{2} X^T(t_{\mathrm{lf}}) P(t_{\mathrm{lf}}) X(t_{\mathrm{lf}}) + \frac{1}{2} \int_{t_0}^{t_{\mathrm{fl}}} u^T(t) b u(t) dt, \tag{15}$$

where

$$P = \begin{bmatrix} [P_{11}]_{1\times1} & [P_{12}]_{1\times2} \\ [P_{12}{}^T]_{2\times1} & [P_{22}]_{2\times2} \end{bmatrix}, \quad P_{11} = w/r_i^2, P_{12} = [0 - w/r_i], P_{22} = \begin{bmatrix} 0 & 0 \\ 0 & w \end{bmatrix}. \tag{16}$$

It is well-known that the solution of the optimal control problem formulated by equations (8) and (15) is

$$u = -\frac{B^T K(t) X(t)}{b}, \tag{17}$$

where $K(t)$ is derived by numerically solving the associated differential matrix Riccati equation formulated as

$$\dot{K} = -KA - A^T K + \frac{KBB^T K}{b}, \quad K(t_{\mathrm{fl}}) = P. \tag{18}$$

The matrixes A, B, and $K(t)$ can be reformulated as

$$A = \begin{bmatrix} [0]_{1\times1} & [A_{12}]_{1\times2} \\ [0]_{2\times1} & [0]_{2\times2} \end{bmatrix}, \quad A_{12} = [\,1 \quad 0\,], \tag{19}$$

$$B = \begin{bmatrix} [0]_{1\times1} \\ [B_{21}]_{2\times1} \end{bmatrix}, \quad B_{21} = \begin{bmatrix} -1 \\ \dfrac{1}{V_i} \end{bmatrix}, \tag{20}$$

$$K = \begin{bmatrix} [K_{11}]_{1\times1} & [K_{12}]_{1\times2} \\ [K_{12}{}^T]_{2\times1} & [K_{22}]_{2\times2} \end{bmatrix}. \tag{21}$$

Substituting equations (19), (20), and (21) into equation (18) yields

$$\begin{aligned} &\dot{K}_{11} = K_{12} S K_{12}{}^T, \quad K_{11}(t_{\mathrm{lf}}) = P_{11}, \\ &\dot{K}_{12} = -K_{11} A_{12} + K_{12} S K_{22}, \quad K_{12}(t_{\mathrm{lf}}) = P_{12}, \\ &\dot{K}_{22} = -K_{12}{}^T A_{12} - A_{12}{}^T K_{12} + K_{22} S K_{22}, \quad K_{22}(t_{\mathrm{lf}}) = P_{22}, \end{aligned} \tag{22}$$

where S is defined as $B_{21}B_{21}^T/b$.

Therefore, equation (17) can be rewritten as

$$u = -\frac{B_{21}{}^T \left[K_{12}{}^T(t, t_{\mathrm{lf}}), K_{22}(t, t_{\mathrm{lf}})\right] X(t)}{b}. \tag{23}$$

Remark 1. $r_i(t_{\mathrm{lf}})$ must be predetermined to calculate $P(t_{\mathrm{lf}})$. Assuming that q_i and θ_i are sufficiently small and that $\theta_l = 0$, it can be approximated that the follower flies along the straight-line trajectory of the leader. Therefore, $r_i(t_{\mathrm{lf}})$ can be estimated by

$$r_i(t_{\mathrm{lf}}) = r_i(t_0) - (V_i - V_l)(t_{\mathrm{fl}} - t_0), \tag{24}$$

where $r_i(t_0)$ is derived by the finder at the initial time.

If the leader is the missile L, and by employing PNG, t_{fl} can be directly derived by the existing approach as [21]

$$t_{\mathrm{fl}} = \frac{r_l(t_0)}{V_l}\left(1 + \frac{\eta_l^2(t_0)}{2(2N_l - 1)}\right) + t_0, \tag{25}$$

where N_l is the navigation gain of missile L. Moreover, the initial distance between the missile L and the target $r_L(t_0)$ can be derived [3]. If the leader is a seeker-less missile (e.g., the missile F_1), t_{fl} can be approximately derived as

$$t_{\mathrm{fl}} = \frac{r_L(t_0) + r_{F_1}(t_0)}{V_{F_1}}, \tag{26}$$

where V_{F_1} is the velocity of missile F_1 and $r_{F_1}(t_0)$ is the initial distance between the missile L and F_1. Similarly, if the leader is the seeker-less missile F_{11}, equation (26) can be rephrased as

$$t_{\mathrm{fl}} = \frac{\left(r_L(t_0) + r_{F_1}(t_0)\right) + r_{F_{11}}(t_0)}{V_{F_{11}}}, \tag{27}$$

where $V_{F_{11}}$ and $r_{F_{11}}(t_0)$ are the velocity of missile F_{11} and the initial distance between missiles F_1 and F_{11}, respectively. Therefore, a follower is required to derive the distance between its leader and the target at the initial time.

Remark 2. The three criteria for the guidance mentioned in Section 2 can be satisfied.

(1) For the first stage of guidance, it can be derived from equation (24) that $\forall t \in [t_0, t_{\mathrm{fl}}]$,

$$\begin{aligned} &r_i(t) \geq r_i(t_0) - (V_i - V_l)(t_{\mathrm{fl}} - t_0), \quad \text{with } V_i \geq V_l, \\ &r_i(t) \geq r_i(t_0), \quad \text{with } V_i < V_l. \end{aligned} \tag{28}$$

Evidently, the impact between the leader and follower is avoided with the condition $V_i < V_l$. Moreover, when $V_i \geq V_l$, an impact can also be avoided if $r_i(t_0)$ satisfies

$$r_i(t_0) \geq (V_i - V_l)(t_{\mathrm{fl}} - t_0). \tag{29}$$

In addition, by considering the limited lock-on distance of the finder, the upper limit of $r_i(t_0)$ which will be implemented during the middle guidance stage, can be derived, i.e.,

$$r_i(t_0) \le l_d, \quad \text{with } V_i \ge V_l,$$
$$r_i(t_0) \le l_d - (V_l - V_i)(t_{\mathrm{fl}} - t_0), \quad \text{with } V_i < V_l, \tag{30}$$

where l_d denotes the lock-on distance of the finder.

(2) Because the follower can employ the PNG during the second stage of guidance, i.e.,

$$a_i = N_i V_i \dot{q}_i. \tag{31}$$

Substituting equation (2) into equation (31) yields

$$a_i = \frac{N_i V_i [V_i \sin(q_i - \theta_i) - V_l \sin(q_i - \theta_l)]}{r_i}. \tag{32}$$

Since $V_l = 0$ in the second stage, equation (32) can be rephrased as

$$a_i = -\frac{N_i {V_i}^2 \sin \eta_i}{r_i}. \tag{33}$$

As the initial acceleration of the PNG is at a maximum, the term $(w/2)\eta_i^2(t_{\mathrm{fl}})$ employed in equation (10) can reduce the maximum acceleration for the second stage ($|a_i(t_{\mathrm{fl}})|$).

(3) The total control cost for the first stage can be optimized by considering the term $(b/2)\int_{t_0}^{t_{\mathrm{fl}}} u^2(t)dt$ in equation (10).

3.3. Two-Stage Guidance. Clearly, it is more convenient to implement the guidance algorithm if it is reformulated with respect to variables that can be directly measured by onboard instruments. Therefore, an alternative measurable state vector for the acceleration command during the first stage is provided in this subsection. With the assumptions that $\theta_l = 0$ and θ_i is sufficiently small, equation (5) can be rephrased as

$$\dot{y}_i = -V_i \theta_i. \tag{34}$$

Moreover, because equation (12) is identical to

$$y_i = r_i q_i, \tag{35}$$

the state vector can be redefined as

$$Z = [\theta_i, q_i]^T, \tag{36}$$

and it can be derived that

$$X = WZ, \tag{37}$$

where

$$W = \begin{bmatrix} 0 & r_i \\ -V_i & 0 \\ 1 & 0 \end{bmatrix}. \tag{38}$$

Figure 3: The relationship between the missiles.

Table 1: Initial states of the missiles.

Parameters	L	F_1	F_2	F_3
Position, $\times 10^3$ m	(6, 1)	(5, 0.5)	(4, 0)	(3, 0.5)
Velocity, $\times 10^2$ m/s	3.5	3.7	3.7	3.7
Heading angle (deg)	10	0	0	0

Then, substituting equation (37) into equation (23) yields

$$u = -\frac{{B_{21}}^T \left[{K_{21}}^T(t, t_{\mathrm{fl}}), K_{22}(t, t_{\mathrm{fl}})\right] WZ(t)}{b}. \tag{39}$$

In the second stage of guidance, if the follower employs the PNG, the acceleration command would be discontinuous at the initial time, since

$$a_i({t_{\mathrm{lf}}}^-) \ne N_i V_i \dot{q}_i({t_{\mathrm{lf}}}^+), \tag{40}$$

where ${t_{\mathrm{lf}}}^+$ and ${t_{\mathrm{lf}}}^-$ represent the initial time of the second stage and the terminal time of the first stage, respectively. Therefore, a biased PNG is proposed for the seeker-less missile during the second stage, i.e.,

$$a_i = N_i V_i (\dot{q}_i(t) - \dot{q}_i({t_{\mathrm{lf}}}^+)h) + a_i({t_{\mathrm{lf}}}^-)h, \tag{41}$$

where

$$h = \frac{r_i(t)}{r_i(t_{\mathrm{lf}})}. \tag{42}$$

Both $\eta_i({t_{\mathrm{lf}}}^+)$ and $a_i({t_{\mathrm{lf}}}^-)$ are sufficiently small if optimal control is implemented in the first stage of guidance. Thus, $|\eta_i| < (\pi/2)$ can be guaranteed during the second stage of guidance. Thus, both r_i and h are monotonously decreasing during this stage, which further means that equation (41) will converge to the PNG, and the miss distance as well as the terminal acceleration command of the biased PNG could be identical to 0. Moreover, it is verified that the normal acceleration of the leader is approximately identical to 0 when the missile L and the seeker-less missile in the second stage employ the PNG and the biased PNG, respectively, with greater navigation gain.

4. Simulation and Analysis

In our analysis, three seeker-less missiles with finders, guided by a missile with a seeker, cooperatively hit a stationary target located at 12000 m and 1000 m. The measurement relationship between the missiles and their initial states of motion are presented in Figure 3 and Table 1, in which L represents the missile with the seeker, while F_1, F_2, and F_3 represent seeker-less missiles. The missile L employs the PNG, while

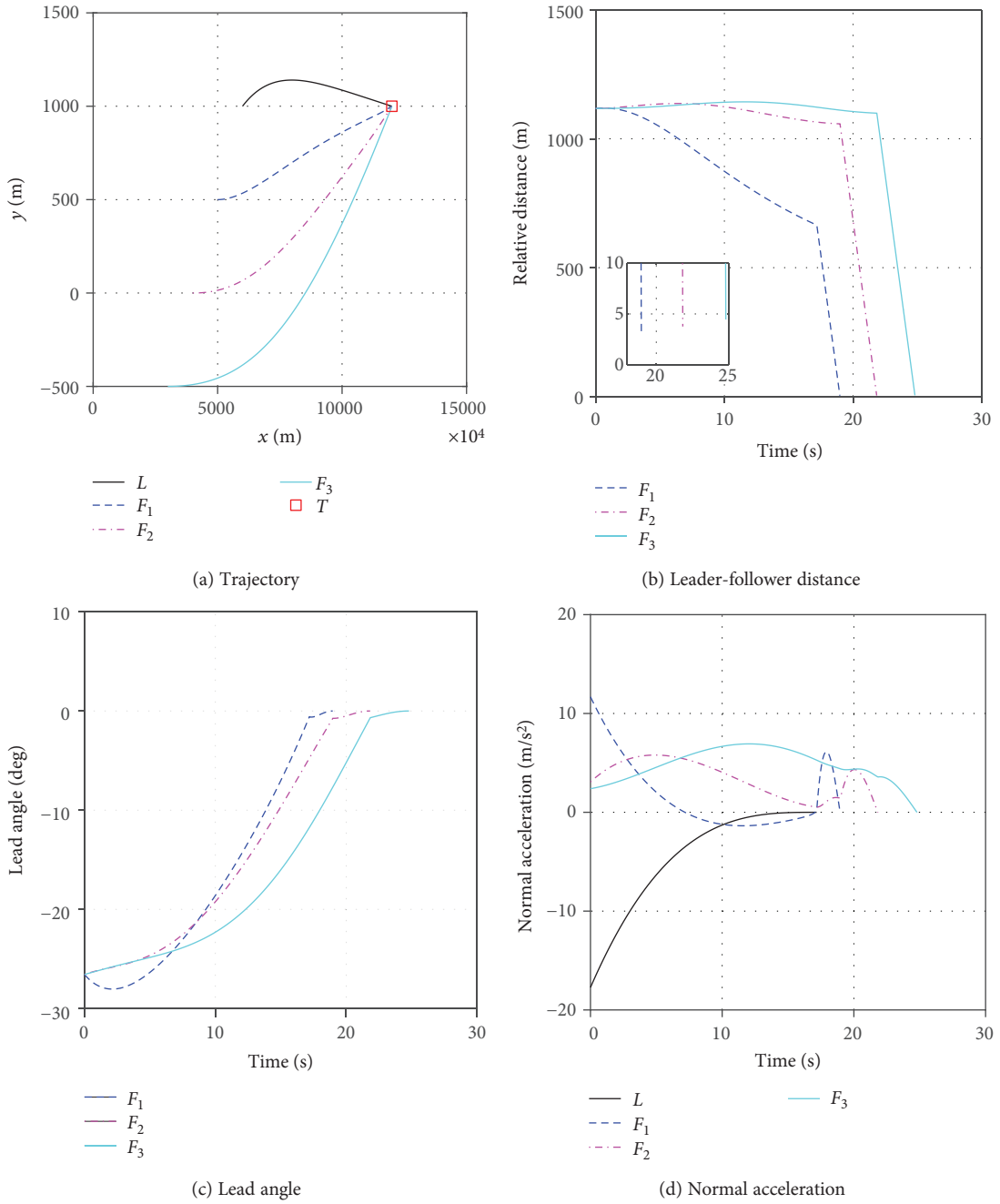

Figure 4: Simulation results for the proposed cooperative guidance law.

F_1, F_2, and F_3 all employ the proposed or modified (for comparison) two-stage guidance law during the entire flight. These two-stage guidance laws change to second stage if the leader is lost for follower. In Figure 3, two different cases are considered: (1) the leader is a missile with a seeker (for F_1) and (2) the leaders are seeker-less missiles with finders (for F_2 and F_3). To achieve a precise hit, the miss distance and normal acceleration command of these missiles and the relative distance between the leader and follower are required to be less than 5 m, 20 m/s^2, and 1200 m/s^2, respectively.

4.1. Sample Simulation. The simulation results for the proposed two-stage guidance law are presented in Figure 4. The trajectories of the four missiles are illustrated in Figure 4(a), which indicates that all seeker-less missiles that correspond to the two cases could precisely hit their targets when the two-stage guidance law is employed for follower missiles with the leader in the first stage. Figure 4(b) shows the leader-follower distance (missile-target distance during second guidance stage), in which it indicates that all the seeker-less missiles can satisfy requirements for miss distances and lock-on distances of finders with the proposed cooperative guidance law. Figure 4(c) illustrates that the lead angles between the seeker-less missiles and their leaders are essentially identical to 0 at the terminal time instant for the first stage of guidance. In other words, the maximum normal

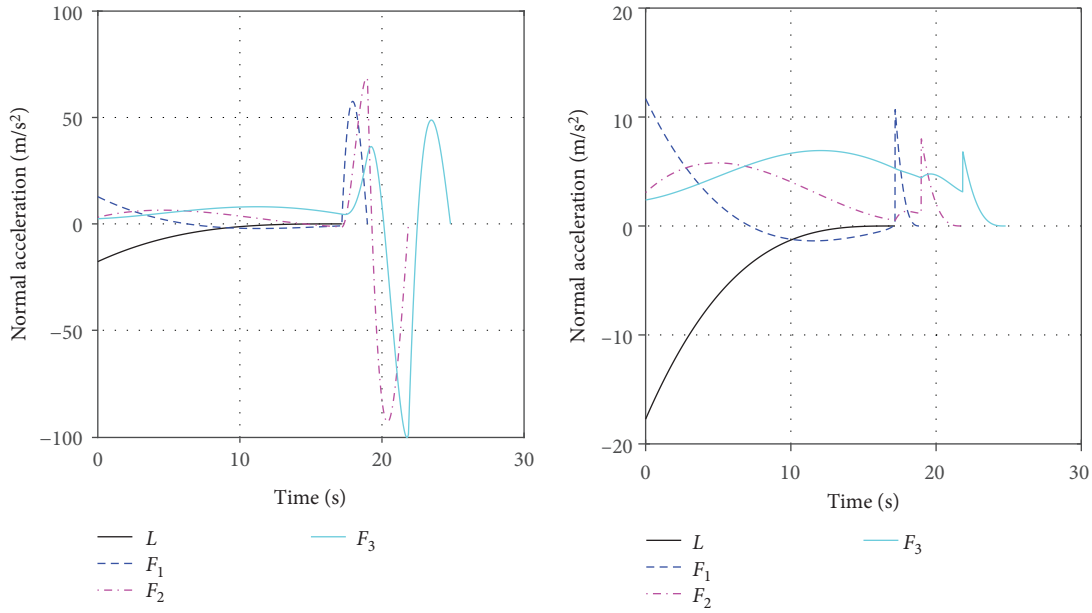

(a) 1st modified two-stage guidance law

(b) 2nd modified two-stage guidance law

Figure 5: Normal acceleration command for modified guidance laws.

acceleration of the seeker-less missile for the second stage of guidance can be reduced. In Figure 4(d), it is indicated that all the missiles can satisfy requirements for a normal acceleration command. Moreover, from Figures 4(b) and 4(d), it can be verified that the miss distance as well as the terminal acceleration command of the seeker-less missile could be identical to 0.

4.2. Comparison of Two Modified Two-Stage Guidance Laws. To verify the superiority of the proposed cost function for the first stage and the biased PNG for the second stage, two modified two-stage guidance laws using the existing formulations are introduced. For the first modified guidance law, the zero-effort miss distance is considered to produce an optimal state of initial motion for the second stage of guidance, as is commonly done in the literature; i.e., the cost function shown in equation (10) is rewritten as [22]

$$J = \frac{\varsigma}{2}\left[y_i(t_{\mathrm{fl}}) + \dot{y}_i(t_{\mathrm{fl}}) \cdot \Delta t\right]^2 + \frac{\zeta}{2}\int_{t_0}^{t_{\mathrm{fl}}} u^2(t)dt, \qquad (43)$$

where ς and ζ are positive constants and Δt denotes the error in flight time between the leader and follower, which is essentially identical to $(r_i(t_0))/V$. For the second modified guidance law, the existing PNG is utilized for the second guidance stage instead of the proposed biased PNG.

With the first or second modified two-stage guidance law, all the miss distances of F_1, F_2, and F_3 and the relative distances between leaders and followers would satisfy the requirement, which can be verified by the simulation. However, compared with the results shown in Figure 4(d) for the proposed method, Figure 5(a), derived by the existing method, indicates that for the first modified two-stage guidance law, the maximum normal acceleration of the seeker-less missile during the second stage of guidance is far greater and cannot satisfy the requirement. The reason is that, compared with the cost function introduced in equation (10), equation (43) cannot effectively reduce the maximum normal acceleration during the second stage of guidance. Moreover, by comparing Figures 4(d) and 5(b), it is observed that compared with the PNG, the seeker-less missile employing the proposed biased PNG can clearly obtain a continuous acceleration command and a smaller maximum acceleration during the second stage of guidance.

5. Conclusion

To achieve a precise hit of a seeker-less missile for a stationary target, a novel cooperative scenario for guidance is proposed in this work that is able to implement fire-and-forget attacks for seeker-less missiles without real-time communication or precise position information. Within the proposed novel cooperative guidance scenario, a two-stage cooperative guidance law is derived for a seeker-less missile. The guidance law for the first stage can produce the minimum control cost for this stage as well as the reduced maximum acceleration command for the second stage. The guidance law for the second stage can guarantee a precise hit for a seeker-less missile with a continuous acceleration command. Simulation results illustrate the effectiveness and superiority of the proposed two-stage guidance law.

Data Availability

The data used to support the findings of this study are included within the article.

Conflicts of Interest

The authors declare that there is no conflict of interest regarding the publication of this paper.

Acknowledgments

This work was supported by the National Science Foundation of China (grant number 11532002) and the Hongjian Innovation Foundation of China (grant number BQ203-HYJJ-Q2018002).

References

[1] G. M. Siouris, *Missile Guidance and Control Systems*, Springer-Verlag New York, Inc, 2004.

[2] J. ZHAO and S. YANG, "Integrated cooperative guidance framework and cooperative guidance law for multi-missile," *Chinese Journal of Aeronautics*, vol. 31, no. 3, pp. 546–555, 2018.

[3] N. Balhance, M. Weiss, and T. Shima, "Cooperative guidance law for intrasalvo tracking," *Journal of Guidance Control and Dynamics*, vol. 40, no. 6, pp. 1441–1456, 2017.

[4] R. Livermore and T. Shima, "Deviated pure-pursuit-based optimal guidance law for imposing intercept time and angle," *Journal of Guidance, Control, and Dynamics*, vol. 41, no. 8, pp. 1807–1814, 2018.

[5] S. F. Xiong, M. Y. Wei, M. Y. Zhao, H. Xiong, W. H. Wang, and B. C. Zhou, "Hyperbolic tangent function weighted optimal intercept angle guidance law," *Aerospace Science and Technology*, vol. 78, pp. 604–619, 2018.

[6] H. Q. Zhang, S. J. Tang, J. Guo, and W. Zhang, "A two-phased guidance law for impact angle control with seeker's field-of-view limit," *International Journal of Aerospace Engineering*, vol. 2018, Article ID 7403639, 13 pages, 2018.

[7] J. H. Liu, J. Y. Shan, and Q. Liu, "Optimal pulsed guidance law with terminal impact angle constraint," *Proceedings of the Institution of Mechanical Engineers, Part G: Journal of Aerospace Engineering*, vol. 231, no. 11, pp. 1993–2005, 2017.

[8] K. S. Erer and R. Tekin, "Impact time and angle control based on constrained optimal solutions," *Journal of Guidance Control and Dynamics*, vol. 39, no. 10, pp. 2448–2454, 2016.

[9] B. G. Park, T. H. Kim, and M. J. Tahk, "Range-to-go weighted optimal guidance with impact angle constraint and seeker's look angle limits," *IEEE Transactions on Aerospace and Electronic Systems*, vol. 52, no. 3, pp. 1241–1256, 2016.

[10] R. Tsalik and T. Shima, "Optimal guidance around circular trajectories for impact-angle interception," *Journal of Guidance, Control, and Dynamics*, vol. 39, no. 6, pp. 1278–1291, 2016.

[11] C. H. Lee, J. I. Lee, and M. J. Tahk, "Sinusoidal function weighted optimal guidance laws," *Proceedings of the Institution of Mechanical Engineers, Part G: Journal of Aerospace Engineering*, vol. 229, no. 3, pp. 534–542, 2015.

[12] Y. Zhao, J. B. Chen, and Y. Z. Sheng, "Terminal impact angle constrained guidance laws using state-dependent Riccati equation approach," *Proceedings of the Institution of Mechanical Engineers, Part G: Journal of Aerospace Engineering*, vol. 229, no. 9, pp. 1616–1630, 2015.

[13] A. Maity, H. B. Oza, and R. Padhi, "Generalized model predictive static programming and angle-constrained guidance of air-to-ground missiles," *Journal of Guidance, Control, and Dynamics*, vol. 37, no. 6, pp. 1897–1913, 2014.

[14] C. H. Lee, T. H. Kim, M. J. Tahk, and I. H. Whang, "Polynomial guidance laws considering terminal impact angle and acceleration constraints," *IEEE Transactions on Aerospace and Electronic Systems*, vol. 49, no. 1, pp. 74–92, 2013.

[15] R. Tekin and K. S. Erer, "Switched-gain guidance for impact angle control under physical constraints," *Journal of Guidance, Control, and Dynamics*, vol. 38, no. 2, pp. 205–216, 2015.

[16] G. S. Kumar, R. Ghosh, D. Ghose, and A. Vengadarajan, "Guidance of seekerless interceptors using innovation covariance based tuning of Kalman filters," *Journal of Guidance, Control, and Dynamics*, vol. 40, no. 3, pp. 603–614, 2017.

[17] G. S. Kumar, D. Ghose, and A. Vengadarajan, "An integrated estimation/guidance approach for seeker-less interceptors," *Proceedings of the Institution of Mechanical Engineers, Part G: Journal of Aerospace Engineering*, vol. 229, no. 5, pp. 891–905, 2015.

[18] Q. L. Zhao, J. Chen, X. W. Dong, Q. D. Li, and Z. Ren, "Cooperative guidance law for heterogeneous missiles intercepting hypersonic weapon," *Acta Aeronautica et Astronautica Sinica*, vol. 37, no. 3, pp. 936–948, 2016.

[19] E. Zhao, S. Wang, T. Chao, and M. Yang, "Multiple missiles cooperative guidance based on leader-follower strategy," *Proceedings of 2014 IEEE Chinese Guidance, Navigation and Control Conference*, 2014, pp. 1163–1167, Yantai, China, 2014.

[20] C. K. Ryoo, H. J. Cho, and M. J. Tahk, "Optimal guidance laws with terminal impact angle constraint," *Journal of Guidance, Control, and Dynamics*, vol. 28, no. 4, pp. 724–732, 2005.

[21] I. S. Jeon, J. I. Lee, and M. J. Tahk, "Homing guidance law for cooperative attack of multiple missiles," *Journal of Guidance, Control, and Dynamics*, vol. 33, no. 1, pp. 275–280, 2010.

[22] P. Zarchan, *Tactical and Strategic Missile Guidance*, VA: AIAA, 6th edition, 2012.

Hindawi
International Journal of Aerospace Engineering
Volume 2019, Article ID 7980379, 12 pages
https://doi.org/10.1155/2019/7980379

Research Article

Evasion-Pursuit Strategy against Defended Aircraft Based on Differential Game Theory

Qilong Sun,[1] **Minghui Shen**,[1] **Xiaolong Gu**,[1] **Kang Hou**,[1] **and Naiming Qi**[2]

[1]*Beijing Institute of Space Long March Vehicle, Beijing 100076, China*
[2]*Harbin Institute of Technology, Harbin 100050, China*

Correspondence should be addressed to Qilong Sun; sunqilong27@163.com

Received 16 October 2018; Accepted 15 January 2019; Published 12 March 2019

Guest Editor: Ernesto Staffetti

The active defense scenario in which the attacker evades from the defender and pursues the target is investigated. In this scenario, the target evades from the attacker, and the defender intercepts the attacker by using the optimal strategies. The evasion and the pursuit boundaries are investigated for the attacker when the three players use the one-to-one optimal guidance laws, which are derived based on differential game theory. It is difficult for the attacker to accomplish the task by using the one-to-one optimal guidance law; thus, a new guidance law is derived. Unlike other papers, in this paper, the accelerations of the target and the defender are unknown to the attacker. The new strategy is derived by linearizing the model along the initial line of sight, and it is obtained based on the open-loop solution form as the closed-loop problem is hard to solve. The results of the guidance performance for the derived guidance law are presented by numerical simulations, and it shows that the attacker can evade the defender and intercept the target successfully by using the proposed strategy.

1. Introduction

In the traditional pursuit-evasion scenario, the guidance law was investigated for two players which included an evasion target and a pursuit attacker. Zarchan studied a variety of guidance laws for this pursuit-evasion scenario [1]. A new impact time and angle control guidance law against stationary and nonmaneuvering targets was investigated for the missile [2]. A novel extended proportional guidance law was designed to intercept the maneuvering target [3]. The adaptive integral sliding mode guidance law was derived in a three-dimensional scenario [4, 5]. In these papers, the acceleration of the target was a known bounded external disturbance to the missile. A two-phase optimal guidance law was derived to improve the estimation accuracy and terminal performances for impact angle constraint engagement [6]. Yang et al. [7] presented a time-varying biased proportional guidance law in which two time-varying bias terms were applied to divide the trajectory into the initial phase and terminal phase. Recently, various pursuit-evasion scenarios involving multiple players have been investigated. The guidance laws for two missiles attacking one target were analyzed [8, 9]. References [10–12] described a scenario in which multimissiles attacked one target, and the cooperative guidance laws were derived.

When a missile attacks the aircraft, the aircraft always launches a defender to protect itself. Meanwhile, the aircraft evades the attacking missile. The problem which includes a target aircraft, a defender, and an attacking missile is known as the active defense scenario. It is difficult for a missile to hit the aircraft that launched a defender by using the traditional guidance law. The three-player engagement is different from the typical one-to-one engagement. In recent years, the strategies in the active defense scenario have been a hot topic, and especially, the cooperative guidance laws between the target and the defender have been studied a lot.

A scenario in which the defender and the fixed or slowly moving target constituted the defended system was investigated [13–15]. In these papers, the optimal defense guidance laws were derived under the condition that the positions and the trajectories of the target and the attacker were known to the defender. Rusnak [16] investigated a scenario in which

the lady evaded from the bandit that pursued the lady and the body guard intercepted the bandit before the bandit captured the lady. In this paper, the optimal strategies were derived base on the differential game theory and optimal control theory. Line of sight (LOS) guidance law was investigated to intercept the attacker and protect the target [17]. In this paper, the defender is located on the line of sight of the attacker and the target. The defender could intercept the attacker with less control by using the LOS guidance law than by using the traditional guidance law. The cooperative optimal guidance laws between the target and the defender were studied [18–20]. In these papers, the target launched one defender, and the guidance laws were derived by differential game theory. The defender and the target helped each other to intercept the attacker. Oyler et al. [21] studied the pursuit-evasion games in the presence of obstacles that inhibited the motions of the players. The dominance regions were presented and analyzed to provide a complete solution to the game. Unlike previous research, two defenders were launched from the target to protect itself [22, 23]. In Reference [23], the cooperation between the defenders and the target was one-way which meant one defender received the information from the target and another defender sent information to the target. In Refs. [24–26], the cooperative guidance law for protecting the target was investigated by using nonlinear methods, and the defender could intercept the attacker with high heading angle errors. The conditions were investigated for the attacker winning the game in the active defense scenario by using the differential game theory [27]. Rubinsky and Gutman [28] investigated a three-player scenario in which the attacker evaded a defender and continued to pursue a target. In this scenario, the target and defender were independent, and the derived guidance law is only suited for the condition that the zero-effort-miss (ZEM) distance between the attacker and the target is not a large value. An evasion and pursuit guidance law for the attacking missile was analyzed [29], and the control efforts of the defender and the target were known to the attacking missile. In this paper, the attacking missile chose an appropriate lateral acceleration to maneuver before the defender and the attacking missile met, then the attacking missile used the optimal pursuit guidance law to hit the aircraft.

In the previous paper, the studies always focused on the cooperative guidance law between the aircraft and the defender. However, the attacking guidance law for the attacker winning the game is relatively rare. Refs. [27–29] presented the attacking guidance laws for the attacking missile. However, in these papers, the control efforts of the target and the defender were known to the missile, and they were hard to obtain in reality. The method presented in Reference [28] is unsuited for the condition that the zero-effort-miss (ZEM) distance between the attacker and the target is large, and the zero-effort-miss (ZEM) distance between the attacker and the defender is small.

In this paper, a new strategy is investigated for the attacker to hit the target. In this scenario, the miss distance between the target and the attacker and the miss distance between the defender and the attacker are considered for the attacker at the same time. The target and the defender are independent, and they use the optimal strategies. It is not necessary for the attacker to obtain the control efforts of the target and the defender by using the derived guidance law.

2. Problem Formulation

The problem consists of three players: an attacker (A), a target (T), and a defender (D), and the scenario is described in Figure 1. LOS is the line of sight. R and V represent the range and velocity. γ represents the flight path angle. λ represents the angle between line of sight and the X axis. The lateral acceleration is denoted by α. The subscripts A, T, and D represent the corresponding players. AT and AD present the corresponding parameters between the players.

Neglecting the gravitational force, the geometric relations for the rates of the ranges are obtained by

$$\begin{aligned} \dot{R}_{\mathrm{AT}} &= V_{\mathrm{A}} \cos(\gamma_{\mathrm{A}} - \lambda_{\mathrm{AT}}) + V_{\mathrm{T}} \cos(\gamma_{\mathrm{T}} + \lambda_{\mathrm{AT}}), \\ \dot{R}_{\mathrm{AD}} &= V_{\mathrm{A}} \cos(\gamma_{\mathrm{A}} - \lambda_{\mathrm{AD}}) + V_{\mathrm{D}} \cos(\gamma_{\mathrm{D}} + \lambda_{\mathrm{AD}}). \end{aligned} \tag{1}$$

The LOS rate relations are expressed as follows:

$$\begin{aligned} \dot{\lambda}_{\mathrm{AT}} &= \frac{V_{\mathrm{T}} \sin(\gamma_{\mathrm{T}} + \lambda_{\mathrm{AT}}) - V_{\mathrm{A}} \sin(\gamma_{\mathrm{A}} - \lambda_{\mathrm{AT}})}{R_{\mathrm{AT}}}, \\ \dot{\lambda}_{\mathrm{AD}} &= \frac{V_{\mathrm{D}} \sin(\gamma_{\mathrm{D}} + \lambda_{\mathrm{AD}}) - V_{\mathrm{A}} \sin(\gamma_{\mathrm{A}} - \lambda_{\mathrm{AD}})}{R_{\mathrm{AD}}}. \end{aligned} \tag{2}$$

The dynamics of each player are considered to be a linear time-invariant system that can be described by the following equations [24]:

$$\begin{aligned} \dot{\delta}^i_{n\times 1} &= \alpha^i_{n\times n}\delta^i_{n\times 1} + \beta^i_{n\times 1}u'_i, \quad i = \{\mathrm{A}, \mathrm{T}, \mathrm{D}\}, \\ \alpha_i K^i_{1\times n}\delta^i_{n\times 1} &+ d_i u'_i, \quad i = \{\mathrm{A}, \mathrm{T}, \mathrm{D}\}. \end{aligned} \tag{3}$$

Here, δ_i is the state vector of internal state variables of each agent with dim $(\delta_i) = n_i$, and u'_i represents its controller.

The path angle relations satisfy the following equation:

$$\dot{\gamma}_i = \frac{a_i}{V_i}, \quad i = \{\mathrm{A}, \mathrm{T}, \mathrm{D}\}. \tag{4}$$

It is assumed that the problem occurs in the endgame phase and the defender separates from the target; thus, the problem can be linearized along the initial lines of sight. The relative displacement between two players normal to LOS_0 is denoted as $y_i\{i = \mathrm{AT}, \mathrm{AD}\}$. The accelerations of the attacker and target normal to $\mathrm{LOS}_{\mathrm{AT}}$ are denoted by $u_{\mathrm{AL}_{\mathrm{AT}}}$ and $u_{\mathrm{TL}_{\mathrm{AT}}}$. The acceleration of the defender normal to $\mathrm{LOS}_{\mathrm{AD}}$ is defined by $u_{\mathrm{DL}_{\mathrm{AD}}}$.Thus, we can obtain

$$\begin{cases} \ddot{y}_{\mathrm{AT}} = u_{\mathrm{TL}_{\mathrm{AT}}} - u_{\mathrm{AL}_{\mathrm{AT}}}, \\ \ddot{y}_{\mathrm{AD}} = u_{\mathrm{DL}_{\mathrm{AD}}}\boldsymbol{\Gamma}(t) - \kappa u_{\mathrm{AL}_{\mathrm{AT}}}, \end{cases} \tag{5}$$

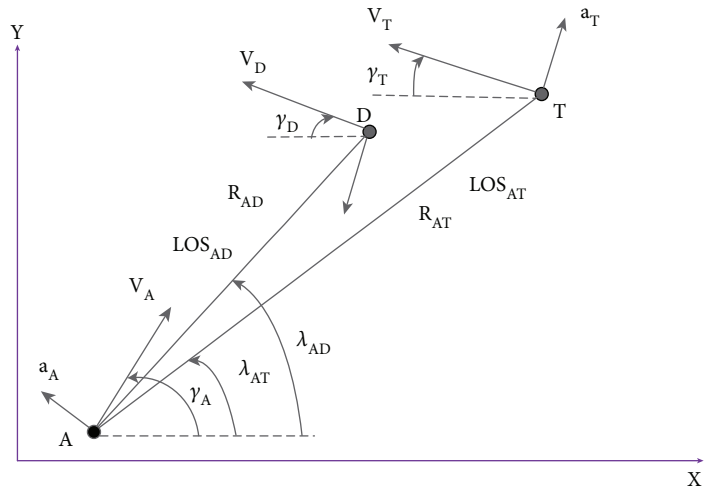

Figure 1: Engagement geometry.

where

$$\begin{cases} u_{\mathrm{AL}_{\mathrm{AT}}} = a_{\mathrm{A}} \cos(\gamma_{\mathrm{A}} - \lambda_{\mathrm{AT}}) = \left(K^{\mathrm{A}}_{1\times n} x_{\mathrm{A}} + d_{\mathrm{A}} u'_{\mathrm{A}}\right) \cos(\gamma_{\mathrm{A}} - \lambda_{\mathrm{AT}}), \\ u_{\mathrm{TL}_{\mathrm{AT}}} = a_{\mathrm{T}} \cos(\gamma_{\mathrm{T}} + \lambda_{\mathrm{AT}}) = \left(K^{\mathrm{T}}_{1\times n} x_{\mathrm{T}} + d_{\mathrm{T}} u'_{\mathrm{T}}\right) \cos(\gamma_{\mathrm{T}} - \lambda_{\mathrm{AT}}), \\ u_{\mathrm{DL}_{\mathrm{AD}}} = a_{\mathrm{D}} \cos(\gamma_{\mathrm{D}} + \lambda_{\mathrm{AD}}) = \left(K^{\mathrm{D}}_{1\times n} x_{\mathrm{D}} + d_{\mathrm{A}} u'_{\mathrm{D}}\right) \cos(\gamma_{\mathrm{D}} - \lambda_{\mathrm{AD}}), \end{cases}$$

$$\Gamma(t) = \begin{cases} 1, & t < t_f^{\mathrm{AD}}, \\ 0, & t \geq t_f^{\mathrm{AD}}, \end{cases}$$

$$\kappa = \frac{\cos(\gamma_{\mathrm{A}} - \lambda_{\mathrm{AD}})}{\cos(\gamma_{\mathrm{A}} - \lambda_{\mathrm{AT}})}. \tag{6}$$

We solve the problem under the condition that the players A, T, and D obey ideal dynamics. Thus, $a^i_{n\times n}$, $\beta^i_{n\times 1}$, $K^i_{1\times n} = 0$ $d_i = 1$. It can be obtained by

$$\begin{cases} u_{\mathrm{AL}_{\mathrm{AT}}} = a_{\mathrm{A}} \cos(\gamma_{\mathrm{A}} - \lambda_{\mathrm{AT}}) = u'_{\mathrm{A}} \cos(\gamma_{\mathrm{A}} - \lambda_{\mathrm{AT}}), \\ u_{\mathrm{TL}_{\mathrm{AT}}} = a_{\mathrm{T}} \cos(\gamma_{\mathrm{T}} + \lambda_{\mathrm{AT}}) = u'_{\mathrm{T}} \cos(\gamma_{\mathrm{T}} + \lambda_{\mathrm{AT}}), \\ u_{\mathrm{DL}_{\mathrm{AT}}} = a_{\mathrm{D}} \cos(\gamma_{\mathrm{D}} + \lambda_{\mathrm{AD}}) = u'_{\mathrm{D}} \cos(\gamma_{\mathrm{D}} + \lambda_{\mathrm{AD}}). \end{cases} \tag{7}$$

u_{A}, u_{T}, and u_{D} satisfy the following form:

$$\begin{cases} u_{\mathrm{A}} = u'_{\mathrm{A}} \cos(\gamma_{\mathrm{A}} - \lambda_{\mathrm{AT}}), \\ u_{\mathrm{T}} = u'_{\mathrm{T}} \cos(\gamma_{\mathrm{T}} + \lambda_{\mathrm{AT}}), \\ u_{\mathrm{D}} = u'_{\mathrm{D}} \cos(\gamma_{\mathrm{D}} + \lambda_{\mathrm{AD}}). \end{cases} \tag{8}$$

The state vector of the linearized engagement is expressed as follows:

$$x = [y_{\mathrm{AT}} \quad \dot{y}_{\mathrm{AT}} \quad y_{\mathrm{AD}} \quad \dot{y}_{\mathrm{AD}}]^{\mathrm{T}}. \tag{9}$$

The equations of motion corresponding to equation (9) are given by

$$\dot{x} = \begin{cases} \dot{y}_{\mathrm{AT}} = x_2, \\ \ddot{y}_{\mathrm{AT}} = u_{\mathrm{T}} - u_{\mathrm{A}}, \\ \dot{y}_{\mathrm{AD}} = x_4, \\ \ddot{y}_{\mathrm{AD}} = u_{\mathrm{D}} \Gamma(t) - \kappa u_{\mathrm{A}}. \end{cases} \tag{10}$$

The equations can be written in the following form:

$$\dot{x} = Ax + B[\, u_{\mathrm{T}} \quad u_{\mathrm{D}} \,]^{\mathrm{T}} + C u_{\mathrm{A}}, \tag{11}$$

where

$$A = \begin{bmatrix} 0 & 1 & 0 & 0 \\ 0 & 0 & 0 & 0 \\ 0 & 0 & 0 & 1 \\ 0 & 0 & 0 & 0 \end{bmatrix},$$

$$B = \begin{bmatrix} 0 & 0 \\ 1 & 0 \\ 0 & 0 \\ 0 & \Gamma(t) \end{bmatrix}, \tag{12}$$

$$C = \begin{bmatrix} 0 \\ -1 \\ 0 \\ -\kappa \end{bmatrix}.$$

The intercept times are considered to be fixed because of the problem occurring in the endgame phase, and they can be given by

$$\begin{cases} t_f^{\mathrm{AT}} = \dfrac{R_{\mathrm{AT}_0}}{V_{\mathrm{A}_0}\cos\left(\gamma_{\mathrm{A}_0} - \lambda_{\mathrm{AT}_0}\right) + V_{\mathrm{T}_0}\cos\left(\gamma_{\mathrm{T}_0} + \lambda_{\mathrm{AT}_0}\right)}, \\ t_f^{\mathrm{AD}} = \dfrac{R_{\mathrm{AD}_0}}{V_{\mathrm{A}_0}\cos\left(\gamma_{\mathrm{A}_0} - \lambda_{\mathrm{AD}_0}\right) + V_{\mathrm{D}_0}\cos\left(\gamma_{\mathrm{D}_0} + \lambda_{\mathrm{AD}_0}\right)}. \end{cases} \tag{13}$$

After t_f^{AD}, the defender will disappear. The time-to-go t_{go} can be described by

$$t_{\mathrm{go}}^i = t_f^i - t, \quad i = \{\mathrm{AT}, \mathrm{AD}\}. \tag{14}$$

3. Strategy for the Attacker

3.1. Order Reduction. The order of the problem needs to be reduced so that it can be solved expediently. The well-known zero-effort-miss (ZEM) distance between the attacker and the target can be expressed as follows:

$$Z_{\mathrm{AT}}(t) = D_{\mathrm{AT}}\Phi\left(t_f^{\mathrm{AT}}, t\right)x. \tag{15}$$

Similarly, the ZEM distance between the attacker and the defender can be expressed as follows:

$$Z_{\mathrm{AD}}(t) = D_{\mathrm{AD}}\Phi\left(t_f^{\mathrm{AD}}, t\right)x, \tag{16}$$

where $\Phi(t_f^{\mathrm{AT}}, t)$ and $\Phi(t_f^{\mathrm{AD}}, t)$ are the transition matrices with respect to equation (11),

$$\begin{cases} \dot{\Phi}\left(t_f^{\mathrm{AD}}, t\right) = -\Phi\left(t_f^{\mathrm{AD}}, t\right)A, \Phi\left(t_f^{\mathrm{AD}}, t_f^{\mathrm{AD}}\right) = \mathbf{I}, \\ \dot{\Phi}\left(t_f^{\mathrm{AT}}, t\right) = -\Phi\left(t_f^{\mathrm{AT}}, t\right)A, \Phi\left(t_f^{\mathrm{AT}}, t_f^{\mathrm{AT}}\right) = \mathbf{I}. \end{cases} \tag{17}$$

D_{AD} and D_{AT} are expressed as follows:

$$\begin{cases} D_{\mathrm{AD}} = [\,0 \quad 0 \quad 1 \quad 0\,], \\ D_{\mathrm{AT}} = [\,1 \quad 0 \quad 0 \quad 0\,]. \end{cases} \tag{18}$$

Equations (15) and (16) can be presented by

$$\begin{cases} Z_{\mathrm{AD}}(t) = y_{\mathrm{AD}} + \dot{y}_{\mathrm{AD}}\left(t_f^{\mathrm{AD}} - t\right), \\ Z_{\mathrm{AT}}(t) = y_{\mathrm{AT}} + \dot{y}_{\mathrm{AT}}\left(t_f^{\mathrm{AT}} - t\right). \end{cases} \tag{19}$$

The dynamics of $Z_{\mathrm{AT}}(t)$ and $Z_{\mathrm{AD}}(t)$ can be obtained by

$$\begin{cases} \dot{Z}_{\mathrm{AD}}(t) = \left(t_f^{\mathrm{AD}} - t\right)(-\kappa u_{\mathrm{A}} + \mathbf{\Gamma}(t)u_{\mathrm{D}}), \\ \dot{Z}_{\mathrm{AT}}(t) = \left(t_f^{\mathrm{AT}} - t\right)(-u_{\mathrm{A}} + u_{\mathrm{T}}). \end{cases} \tag{20}$$

3.2. One-to-One Optimal Strategies. In the attacker-target engagement, the attacker needs to pursue the target. The cost function to solve the problem is expressed by

$$J_{\mathrm{AT}} = \frac{1}{2}\left[y_{\mathrm{AT}}\left(t_f^{\mathrm{AT}}\right)\right]^2. \tag{21}$$

Because of $y_{\mathrm{AT}}(t_f^{\mathrm{AT}}) = Z_{\mathrm{AT}}(t_f^{\mathrm{AT}})$, the cost function can be rewritten in the following form:

$$J_{\mathrm{AT}} = \frac{1}{2}\left[Z_{\mathrm{AT}}\left(t_f^{\mathrm{AT}}\right)\right]^2. \tag{22}$$

Similarly, in the attacker-defender engagement, the attacker needs to evade from the defender. The cost function to solve the problem is expressed by

$$J_{\mathrm{AD}} = -\frac{1}{2}\left[Z_{\mathrm{AD}}\left(t_f^{\mathrm{AD}}\right)\right]^2. \tag{23}$$

The Hamiltonian functions corresponding to equations (23) and (22) are given by

$$\begin{cases} H_{\mathrm{AD}} = \lambda_1\dot{Z}_{\mathrm{AD}}(t), \\ H_{\mathrm{AT}} = \lambda_2\dot{Z}_{\mathrm{AT}}(t). \end{cases} \tag{24}$$

The adjoint equation and transversality condition are as follows:

$$\begin{cases} \dot{\lambda}_1 = -\dfrac{\partial H}{\partial Z_{\mathrm{AD}}} = 0, \quad \lambda_1\left(t_f^{\mathrm{AD}}\right) = \dfrac{\partial J_{\mathrm{AD}}}{\partial Z_{\mathrm{AD}}\left(t_f^{\mathrm{AD}}\right)} = -Z_{\mathrm{AD}}\left(t_f^{\mathrm{AD}}\right), \\ \dot{\lambda}_2 = -\dfrac{\partial H}{\partial Z_{\mathrm{AT}}} = 0, \quad \lambda_2\left(t_f^{\mathrm{AT}}\right) = \dfrac{\partial J_{\mathrm{AT}}}{\partial Z_{\mathrm{AT}}\left(t_f^{\mathrm{AT}}\right)} = Z_{\mathrm{AT}}\left(t_f^{\mathrm{AT}}\right). \end{cases} \tag{25}$$

Thus, the solution can be obtained as follows:

$$\begin{cases} \lambda_1(t) = -Z_{\mathrm{AD}}\left(t_f^{\mathrm{AD}}\right), \\ \lambda_2(t) = Z_{\mathrm{AT}}\left(t_f^{\mathrm{AT}}\right). \end{cases} \tag{26}$$

Substituting equations (26) and (20) into equation (24), it can be obtained in the following form:

$$\begin{cases} H_{\mathrm{AD}} = -Z_{\mathrm{AD}}\left(t_f^{\mathrm{AD}}\right)\left(t_f^{\mathrm{AD}} - t\right)(-u_{\mathrm{A}}\kappa + \mathbf{\Gamma}(t)u_{\mathrm{D}}), \\ H_{\mathrm{AT}} = Z_{\mathrm{AT}}\left(t_f^{\mathrm{AT}}\right)\left(t_f^{\mathrm{AT}} - t\right)(-u_{\mathrm{A}} + u_{\mathrm{T}}). \end{cases} \tag{27}$$

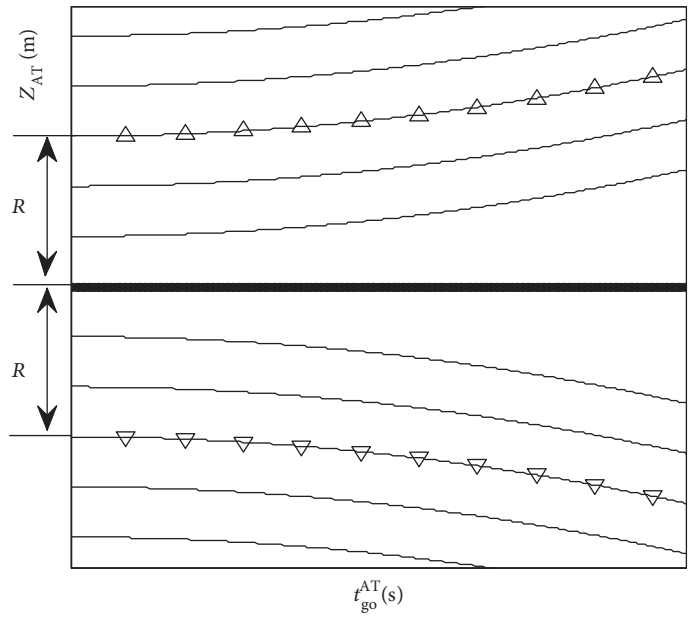

Figure 2: Optimal pursuit trajectories.

The optimal strategies for the attacker-target engagement are as follows:

$$\begin{cases} u_A^\Theta = \text{sign}(Z_{AT}(t))u_A^{\max}, \\ u_T^\Theta = \text{sign}(Z_{AT}(t))u_T^{\max}. \end{cases} \tag{28}$$

The optimal strategies for the attacker-defender engagement are as follows:

$$\begin{cases} u_A^\Theta = -\text{sign}[Z_{AD}(t)\kappa]u_A^{\max}, \\ u_D^\Theta = -\text{sign}(Z_{AD}(t))u_D^{\max}, \end{cases} \tag{29}$$

where superscript max represents the maximal value.

3.3. Optimal Trajectories for the Attacker. In the attacker-target engagement, the optimal pursuit strategy for the attacker in equation (28) is

$$u_A^\Theta = \text{sign}(Z_{AT}(t))u_A^{\max}. \tag{30}$$

It is assumed that $u_A^{\max}, u_T^{\max}$, and $u_D^{\max}$ satisfy $u_A^{\max} > u_T^{\max}$ and $u_A^{\max} > u_D^{\max}$ in the scenario. $\dot{Z}_{AT}(t)$ satisfies the following form:

$$\dot{Z}_{AT}(t) = t_{go}^{AT}[-\text{sign}(Z_{AT}(t))u_A^{\max} + \text{sign}(Z_{AT}(t))u_T^{\max}]. \tag{31}$$

The kill radius of the attacker is R; $Z_{AT}(t)$ satisfies

$$Z_{AT}(t) + \int_t^{t_f^{AT}} [-\text{sign}(Z_{AT}(t))u_A^{\max} + \text{sign}(Z_{AT}(t))u_T^{\max}]\left(t_f^{AT} - \xi\right)d\xi = R. \tag{32}$$

The positive and negative pursuit boundary trajectories are given by

$$\begin{cases} Z_{AT}^\Theta\left(t_{go}^{AT}\right) = R - \frac{1}{2}(-u_A^{\max} + u_T^{\max})\left(t_{go}^{AT}\right)^2, \\ -Z_{AT}^\Theta\left(t_{go}^{AT}\right) = -R + \frac{1}{2}(-u_A^{\max} + u_T^{\max})\left(t_{go}^{AT}\right)^2. \end{cases} \tag{33}$$

Figure 2 presents the optimal pursuit trajectories. The positive and negative boundary trajectories are marked with triangles. In the engagement, the attacker uses the optimal pursuit guidance law, and the target uses the optimal evasion guidance law corresponding to equation (28). If $Z_{AT}(t)$ locates on the boundary trajectories, the final miss distance between the attacker and the target will be R. If $Z_{AT}(t)$ locates within the zone between the positive and negative boundary trajectories, the final miss distance between the attacker and the target will be less than R; thus, the attacker can hit the target successfully. Conversely, the aircraft evades the attacker successfully.

The defender is launched from the target; thus, κ is always a positive value. Similarly, $\dot{Z}_{AD}(t)$ satisfies the following form:

$$\dot{Z}_{AD}(t) = t_{go}^{AD}[\text{sign}(Z_{AD}(t))u_A^{\max}\kappa - \text{sign}(Z_{AD}(t))u_D^{\max}]. \tag{34}$$

The kill radius of the defender is M; $Z_{AD}(t)$ satisfies

$$Z_{AD}(t) + \int_t^{t_f^{AD}} [\text{sign}(Z_{AD}(t))u_A^{\max}\kappa - \text{sign}(Z_{AD}(t))u_D^{\max}]\left(t_f^{AD} - \xi\right)d\xi = M. \tag{35}$$

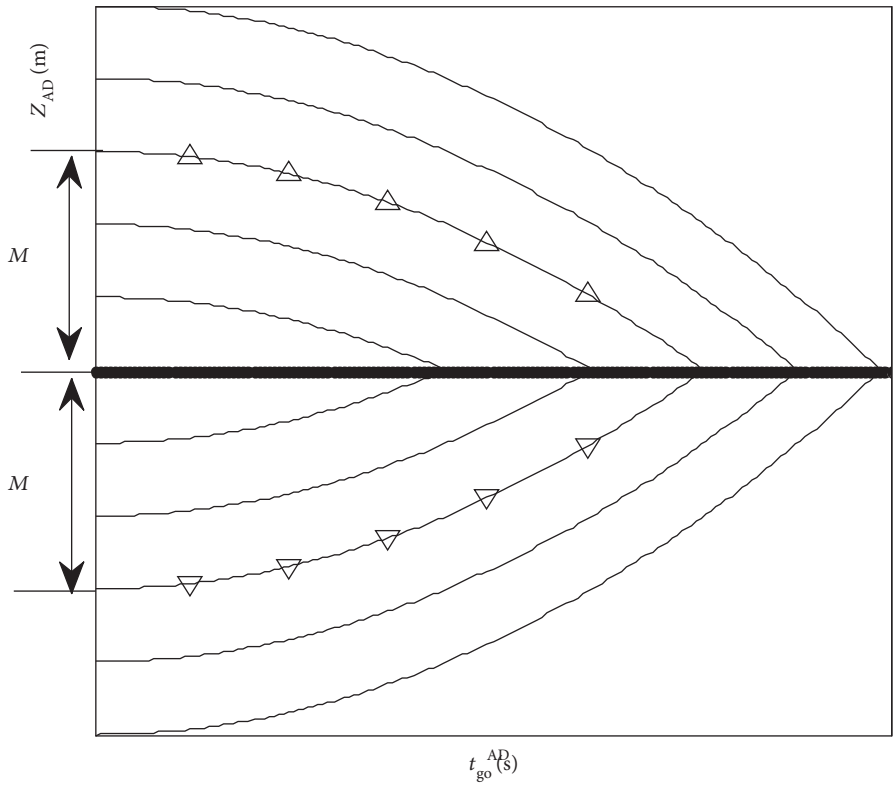

Figure 3: Optimal evasion trajectories.

The positive and negative evasion boundary trajectories are given by

$$\begin{cases} Z_{AD}^{\Theta}\left(t_{go}^{AD}\right) = M - \frac{1}{2}\left(u_A^{max}\kappa - u_D^{max}\right)\left(t_{go}^{AD}\right)^2, \\ -Z_{AD}^{\Theta}\left(t_{go}^{AD}\right) = -M + \frac{1}{2}\left(u_A^{max}\kappa - u_D^{max}\right)\left(t_{go}^{AD}\right)^2. \end{cases} \tag{36}$$

Figure 3 presents the optimal evasion trajectories under the condition that $u_A^{max}\kappa > u_D^{max}$. The positive and negative boundary trajectories are marked with triangles. In the engagement, the attacker uses the optimal evasion guidance law, and the defender uses the optimal intercept guidance law corresponding to equation (29). If $Z_{AD}(t)$ locates on the boundary trajectories, the final miss distance between the attacker and the defender will be M. If $Z_{AD}(t)$ locates without the zone between the positive and negative boundary trajectories, the final miss distance between the attacker and the defender will be larger than M; thus, the attacker can evade the defender successfully. Conversely, the defender intercepts the attacker successfully.

It can be noted that if the signs of Z_{AT} and Z_{AD} are the same, the optimal strategies of the attacker are different in equations (28) and (29). It means that when the attacker pursues the target, it will approach the defender. Figure 4 shows the time evolution of the ZEMs for the situation in which the attacker evades the defender before the engagement time t_f^{AD}, then pursues the target. It is shown that if the attacker evades the defender before t_f^{AD}, the absolute value of Z_{AT} will increase heavily, and it will go out of the zone between the positive and negative pursuit boundary trajectories easily. Thus, it is difficult for the attacker to pursue the target successfully after t_f^{AD}.

Figure 5 shows the time evolution of the ZEMs for the situation in which the attacker pursues the target in the total endgame phase. It is shown that the value of Z_{AD} will easily go in the zone between the positive and negative evasion boundary trajectories. Thus, the attacker can be intercepted easily by the defender because the attacker only pursues the target and ignores the defender.

3.4. Optimal Pursuit Strategy for the Attacker. If the attacker wants to win the game, the attacker needs to evade from the defender and pursue the target. Thus, the cost function is designed by

$$J = -\frac{1}{2}\alpha\left[Z_{AD}\left(t_f^{AD}\right)\right]^2 + \frac{1}{2}\beta\left[Z_{AT}\left(t_f^{AT}\right)\right]^2, \tag{37}$$

where α and β are nonnegative weights.

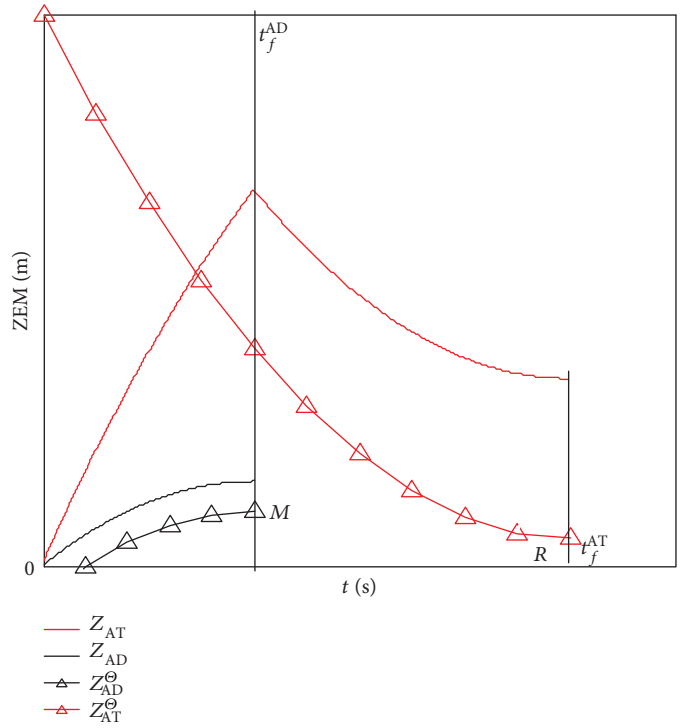

Figure 4: Time evolution of the ZEMs for the attacker evading the defender before t_f^{AD}.

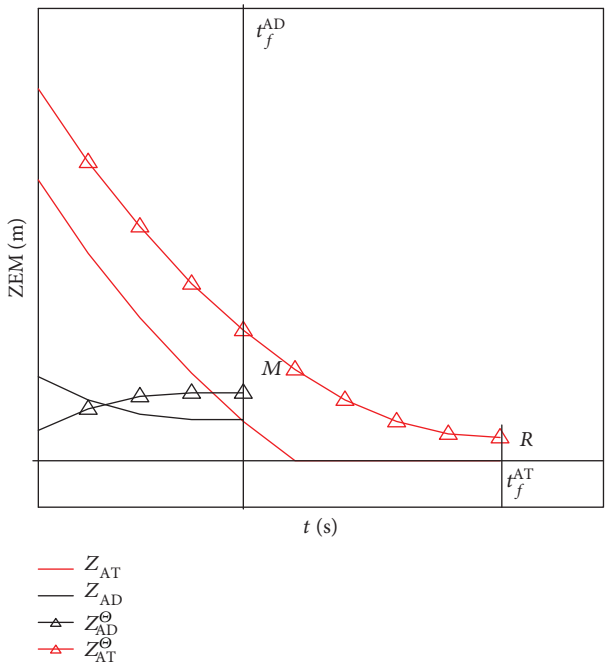

Figure 5: Time evolution of the ZEMs for the attacker pursuing the target in the total endgame phase.

Table 1: Initial parameters.

Parameters (unit)	Target	Attacker	Defender
Initial position (km)	(6, 2)	(0, 0)	(6, 2)
Initial course (deg)	5	0	7.5
Maximal acceleration (m/s^2)	50	180	70
Speed (m/s)	300	600	800

The Hamiltonian function of the problem is in the following form:

$$H = \lambda_1 \dot{Z}_{AD}(t) + \lambda_2 \dot{Z}_{AT}(t). \tag{38}$$

Parameters satisfy

$$\begin{cases} \dot{\lambda}_1 = -\dfrac{\partial H}{\partial Z_{AD}} = 0, \\ \lambda_1\left(t_f^{AD}\right) = \dfrac{\partial J}{\partial Z_{AD}\left(t_f^{AD}\right)} = -\alpha Z_{AD}\left(t_f^{AD}\right), \\ \dot{\lambda}_2 = -\dfrac{\partial H}{\partial Z_{AT}} = 0, \\ \lambda_2\left(t_f^{AT}\right) = \dfrac{\partial J}{\partial Z_{AT}\left(t_f^{AT}\right)} = \beta Z_{AT}\left(t_f^{AT}\right). \end{cases} \tag{39}$$

Substituting equations (39) and (20) into equation (38),

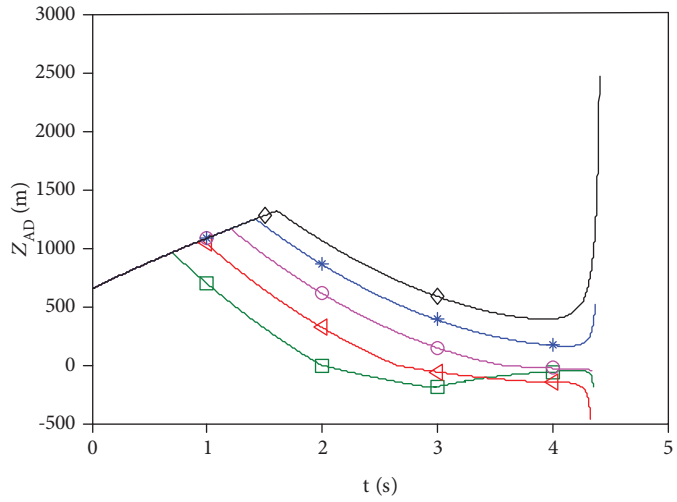

Figure 6: Time evolutions of $Z_{AD}(t)$.

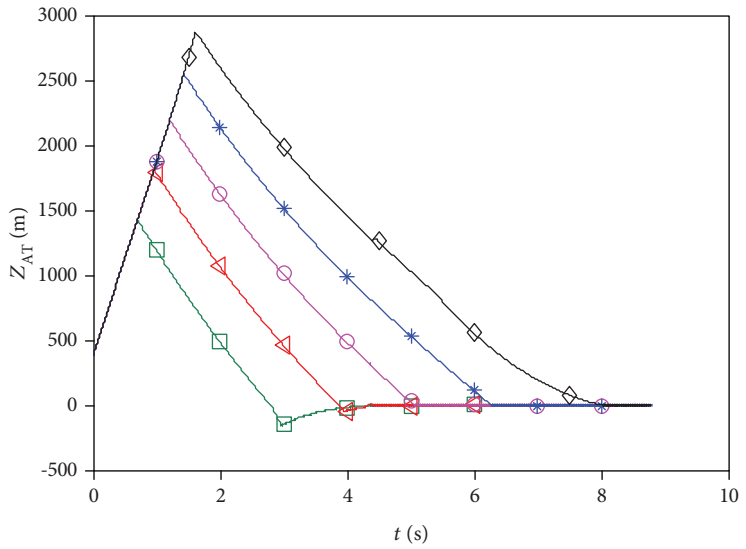

Figure 7: Time evolutions of $Z_{AT}(t)$.

we can obtain the following equation:

$$H = \left[\alpha Z_{AD}\left(t_f^{AD}\right)\boldsymbol{\Gamma}(t)\kappa t_{go}^{AD} - \beta Z_{AT}\left(t_f^{AT}\right)t_{go}^{AT}\right] \times u_A - \alpha Z_{AD}\left(t_f^{AD}\right)\boldsymbol{\Gamma}(t)t_{go}^{AD}u_D + \beta Z_{AT}\left(t_f^{AT}\right)t_{go}^{AT}u_T. \quad (40)$$

The open-loop optimal strategies can be expressed as follows:

$$\begin{cases} u_A^{\Theta} = -\text{sign}\left[\alpha Z_{AD}\left(t_f^{AD}\right)\boldsymbol{\Gamma}(t)t_{go}^{AD}\kappa - \beta Z_{AT}\left(t_f^{AT}\right)t_{go}^{AT}\right]u_A^{max}, \\ u_T^{\Theta} = \text{sign}\left[Z_{AT}\left(t_f^{AT}\right)t_{go}^{AT}\right]u_T^{max}, \\ u_D^{\Theta} = -\text{sign}\left[Z_{AD}\left(t_f^{AD}\right)\alpha\boldsymbol{\Gamma}(t)t_{go}^{AD}\right]u_D^{max}. \end{cases} \quad (41)$$

The close-loop optimal strategies of u_T^{Θ} and u_D^{Θ} are solved as follows:

$$\begin{cases} u_T^{\Theta} = \text{sign}\left[Z_{AT}(t)t_{go}^{AT}\right]u_T^{max}, \\ u_D^{\Theta} = -\text{sign}\left[Z_{AD}(t)\alpha\boldsymbol{\Gamma}(t)t_{go}^{AD}\right]u_D^{max}, \end{cases} \quad (42)$$

where superscript max represents the maximal value.

The close-loop optimal strategy of the attacker is difficult to obtain. The open-loop optimal strategy is

$$u_A^{\Theta} = -\text{sign}\left[\alpha Z_{AD}\left(t_f^{AD}\right)\boldsymbol{\Gamma}(t)t_{go}^{AD}\kappa - \beta Z_{AT}\left(t_f^{AT}\right)t_{go}^{AT}\right]u_A^{max}. \quad (43)$$

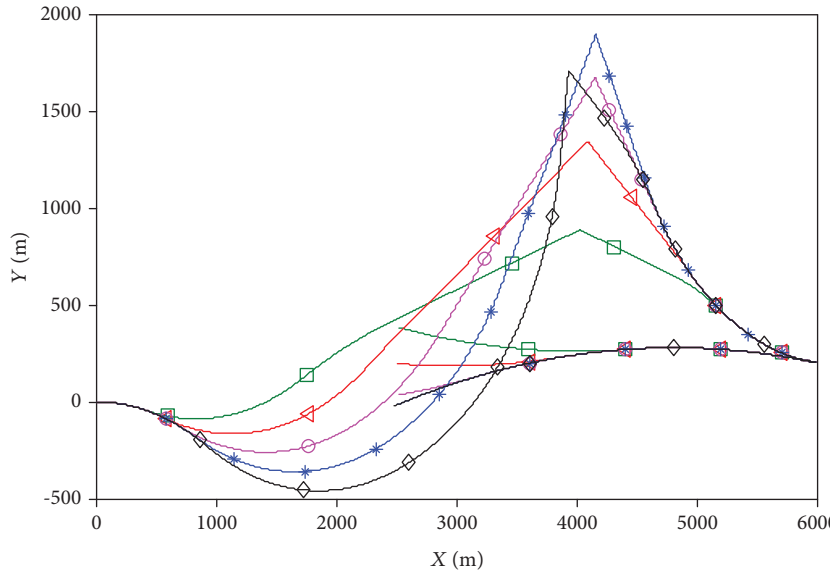

Figure 8: Time evolutions of trajectories.

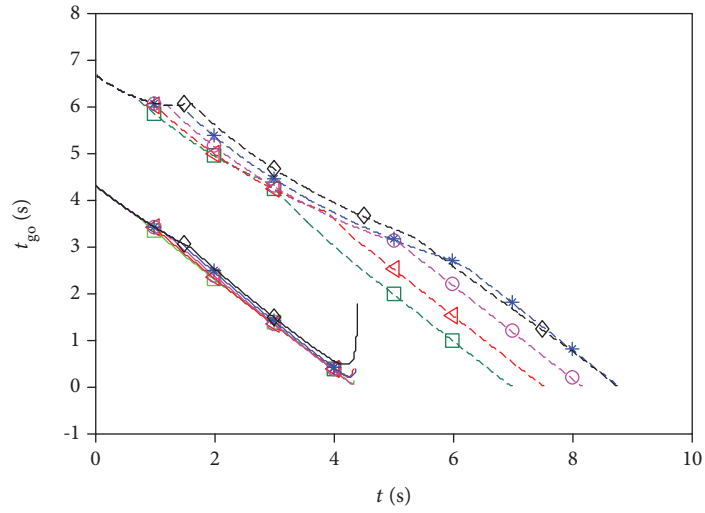

Figure 9: Time evolutions of time-to-go.

The strategy is designed for the attacker to evade from the defender and pursue the target as follows:

$$u_{\mathrm{A}}^{\Theta} = \mathrm{sign}\left[\alpha Z_{\mathrm{AD}}(t)\mathbf{\Gamma}(t)t_{\mathrm{go}}^{\mathrm{AD}}\kappa - \beta Z_{\mathrm{AT}}(t)t_{\mathrm{go}}^{\mathrm{AT}}\right]u_{\mathrm{A}}^{\max}. \quad (44)$$

Equation (44) can be rewritten as follows:

$$u_{\mathrm{A}}^{\Theta} = \mathrm{sign}\left[\frac{\alpha}{\beta}Z_{\mathrm{AD}}(t)\mathbf{\Gamma}(t)t_{\mathrm{go}}^{\mathrm{AD}}\kappa - Z_{\mathrm{AT}}(t)t_{\mathrm{go}}^{\mathrm{AT}}\right]u_{\mathrm{A}}^{\max}. \quad (45)$$

4. Nonlinear Simulation

The initial condition is shown in Table 1.

Figures 6, 7, 8, and 9 show the time evolutions of $Z_{\mathrm{AD}}(t)$, $Z_{\mathrm{AT}}(t)$, three players' trajectories, and time-to-go by using nonlinear simulation for different values of α/β. Figure 10 shows the values of the control parameters corresponding to $\alpha/\beta Z_{\mathrm{AD}}(t)t_{\mathrm{go}}^{\mathrm{AD}}\kappa$ and $Z_{\mathrm{AT}}(t)t_{\mathrm{go}}^{\mathrm{AT}}$. In the simulation phase, the initial line of sight is updated in real time, and t_f^{AD} and t_f^{AT} are replaced by $t_{\mathrm{go}}^{\mathrm{AD}}$ and $t_{\mathrm{go}}^{\mathrm{AT}}$. The meaning of the lines for different values of α/β are shown in Figure 11. The engagement times and the miss distances are shown in Table 2.

It is shown that when the time approaches the engagement time t_f^{AD}, the absolute value of $Z_{\mathrm{AD}}(t)$ increases substantially because at this time, the LOS changes quickly, and $t_{\mathrm{go}}^{\mathrm{AD}}$ increases heavily. It is noted that at the initial time, $Z_{\mathrm{AD}}(t)$ and $Z_{\mathrm{AT}}(t)$ increase because at this time, the absolute value of $\alpha/\beta Z_{\mathrm{AD}}(t)t_{\mathrm{go}}^{\mathrm{AD}}\kappa$ is bigger than that of $Z_{AT}(t)t_{go}^{AT}$, and the attacker tries to minimize the cost function. As time goes on, the absolute value of $Z_{AT}(t)t_{go}^{AT}$ increases more quickly,

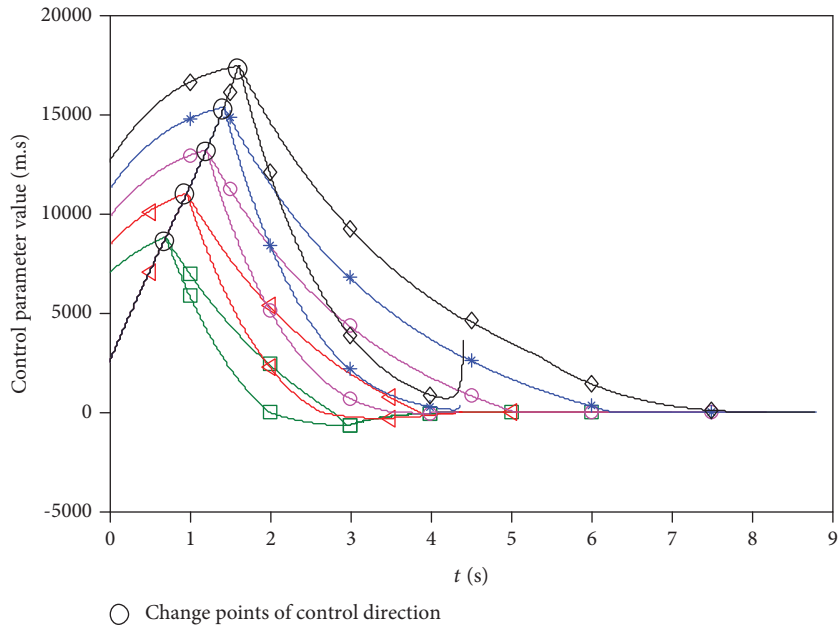

FIGURE 10: Time evolutions of the control parameters of $\alpha/\beta Z_{\mathrm{AD}}(t)t_{\mathrm{go}}^{\mathrm{AD}}\kappa$ and $Z_{AT}(t)t_{go}^{AT}$.

α/β value	$Z_{\mathrm{AD}}(t)$ (Figure 6)	$Z_{\mathrm{AT}}(t)$ (Figure 7)	Attacker trajectory Figure 8	Defender trajectory Figure 8	Target trajectory Figure 8	$t_{\mathrm{go}}^{\mathrm{AD}}$ (Figure 9)	$t_{\mathrm{go}}^{\mathrm{AT}}$ (Figure 9)	α/β x $Z_{\mathrm{AD}}(t)$ $t_{\mathrm{go}}^{\mathrm{AD}}\kappa$ value (Figure 10)	$Z_{\mathrm{AT}}(t)t_{\mathrm{go}}^{\mathrm{AT}}$ value (Figure 10)
2.5									
3									
3.5									
4									
4.5									

FIGURE 11: Meanings of the lines for different values of α/β.

and its influence on the cost function becomes greater. Thus, the control direction of the attacker changes, which leads to the decrease of $Z_{\mathrm{AD}}(t)$ and $Z_{\mathrm{AT}}(t)$. It can be concluded that the attacker can evade from the defender and hit the target by using the derived strategy through observing the trajectories, and results are shown in Figure 8 and Table 2.

5. Conclusion

The scenario in which the attacker attacks the active defense aircraft is investigated. In this scenario, the target evades the attacker, and the defender intercepts the attacker by using optimal guidance laws. The optimal

Table 2: Simulation results for different values of α/β.

α/β	Miss distance (m) (AD)	Miss distance (m) (AT)	t_f^{AT} (s)	t_f^{AD} (s)
2.5	47.464	0.235	6.9913	4.3632
3	132.881	0.183	7.5299	4.3645
3.5	32.875	0.389	8.1781	4.3622
4	141.523	0.062	8.7972	4.4023
4.5	318.687	0.045	8.7778	4.4392

one-to-one guidance law is derived for the attacker. If the attacker evades the defender by using the optimal evasion guidance law before t_f^{AD}, it will go out of the zone between the positive and negative pursuit boundary trajectories easily. Thus, it is difficult for the attacker to pursue the target successfully after t_f^{AD}. If the attacker pursues the target in the total endgame phase, the value of Z_{AD} will easily go in the zone between the positive and negative evasion boundary trajectories, and the attacker can be intercepted by the defender.

Thus, a new strategy is derived for the attacker to win the game in the active defense scenario. In this problem, the target evades from the attacker, and the defender intercepts the attacker by using the derived close-loop optimal strategies. Although the close-loop strategy is difficult to obtain by using the presented cost function for the attacker, an available strategy is designed for it based on the open-loop solution. The attacker can accomplish the task of evading from the defender and pursuing the target by using the derived strategy.

Data Availability

The data used to support the findings of this study are available from the corresponding author upon request.

Conflicts of Interest

The authors declare that they have no competing interests.

Acknowledgments

This work was cosupported by the National Natural Science Foundation of China (11672093) and the Shanghai Aerospace Science and Technology Innovation Foundation (SAST2016039).

References

[1] P. Zarchan, "Tactical and strategic missile guidance," *Progress in Astronautics and Aeronautics*, vol. 219, pp. 11–29, 2007.

[2] Z. Yang, H. Wang, D. Lin, and L. Zang, "A new impact time and angle control guidance law for stationary and nonmaneuvering targets," *International Journal of Aerospace Engineering*, vol. 2016, Article ID 6136178, 14 pages, 2016.

[3] J. Ye, H. Lei, and J. Li, "Novel fractional order calculus extended PN for maneuvering targets," *International Journal of Aerospace Engineering*, vol. 2017, Article ID 5931967, 9 pages, 2017.

[4] Y. Si and S. Song, "Three-dimensional adaptive finite-time guidance law for intercepting maneuvering targets," *Chinese Journal of Aeronautics*, vol. 30, no. 6, pp. 1985–2003, 2017.

[5] Y. Zhang, S. Tang, and J. Guo, "An adaptive fast fixed-time guidance law with an impact angle constraint for intercepting maneuvering targets," *Chinese Journal of Aeronautics*, vol. 31, no. 6, pp. 1327–1344, 2018.

[6] T. Wang, S. Tang, J. Guo, and H. Zhang, "Two-phase optimal guidance law considering impact angle constraint with bearings-only measurements," *International Journal of Aerospace Engineering*, vol. 2017, Article ID 1380531, 12 pages, 2017.

[7] Z. Yang, H. Wang, and D. Lin, "Time-varying biased proportional guidance with seeker's field-of-view limit," *International Journal of Aerospace Engineering*, vol. 2016, Article ID 9272019, 11 pages, 2016.

[8] S. S. Kumkov, S. L. Menec, and V. S. Patsko, "Solvability sets in pursuit problem with two pursuers and one evader," *IFAC Proceedings Volumes*, vol. 47, no. 3, pp. 1543–1549, 2014.

[9] S. S. Kumkov, S. Le Ménec, and V. S. Patsko, "Level sets of the value function in differential games with two pursuers and one evader. Interval analysis interpretation," *Mathematics in Computer Science*, vol. 8, no. 3-4, pp. 443–454, 2014.

[10] J. Zhao and S. Yang, "Integrated cooperative guidance framework and cooperative guidance law for multi-missile," *Chinese Journal of Aeronautics*, vol. 31, no. 3, pp. 546–555, 2018.

[11] X. Wei, Y. Wang, S. Dong, and L. Liu, "A three-dimensional cooperative guidance law of multimissile system," *International Journal of Aerospace Engineering*, vol. 2015, 8 pages, 2015.

[12] J. Zeng, L. Dou, and B. Xin, "A joint mid-course and terminal course cooperative guidance law for multi-missile salvo attack," *Chinese Journal of Aeronautics*, vol. 31, no. 6, pp. 1311–1326, 2018.

[13] R. Boyell, "Defending a moving target against missile or torpedo attack," *IEEE Transactions on Aerospace and Electronic Systems*, vol. AES-12, no. 4, pp. 522–526, 1976.

[14] R. Boyell, "Counterweapon aiming for defense of a moving target," *IEEE Transactions on Aerospace and Electronic Systems*, vol. AES-16, no. 3, pp. 402–408, 1980.

[15] J. Shinar and G. Silberman, "A discrete dynamic game modelling anti-missile defense scenarios," *Dynamics and Control*, vol. 5, no. 1, pp. 55–67, 1995.

[16] I. Rusnak, "The lady, the bandits and the body guards - a two team dynamic game," in *Proceedings of the 16th world IFAC congress*, pp. 441–446, Prague, Czech Republic, July 2005.

[17] A. Ratnoo and T. Shima, "Line-of-sight interceptor guidance for defending an aircraft," *Journal of Guidance, Control, and Dynamics*, vol. 34, no. 2, pp. 522–532, 2011.

[18] T. Shima, "Optimal cooperative pursuit and evasion strategies against a homing missile," *Journal of Guidance, Control, and Dynamics*, vol. 34, no. 2, pp. 414–425, 2011.

[19] O. Prokopov and T. Shima, "Linear quadratic optimal cooperative strategies for active aircraft protection," *Journal of Guidance, Control, and Dynamics*, vol. 36, no. 3, pp. 753–764, 2013.

[20] J. F. Fisac and S. S. Sastry, "The pursuit-evasion-defense differential game in dynamic constrained environments," in *2015 54th IEEE Conference on Decision and Control (CDC)*, pp. 4549–4556, Osaka, Japan, December 2015.

[21] D. W. Oyler, P. T. Kabamba, and A. R. Girard, "Pursuit-evasion games in the presence of obstacles," *Automatica*, vol. 65, no. 1, pp. 1–11, 2016.

[22] S. Zhang, Y. Guo, and S. Wang, "Cooperative intercept guidance of multiple aircraft with a lure role included," *International Journal of Aerospace Engineering*, vol. 2018, Article ID 4126807, 15 pages, 2018.

[23] S. Qilong, Q. Naiming, X. Zheyao, L. Yanfang, and Z. Yong, "An optimal one-way cooperative strategy for two defenders against an attacking missile," *Chinese Journal of Aeronautics*, vol. 30, no. 4, pp. 1506–1518, 2017.

[24] E. Garcia, D. W. Casbeer, K. Pham, and M. Pachter, "Cooperative aircraft defense from an attacking missile," in *53rd IEEE Conference on Decision and Control*, pp. 2926–2931, Los Angeles, CA, USA, December 2014.

[25] E. Garcia, D. W. Casbeer, and M. Pachter, "Active target defense differential game with a fast defender," in *2015 American Control Conference (ACC)*, pp. 3752–3757, Chicago, IL, USA, July 2015.

[26] S. R. Kumar and T. Shima, "Cooperative nonlinear guidance strategies for aircraft defense," *Journal of Guidance, Control, and Dynamics*, vol. 40, no. 1, pp. 124–138, 2017.

[27] Q. Sun, N. Qi, L. Xiao, and H. Lin, "Differential game strategy in three-player evasion and pursuit scenarios," *Journal of Systems Engineering and Electronics*, vol. 29, no. 2, pp. 352–366, 2018.

[28] S. Rubinsky and S. Gutman, "Three-player pursuit and evasion conflict," *Journal of Guidance, Control, and Dynamics*, vol. 37, no. 1, pp. 98–110, 2014.

[29] N. Qi, Q. Sun, and J. Zhao, "Evasion and pursuit guidance law against defended target," *Chinese Journal of Aeronautics*, vol. 30, no. 6, pp. 1958–1973, 2017.

Hindawi
International Journal of Aerospace Engineering
Volume 2019, Article ID 3729480, 10 pages
https://doi.org/10.1155/2019/3729480

Research Article

Analyzing the Departure Runway Capacity Effects of Integrating Optimized Continuous Climb Operations

Manuel Villegas Díaz,[1] **Fernando Gómez Comendador**,[1] **Javier García-Heras Carretero**,[2] **and Rosa María Arnaldo Valdés**[1]

[1]*Universidad Politécnica de Madrid, Madrid 28040, Spain*
[2]*Universidad Carlos III de Madrid, Leganés 28911, Spain*

Correspondence should be addressed to Manuel Villegas Díaz; manuel.villegas.diaz@alumnos.upm.es

Received 30 August 2018; Revised 18 December 2018; Accepted 25 December 2018; Published 11 February 2019

Guest Editor: Yoshinori Matsuno

Performing Continuous Climb Operation (CCO) procedures enable the reduction of the environmental footprint and the improvement of the trajectory efficiency when individually operated. However, its operation may affect negatively the overall operational efficiency at Terminal Manoeuvring Areas (TMAs). The estimation of capacity is a matter of paramount importance to all airport planning and analyzing the capacity effects of this particular operational technique on a certain scenario will definitely help on evaluating its potential applicability. In this paper, departure runway capacity at the Adolfo Suárez Madrid-Barajas airport was operationally evaluated when introducing CCOs. The considered trajectories consisted of multiobjective optimized CCOs based on the optimal control theory, using the pseudospectral direct numerical method. These scenarios allowed addressing of the incremental variations of CCOs versus conventional departures, through fast time simulation, with the objective to assess the effects on the operations.

1. Introduction

Defined as an uninterrupted climb flight operation allowing the aircraft to attain initial cruise flight level at an optimum air speed with optimal thrust settings [1], the Continuous Climb Operation (CCO) leads to a significant fuel economy and environmental benefits. The improvement of flight trajectories through the execution of a flight profile optimized to the performance of an aircraft represents a significant enabler for Trajectory-Based Operations (TBO), which is one of the four pillars (four-phase improvement) defined on Single European Sky ATM Research (SESAR) [2].

At a local level, continuous operating techniques, such as CCOs, can significantly reduce the environmental footprint in living areas around the airports. Besides, this technique allows the airspace users to plan and, ideally, to fly a trajectory which will be closer to their preferences whilst complying with operational constraints. This may be translated into positive contributions on cost benefits through satisfying the airspace users' business needs.

As part of the Aviation System Block Upgrade (ASBU) system engineering modernization strategy, Global Air Navigation Plan (GANP) [3], the International Civil Aviation Organization (ICAO) prioritizes the usage of CCOs among other initiatives. Along these lines, global air navigation initiatives for future air traffic management like the Single European Sky ATM Research (SESAR) [2] in Europe and The Next Generation Air Transportation System (NextGen) [4] in the United States of America put in place innovative activities for the optimization of vertical trajectories. The departure phase of the flight has been identified as a key area where substantial environmental benefits could be achieved.

The optimization of flight trajectories for terminal operating procedures has been a problem extensively tackled for years, particularly focused on arrival procedures. Limited research has been conducted in terms of "pure" CCOs, as the benefits did not seem to be noteworthy. However,

considering that engines usually run close to full throttle during a climb phase, there exist the potential for reducing the environmental footprint in living areas around the airports. In this regard, McConnachie et al. [5] presented the evidences for environmental performance change in case CCOs are applied at certain airports. Nevertheless, it was plausibly assumed that a CCO is just an uninterrupted climb. The successful application of a CCO should not be simplistically reduced to the operation of an uninterrupted climb procedure, which implies inexistent level-off segments. It is important to note the importance of factors like the aircraft, airport type, aircraft weight, runway, Standard Instrument Departure (SID), and operational constraints when identifying the CCO profile optimized to the performance of the aircraft.

However, the integration of a CCO-operating technique in a Terminal Manoeuvring Area (TMA) requires the analysis of one of the most important parameters on airport planning, which is capacity. This Key Performance Area (KPA), which is one of the eleven KPAs defined by ICAO, at high-density terminal areas motivated the interesting work presented by Li et al. [6]. The model introduced for terminal area design is mainly focused on arrival trajectories. It is important to highlight that the integration of a pure CCO has not been directly considered by recent investigations; therefore, an assessment of the operational limitations and its potential effects would be tempting.

In Europe, SESAR targets up to 30% reduction in departure delays. On the other hand, its environmental expectation targets up to 10% reduction in CO_2 emissions including a positive impact on noise and air quality. Along with this KPA, the operational efficiency aims up to 6% reduction in flight time and up to 10% reduction in fuel burn. The successful achievement of all these targets is not trivial considering that the implementation of an environmental friendly operational procedure may produce negative effects on other KPAs.

It is likely to obtain local positive environmental effects through the application of optimized CCOs whilst affecting negatively airport efficiency operations. In other words, a new operating technique that seems to be beneficial when it is applied in isolation may not be quite beneficial when integrated as a part of a complete scenario. The study presented at this paper is aimed at studying the capacity effects when applying optimized CCOs. The Adolfo Suárez Madrid-Barajas airport (ICAO code, LEMD) has been selected as the test scenario to evaluate the effects on capacity when facilitating CCOs. The study has been enabled by a consolidated multiobjective software model, which was previously developed by the authors, for the computation of aircraft trajectories when performing optimal CCOs in terms of noise and fuel consumption.

To this end, the paper is organized as follows: Section 2 gathers the description of the scenario. Section 3 includes the aircraft performance model. Section 4 provides the operational constraints as well as the boundary conditions. Section 5 describes the used methodology for tackling the exercise. Section 6 presents the results, which offers the main findings of the analysis. And finally, Section 7 concludes with the key remarks of the study.

2. Departures at Adolfo Suárez Madrid-Barajas

Adolfo Suárez Madrid-Barajas is the largest airport in Spain with 378,566 total operations in 2017. Considered as one of the largest airport in Europe by physical size, it is the country's busiest airport in Spain, and Europe's sixth busiest. The airport is predominantly operated in north configuration and runway (RWY) 36L was selected as the preferred option for this study. In particular, the chosen flight segments go from ground to waypoint (WPT) AVILA. A shorter flight segment which is common for two Standard Instrument Departures (SIDs): Bardi Two Tango (BARDI2T) and Cáceres One Tango (CCS1T), and a longer flight segment, which is shared by Bardi Two Kilo (BARDI2K) SID and Cáceres One Kilo (CCS1K) SID. The operations of these SIDs are limited by the performance of the aircraft and aircraft type as clarified below.

Figure 1 shows a zoom view of the published chart, which includes the SIDs for RWY 36L, usable at daytime. SIDs BARDI2T/CCS1T are only allowed to authorized aircraft and, thus, BARDI2K/CCS1K becomes mandatory to listed aircraft due to noise restrictions. Published noise abatement procedures are applicable to all takeoffs, unless exceptionally cancelled due to an event that cannot be reasonably anticipated.

This is a challenging scenario as the performance of the aircraft plays a relevant role when performing BARDI2K/CCS1K or BARDI2T/CCS1T SID. The facilitation of CCO when performing these departure segments must satisfy the airspace restrictions and operational constraints.

3. Aircraft Performance

This section gathers the aircraft dynamics equations considered for this study. The considered representation of the aircraft is a dynamic model, which represents the point variable mass motion over a spherical flat nonrotating earth model besides neglecting wind components. The resulting set of differential equations of the aircraft is the following:

$$\begin{aligned}
\dot{x} &= V.\cos(\gamma),\\
\dot{h} &= V.\sin(\gamma),\\
\dot{V} &= \frac{T(h,V) - D(h,V,C_d) - m.g.\sin(\gamma)}{m(t)},\\
\dot{\gamma} &= \frac{L(h,V,C_l) - m.g.\sin(\gamma)}{m(t).V(t)},\\
\dot{m} &= -T(h,V).\eta(h,V),
\end{aligned} \tag{1}$$

where the state vector is comprised of the true airspeed V, the longitudinal position x, the aerodynamic flight path angle γ, the altitude h, and the mass of the aircraft m. In addition to the states, there are other components like T, which represents the thrust, g the gravity acceleration (assumed as a constant value), D is the aerodynamic drag, and η is the thrust-specific fuel flow.

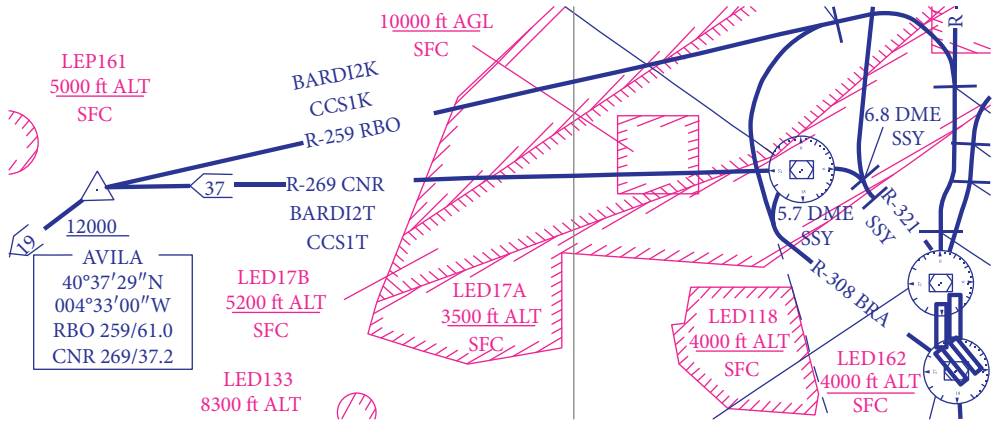

Figure 1: SIDs RWY 36L. Detailed view of selected flight segments associated to BARDI2T/CCS1T & BARDI2K/CCS1K SIDs.

Table 1: Operational constraints.

SID	BARDI2T/CCS1T	BARDI2K/CCS1K
MCG	6.4% to 10000 ft	7.5% to 4500 ft
KIAS constraints (1)	5.7 DME SSY: 180-240 kt	15 DME BRA h ≥ 6500 ft
KIAS constraints (2)	h ≤ 10000 ft KIAS ≤ 250 kt	
AVILA (2)	h ≥ 12000 ft	

In terms of the atmosphere, it has been considered the ICAO Standard Atmosphere (ISA) model [7], which presents pressure $p(h)$, density $\rho(h)$, and temperature $\tau(h)$. This model denotes p_0, ρ_0, and τ_0 for the standard values at sea level for pressure, density, and temperature, respectively.

4. Operational Constraints and Boundary Conditions

The studied scenario corresponds to RWY 36L at the Adolfo Suárez Madrid-Barajas airport. The surveillance data has been analyzed in order to identify the operational constraints of the scenario prior to the performance of the simulations. Flows for departures and arrivals have been studied. Moreover, it has also been analyzed the potential interaction of the inbound & outbound flows against the modeled flight segment for SIDs BARDI2T/CCS1T and BARDI2K/CCS1K.

Determining the capacity effects when facilitating CCOs has been applied to the aforesaid SIDs, where the performance of the aircraft plays a significant role. The clearance for flying a CCO technique does not take the aircraft operator away from being compliant with the numerous operational constraints.

The considered flight segments start with a climb on the runway heading directly to DVOR/DME SSY and finish when crossing AVILA waypoint at 12000 ft or above. The operation of these flight segments may be influenced by aircraft performance limitations, which may be translated on negative effects depending on the selected SID. It is worth mentioning that assuming the initial Air Traffic Control (ATC) clearance of maintaining 13000 ft and requesting flight level change en route may not stop a continuous climb operation in the first instance.

The assumed separation for departures is time based. The considered value is 120 seconds between any combinations of aircraft types. Regarding the operational constraints, Table 1 gathers the operational constraints, like Minimum Climb Gradient (MCG) and Knots Indicated Airspeed (KIAS), among others.

The computational cost for finding the solution is significantly higher when the problem is applied to actual scenarios due to the mandatory compliance of actual operational constraints. The initial conditions on the studied procedure are taken at the moment the aircraft lines up for taking off. Table 2 summarizes the main boundary conditions considered when modeling the departures for the considered aircraft types, Airbus 319 (A319) and Airbus 330 (A330). The surveillance data analysis performed through additional hand-tailored MATLAB models enabled the operational assessment of departure and arrival flows as well as the calculation of some relevant parameters indicated within Table 2. The analysis of the surveillance data brings up interesting facts, for example, SID BARDI2T/CCS1T is highly operated by mediums compared to heavies. Considering this, it is not realistic to consider a medium aircraft operating BARDI2K/CCS1K SID.

5. Model

Traditionally, tactical controllers manage the aircraft within their airspace domain and provide clearances to specific altitudes based on the characteristics of the traffic in terms of complexity and airspace layout. A conventional departure trajectory, which has been vertically limited, presents several level-offs before reaching the cruise level. There is a limit to

Table 2: Boundary conditions.

SID	BARDI2T/CCS1T	BARDI2K/CCS1K
RWY (h)	0 ft	
RWY (KIAS)	0 knots	
RWY (Rate of Climb (ROC))	0 ft	
AVILA (h)	16200 ft–26400 ft	
AVILA (KIAS)	392 knots (A319)/389 knots (A330)	401 knots (A330)
AVILA (ROC)	2165 fpm (A319)/1546 fpm(A330)	1467 fpm (A330)
Flight distance	47 NM	56 NM

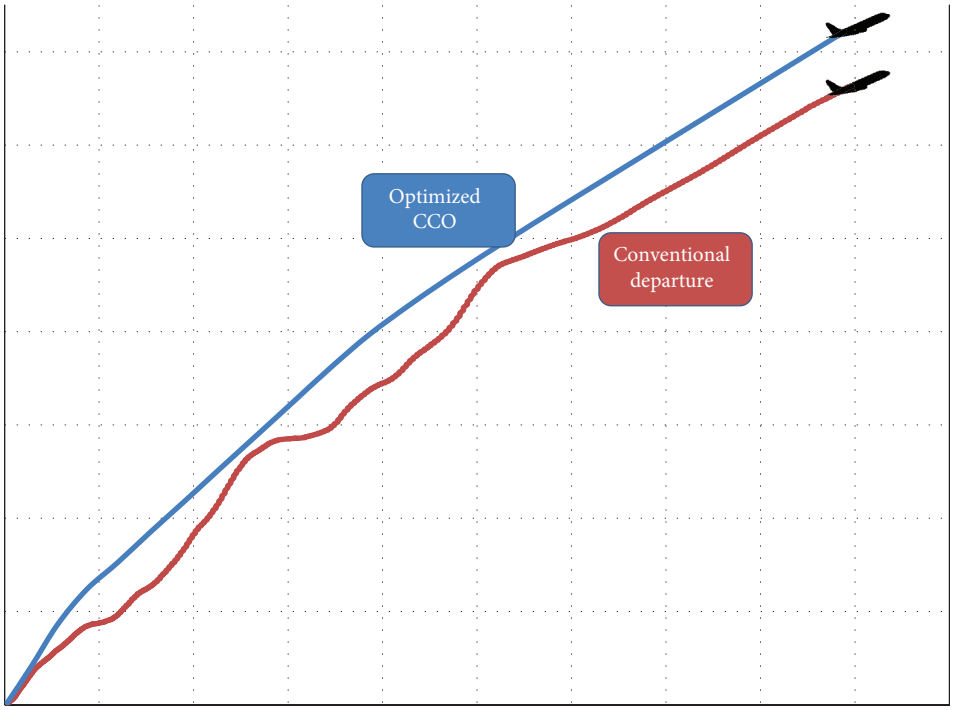

Figure 2: Departure flight paths. Optimized CCO versus standard departure.

the number of aircraft a controller can keep track of at one time, so as airspace has to be subdivided in airspace sectors, the flights require leveled segments. These leveled segments on the vertical profile penalize the aircraft efficiency and prevent the aircraft from flying its ideal trajectory. Conversely, the performance of an optimized CCO that allows the aircraft to attain initial cruise flight level at an optimum air speed with optimal thrust settings brings noteworthy benefits to the flight efficiency. Figure 2 illustrates a standard departure and an optimized CCO where the differences between the departure flight paths can be appreciated.

The mathematical method used for the optimization of the CCO is based on the optimal control theory, which aims at determining the control input that will cause a system to achieve the control objectives, whilst satisfying the constraints and also optimizing some performance criterion. The trajectory optimization problem was solved following an open loop terminal control problem that allows the constraints acting on the dynamical system to be considered in a way that the obtained trajectory will be admissible.

Commercial aircraft trajectory problems have been tackled through open loop optimal control techniques [8–10]. However, optimal control problems are characterized for being highly nonlinear, and thus, it becomes certainly difficult to find analytical solutions. Numerical methods are typically used for this purpose, and direct methods fit the approach for the trajectory optimization problem. A simplistic description of direct methods could be presented as discretizing the optimal control problem at the nodes of discretization, resulting to a NLP ready to be solved.

5.1. Optimal Control Problem. With the aim of facilitating the discussion, consider the following optimal control problem (OCP):

$$\min J(t, x(t), u(t), l) = E\left(t^{\mathrm{F}}, x\left(t^{\mathrm{F}}\right)\right) + \int_{t^{\mathrm{I}}}^{t^{\mathrm{F}}} L(x(t), u(t), l)dt, \tag{2}$$

subject to

$\dot{x}(t) = f(x(t), u(t), l)$, dynamic equations; $0 = g(x(t), u(t), l)$, algebraic equations; $x(t^{\mathrm{I}}) = x^{\mathrm{I}}$, initial boundary conditions; $\psi(x(t^{\mathrm{F}})) = 0$, terminal boundary conditions; and $\phi_l \le \phi[x(t), u(t), p] \le \phi_u$, path constraints.

Variable $t \in [t^{\mathrm{I}}, t^{\mathrm{F}}] \subset \mathbb{R}$ represents time, and $l \in \mathbb{R}^{n_l}$ is a vector of parameters. Notice that the initial time t^{I} is fixed and the final time t^{F} might be fixed or left undetermined. $x(t)$: $[t^{\mathrm{I}}, t^{\mathrm{F}}] \to \mathbb{R}^{n_x}$ represents the state variables. $u(t)$: $[t^{\mathrm{I}}, t^{\mathrm{F}}] \to \mathbb{R}^{n_u}$ represents the control functions, also referred to as control inputs, assumed to be measurable. The objective function $J : [t^{\mathrm{I}}, t^{\mathrm{F}}] \times \mathbb{R}^{n_x} \times \mathbb{R}^{n_u} \times \mathbb{R}^{n_l} \to \mathbb{R}$ is given in the Bolza form. It is expressed as the sum of the Mayer term $E(t^{\mathrm{F}}, x(t^{\mathrm{F}}))$ and the Lagrange term $\int_{t^{\mathrm{I}}}^{t^{\mathrm{F}}} L(x(t), u(t), l)dt$.

Functions $E : [t^{\mathrm{I}}, t^{\mathrm{F}}] \times \mathbb{R}^{n_x} \to \mathbb{R}$ and $L : \mathbb{R}^{n_x} \times \mathbb{R}^{n_u} \times \mathbb{R}^{n_l} \to \mathbb{R}$ are assumed to be twice differentiable. The system is a DAE system in which the right hand side function of the differential equations $f : \mathbb{R}^{n_x} \times \mathbb{R}^{n_u} \times \mathbb{R}^{n_l} \to \mathbb{R}^{n_x}$ is assumed to be piecewise Lipschitz continuous, and the derivative of the algebraic right hand side function $g : \mathbb{R}^{n_x} \times \mathbb{R}^{n_u} \times \mathbb{R}^{n_l} \to \mathbb{R}^{n_z}$ with respect to z is assumed to be regular. $x^{\mathrm{I}} \in \mathbb{R}^{n_x}$ represents the vector of initial conditions given at the initial time t^{I} and the function $\psi : \mathbb{R}^{n_x} \to \mathbb{R}^{n_q}$ provides the terminal conditions at the final time, and it is assumed to be twice differentiable. The system must satisfy algebraic path constraints given by the function $\phi : \mathbb{R}^{n_x} \times \mathbb{R}^{n_u} \times \mathbb{R}^{n_l} \to \mathbb{R}^{n_\phi}$ with lower bound $\phi_l \in \mathbb{R}^{n_\phi}$ and upper bound $\phi_u \in \mathbb{R}^{n_\phi}$. Function ϕ is assumed to be twice differentiable.

The Chebyshev pseudospectral method, which has demonstrated advantages over indirect methods, is widely used in engineering applications, especially on trajectory optimization problems [11]. This spectral method utilizes orthogonal polynomials instead of piecewise continuous polynomials when approximating state and control variables. F. Fahroo and I. M. Ross presented at [12] the demonstration of the fact that Chebyshev-Gauss-Lobatto (CGL) method yields more accurate results than those obtained from the traditional collocation method. Recently, in [13], an intensive analysis on different direct collocation methods to solve a classical problem on ATM was presented. Once again, pseudospectral collocation method has proven better results on accuracy and computational time but uncertainties in vertical trajectories during a climb/descent.

In this investigation, the operational flight paths were obtained through multiobjective optimization process based on CCO principles by a CGL pseudospectral method. The calculations were executed through a hand-tailored software tool implemented on AMPL modeling language [14] for Airbus A319 and A330 aircraft, using IPOPT as the NLP solver. The latest Base of Aircraft Data (BADA 4.1 [15]) supported the AMPL self-implemented optimization model. AMPL is an algebraic modeling system for mathematical programming of large-scale optimization problems. For the sake of clarity, a solver is defined as the number-crunching algorithm that computes optimal solutions. The calculated optimal trajectories were stored in a database for further processing.

5.2. Optimization Criteria. The environmental optimization criterion has been modeled considering two magnitudes: maximum A-weighted sound level ($L_{\max}$) and fuel burn. Aiming at supporting this multiobjective optimization, the weighted combination of the aforementioned factors has been implemented as follows:

$$J = a\,(\text{noise}) + b\,(\text{fuel consumption}), \tag{3}$$

where a and b are adjustable weighting constants. The values of these constants are directly related to the trade-off between noise exposure and fuel consumption/emissions. In this study, both factors have received the same weighting avoiding the prioritization of one of them. It is out of the scope of this study to present the analysis of Pareto for the aforesaid weighting constants. The considered parameter for noise optimization, maximum A-weighted sound level ($L_{\max}$), is based on the methodology employed by the Integrated Noise Model (INM) [16]. The core of this methodology relies on the Noise-Power-Distance (NPD).

5.3. Departure Capacity Model. The following steps were required to establish the appropriate enablers that allow addressing of the main objective of this study, in other words, the means of evaluating the operational implications of integrating optimal CCOs.

The scenario was modeled considering operational and physical constraints. The derivation of the runway utilization rates when performing CCOs required the construction of a departure capacity model. It was flexibly constructed, based on the MATLAB software tool, in a number of stages:

(1) The physical constraints were analyzed for variability across departure routes

(2) The different operational constraints were compared to determine which were the most dominant

(3) Preprocess of surveillance data and FDR data to generate database

(4) Databases (actual data) were processed through an additional MATLAB model to determine arrival and departure traffic flows, as well as aircraft type patterns

(5) In parallel, the optimal CCOs were simulated whilst being complied with the identified constraints

(6) The databases (optimized trajectories) were compiled by using the data obtained from the simulations

(7) The databases were processed by the capacity model with the aim of determining the runway utilization rates

The data regarding the considered aircraft types (A330\A319) was processed by the departure capacity model ensuring no loss of separation. The separation values for this calculation were 1000 ft (vertical) and 3 NM (horizontal) [17]. Table 3 presents the evaluated aircraft types per SID.

Table 3: Aircraft types and their associated mass (M) per SID for optimal CCOs and conventional departures.

SID	BARDI2T/CCS1T	BARDI2K/CCS1K
Aircraft (CCO)	M1/M2/M3 (A319)/M1/M2/M3 (A330)	M1/M2/M3 (A330)
Aircraft (conventional)	M1/M2/M3 (A319)/M1/M2/M3/M4 (A330)	M1/M2 (A330)

As it is possible to appreciate on it, the A319 were not considered for BARDI2K/CCS1K taking into account the findings from the surveillance data analysis. It bears out the fact that mediums operating the long leg when departing west are not usual. Regarding the aircraft mass for CCOs, several highly representative take-off mass values were considered where M1 represents the lightest of the studied actual data sample. The figures are not provided in purpose.

Different path lengths, speeds, altitudes, ATC constraints, performance limitations, and operational-cleared levels are some of the numerous parameters, which were considered. The construction of the model was reviewed and discussed with operational staff ensuring the most realistic scenario. The selected mechanism of evaluating the capacity is based on the Monte Carlo simulations that were hand-tailored through MATLAB.

6. Results

Estimating capacity is a matter of paramount importance to all airport planning and analyzing the capacity effects of this particular operational technique on a certain scenario helped on evaluating its potential applicability. The selected method to evaluate CCOs was to study them against actual conventional departures. From an operational point of view, it has been assumed departure separation is based on time. In this regard, a standard time separation of 120 seconds between consecutive departures has been considered. Unfortunately, the combination of certain conventional departures and optimal CCOs may require longer time spacing while ensuring safety operations between the aircrafts along the SIDs.

Figure 3 gathers the information regarding the effects on time spacing in view of the results obtained, is influenced, by the SID and the combination of leading (each represented line) and trailing aircraft (abscissa axis). The following points address those combinations of departures where longer time spacings, than the standard 120 seconds, are required to ensure no loss of separation.

(1) M1B2KA330 (.-+). Being the leading aircraft, an A330 departing BARDI2K/CCS1K whilst performing a conventional departure, it is necessary for an increase of time spacing between 61 and 65 seconds when the trailing aircraft is A319 and between 28 and 38 seconds for A330 performing conventional departures through BARDI2T/CCS1T

(2) M2B2KA330 (-+). Leading aircraft, an A330 departing BARDI2K/CCS1K whilst performing a conventional departure, it is necessary for an increase of time spacing between 52 and 56 seconds when the trailing aircraft is A319 and between 27 and 36 seconds for A330 performing conventional departures through BARDI2T/CCS1T

(3) M1B2KA330 CCO (.-o). Being the leading aircraft, the lightest A330 (M1) departing BARDI2K/CCS1K whilst performing a CCO, it is necessary for an increase of time spacing between 29 and 35 seconds when the trailing aircraft is A319 performing CCOs through BARDI2T/CCS1T and between 7 and 35 seconds for A330 departing through BARDI2T/CCS1T

(4) M2B2KA330 CCO (-o). Being the leading aircraft, the A330 (M2) departing BARDI2K/CCS1K whilst performing a CCO, it is necessary for an increase of time spacing between 25 and 31 seconds when the trailing aircraft is A319 performing CCOs through BARDI2T/CCS1T and between 4 and 31 seconds for A330 departing through BARDI2T/CCS1T

(5) M3B2KA330 CCO (-o). Being the leading aircraft, the heaviest A330 (M3) departing BARDI2K/CCS1K whilst performing a CCO, it is necessary for an increase of time spacing between 22 and 28 seconds when the trailing aircraft is A319 performing CCOs through BARDI2T/CCS1T and up to 28 seconds for A330 departing through BARDI2T/CCS1T

Considering the above factors it is interesting to highlight two findings: first of all, when the leading aircraft is performing a conventional departure via the long leg of the SIDs (BARDI2K/CCS1K), the standard time spacing requires to be increased. This time spacing is likely to be higher when the trailing aircraft type is lighter than the leading one. Secondly, it is interesting to note the fact that when the leading heavy aircraft is performing a CCO via BARDI2K/CCS1K, it is necessary for more time spacing for the trailing aircraft flying CCOs than conventional departures.

6.1. Runway Capacity Effects Due to CCO Expedition. Finally, the effects on capacity for each combination of leading-trailing aircraft were calculated using Monte Carlo simulations. The Monte Carlo simulations were conducted using a hand-tailored model based on MATLAB software tool. Its main objective was to obtain the capacity values per hour of operation considering the previously calculated time spacing between different combinations of aircraft. The simulations were conducted for 10.000

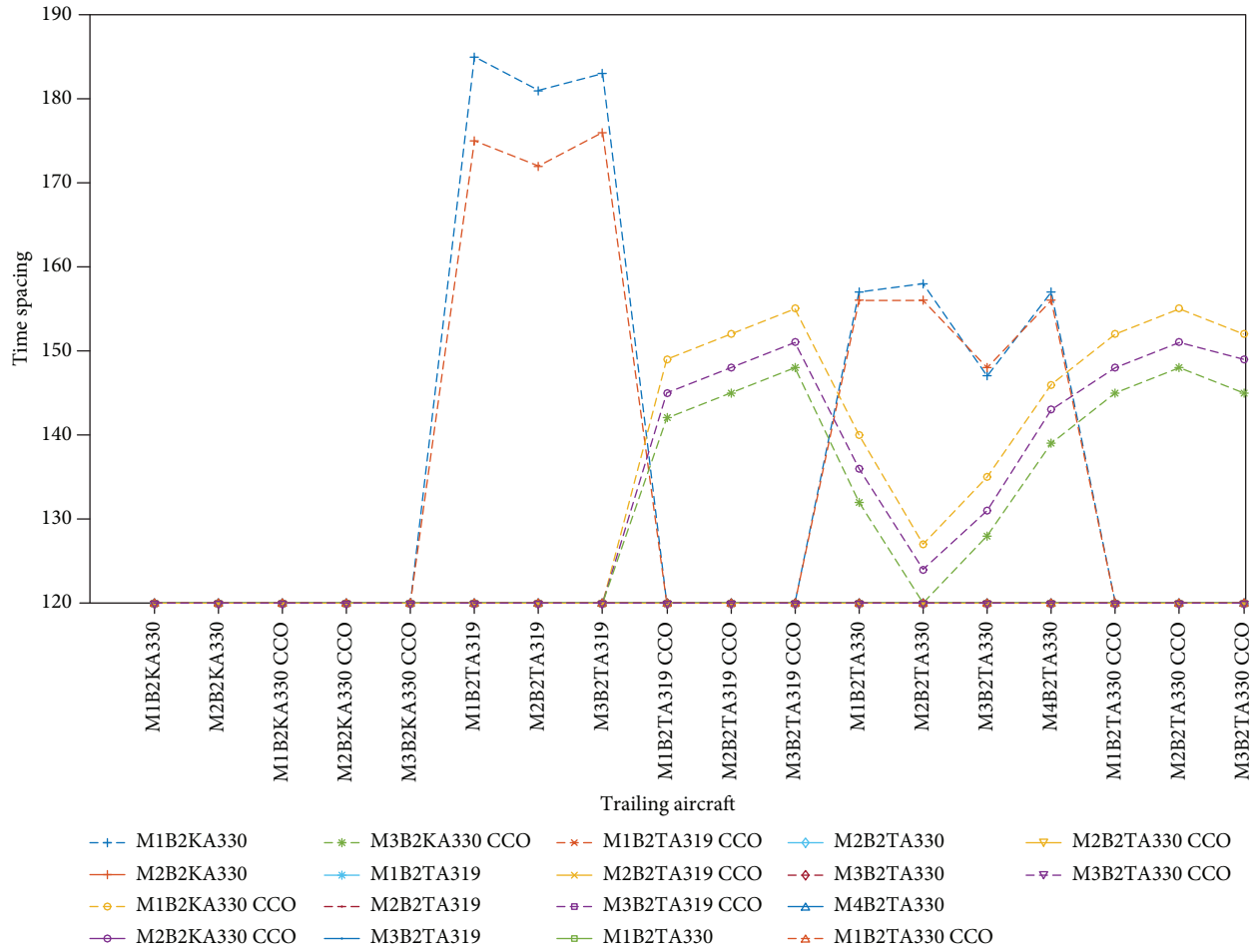

Figure 3: Time separations between aircraft operating BARDI2T/CCS1T and BARDI2K/CCS1K SIDs.

hours per scenario. The model addresses 11 scenarios depending on the percentage of CCOs that covers a total of 110.000 hours analyzed:

(1) *Scenario 1*.100% CCOs

(2) *Scenario 2*. 90% CCOs/10% conventional departures

(3) *Scenario 3*. 80% CCOs/20% conventional departures

(4) *Scenario 4*. 70% CCOs/30% conventional departures

(5) *Scenario 5*. 60% CCOs/40% conventional departures

(6) *Scenario 6*. 50% CCOs/50% conventional departures

(7) *Scenario 7*. 40% CCOs/60% conventional departures

(8) *Scenario 8*. 30% CCOs/70% conventional departures

(9) *Scenario 9*. 20% CCOs/80% conventional departures

(10) *Scenario 10*. 10% CCOs/90% conventional departures

(11) *Scenario 11*. 100% conventional departures

Figure 4 gathers the information regarding the boxplot for each scenario. It allows the reader to appreciate the key results and to identify the key characteristics. The median, which is represented by the line in the box, represents a measure of the center of the data, and the interquartile range box (the green and the red box) brings the distance between the first and the third quartile. Besides, the interquartile range box brings the distance between the first and the third quartile. Last but not the least, the whiskers show the ranges for the bottom 25% and the top 25% of the data values.

(1) *Scenario 1*. The median capacity is 28 movements per hour, and the capacity is as low as 26 and as high as 29. The capacity values are less variable than other scenarios

(2) *Scenario 2*. The median capacity is 28.2 movements. Most of the capacity values are between 28 and 29, and the boxplot manifests top-skewed data, which means that most of the capacity values are lower. The capacity values are as low as 26 and as high as 29

(3) *Scenario 3*. Median capacity value is 28.4, and the interquartile range box is the same as the previous scenario. The boxplot represents top-skewed data. The whisker values are as low as 26 and as high as 29

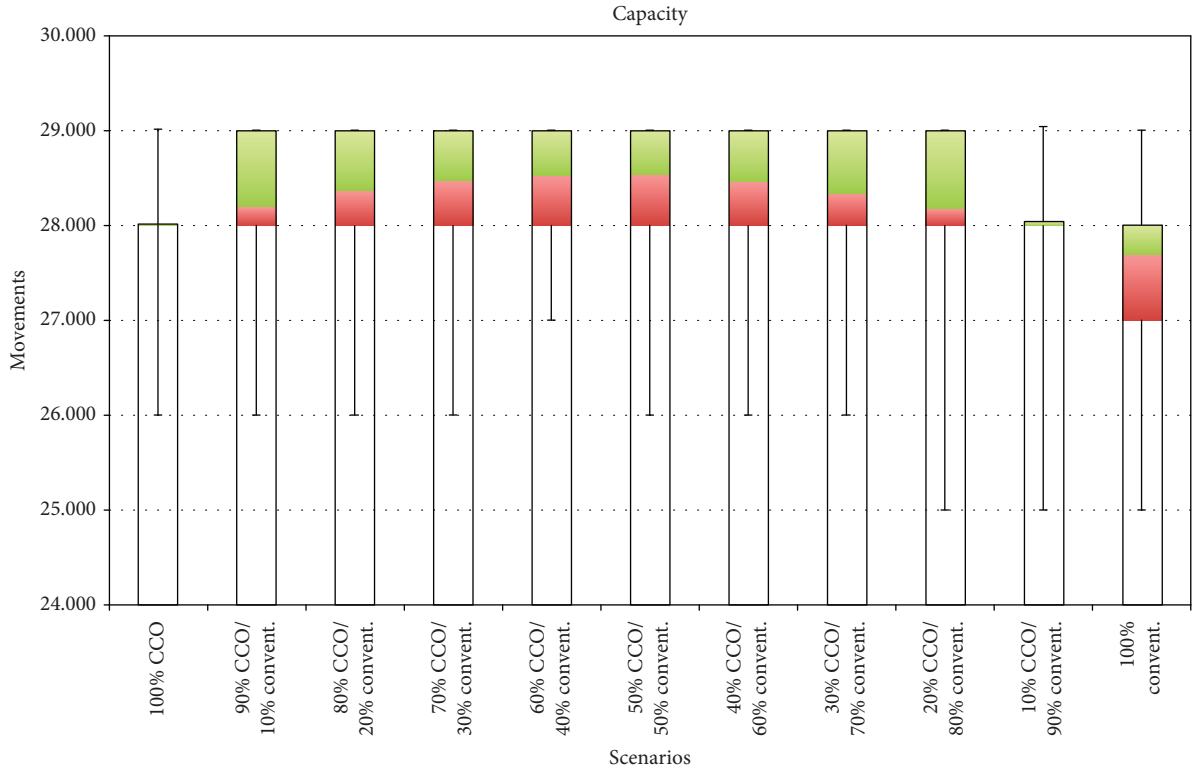

Figure 4: Capacity. Maximum number of aircraft that can be accommodated per hour according to aforementioned scenarios.

(4) *Scenario 4*. The median capacity value is 28.5, and the interquartile range box and the whiskers have the same values on the previous scenario. In this case the main difference is regarding the skewed data, which seems to be slightly top-skewed

(5) *Scenario 5*. The median capacity is 28.5, the interquartile range box remains as before but the bottom whisker increases up to 27. In this case, the data is not skewed

(6) *Scenario 6*. The median capacity is 28.5. The interquartile range box is the same as before, but in this case, the lower whisker goes back to 26. The data distribution is symmetric

(7) *Scenario 7*. Median value is 28.5. Similar to scenario 6 where it is possible to appreciate a change of trend regarding the data which is slightly top-skewed

(8) *Scenario 8*. Median value is 28.3. The main difference compared to scenario 6 is that in this case, it is clearly top-skewed data

(9) *Scenario 9*. Median value is 28.2. In this case, the lower whisker decreases down to 25, and the scenario is clearly top-skewed data

(10) *Scenario 10*. Median capacity value is 28 movements per hour, and the capacity is as low as 25 and as high as 29. The capacity values are less variable than other scenarios

(11) *Scenario 11*. Median capacity value is the lowest, 27.7. The capacity is as low as 25 and as high as 29. Most of the capacity values are between 27 and 28, and the boxplot manifests bottom-skewed data, which means that most of capacity values are higher

Figure 5 reveals that the median values for the studied scenarios vary between 27.7 and 28.5. It is interesting to note the fact that those scenarios where the percentages of each type of traffic are similar, the median presents its highest values. The standard deviation appreciated for the scenarios with lower percentage of CCOs are higher. This indicates that the values are more dispersed.

7. Conclusions

In view of the obtained results, the integration of traffic performing CCOs on departures does not affect negatively in terms of runway capacity. Therefore, it may be argued that whilst the combination between leading-trailing aircraft on mixed departures may affect the capacity, the effect is within an acceptable limit.

The integration of CCO does not necessarily require a specific ATM tool at the controller's working position but the procedures should support them. Nevertheless, the results suggest that integrating CCOs along with a combination of a departure sequence tool tend to mitigate the characteristics of these operating techniques.

Unlike standard arrival routes where aircrafts are tactically guided by air traffic controllers, SID routes tend to follow fixed flight paths. Thus, the optimization of the

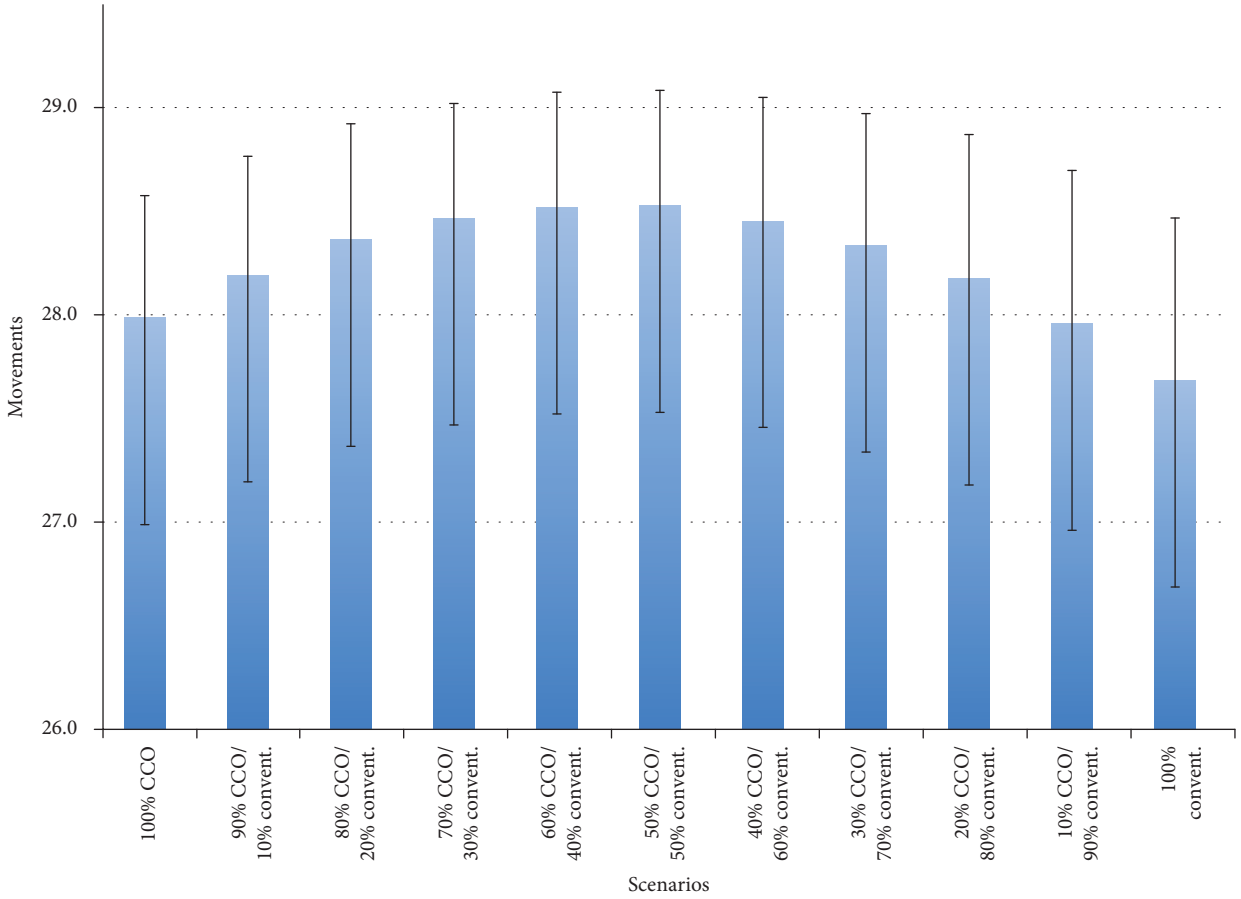

Figure 5: Capacity. Mean capacity values are represented by the bar plot and the associated standard deviations of the sample are illustrated by the whiskers.

vertical profile may be considered an appropriate initiative for departure efficiency.

Allowing the airspace user to fly optimized continuous climb operations will bring significant benefits in greenhouse gas and noise emissions in the vicinity of airports. From the operational point of view, it will lead to more consistent flight paths whilst reducing the number of required radio transmissions. As a consequence, this may be traduced on lower pilot and air traffic controller workload.

This study reinforces the idea of transmitting the importance of CCOs and, furthermore, promotes the usage of this operating technique in TMAs.

Nomenclature

C_d: Coefficient of drag
C_l: Coefficient of lift
D: Drag force
g: Gravity acceleration
h: Altitude
L: Lift force
m: Mass
p: Atmospheric pressure
p_0: Standard value at sea level for atmospheric pressure
t: Time
T: Thrust
V: True airspeed
x: Longitudinal position
η: Thrust-specific fuel flow
γ: Flight path angle
ρ: Atmospheric density
ρ_0: Standard value at sea level for atmospheric density
τ: Temperature
τ_0: Standard value at sea level for temperature.

Data Availability

The data used to support the findings of this study are available from the corresponding author upon request.

Conflicts of Interest

The authors declare that there is no conflict of interest regarding the publication of this paper.

References

[1] ICAO, *Continuous climb operations (CCO) manual*, International Civil Aviation Organization, 1st edition, 2013.

[2] SESAR, "Single sky atm research (2016)," September 2016, http://www.sesarju.eu.

[3] ICAO, *Global air navigation plan 2016-2030*, International Civil Aviation Organization, 2013.

[4] NextGen, "The next generation air transportation system (2016)," https://www.faa.gov/nextgen/.

[5] D. McConnachie, P. Bonnefoy, and A. Belle, "Investigating benefits from continuous climb operating concepts in the national airspace system," in *11th USA Europe Air Traffic Management Research and Development Seminar*, pp. 1–11, Lisbon, Portugal, 2015.

[6] M. Z. Li and M. S. Ryerson, "A data-driven approach to modeling high-density terminal areas: a scenario analysis of the new Beijing, China airspace," *Chinese Journal of Aeronautics*, vol. 30, no. 2, pp. 538–553, 2017.

[7] ICAO, *Manual of the ICAO standard atmosphere*, International Civil Aviation Organization, 3rd edition, 1993.

[8] P. Bonami, A. Olivares, M. Soler, and E. Staffetti, "Multiphase mixed-integer optimal control approach to aircraft trajectory optimization," *Journal of Guidance, Control, and Dynamics*, vol. 36, no. 5, pp. 1267–1277, 2013.

[9] A. Franco and D. Rivas, "Optimization of multiphase aircraft trajectories using hybrid optimal control," *Journal of Guidance, Control, and Dynamics*, vol. 38, no. 3, pp. 452–467, 2015.

[10] D. González-Arribas, M. Soler, and M. Sanjurjo-Rivo, "Robust aircraft trajectory planning under wind uncertainty using optimal control," *Journal of Guidance, Control, and Dynamics*, vol. 41, no. 3, pp. 673–688, 2018.

[11] J. Zhao, R. Zhou, and X. Jin, "Reentry trajectory optimization based on a multistage pseudospectral method," *The Scientific World Journal*, vol. 2014, Article ID 878193, 13 pages, 2014.

[12] F. Fahroo and I. M. Ross, "Direct trajectory optimization by a chebyshev pseudospectral method," *Journal of Guidance, Control, and Dynamics*, vol. 25, no. 1, pp. 160–166, 2002.

[13] J. García-Heras, M. Soler, and F. J. Sáez, "A comparison of optimal control methods for minimum fuel cruise at constant altitude and course with fixed arrival time," *Procedia Engineering*, vol. 80, pp. 231–244, 2014.

[14] AMPL, "AMPL modeling language (2013)," September 2016, http://ampl.com.

[15] Eurocontrol, "User manual for the base of aircraft data (BADA) family 4," in *European organisation for the safety of air navigation*, EUROCONTROL Agency Rue de la Fusee, 2014.

[16] E. R. Boeker, E. Dinges, B. He et al., *Integrated noise model (inm) version 7.0 technical manual, FAA-AEE-08-01 NSN 7540-01-280-550*, U.S. Department of Transportation, Federal Aviation Administration, Office of Environment and Energy, 2008.

[17] ICAO, *PANS-ATM, or procedures for navigation services–air traffic management*, International Civil Aviation Organization, 16th edition, 2016.